QUANTUM MONTE CARLO STUDY OF BOSONIC SOLIDS AT ZERO TEMPERATURE

by

CLAUDIO CAZORLA SILVA

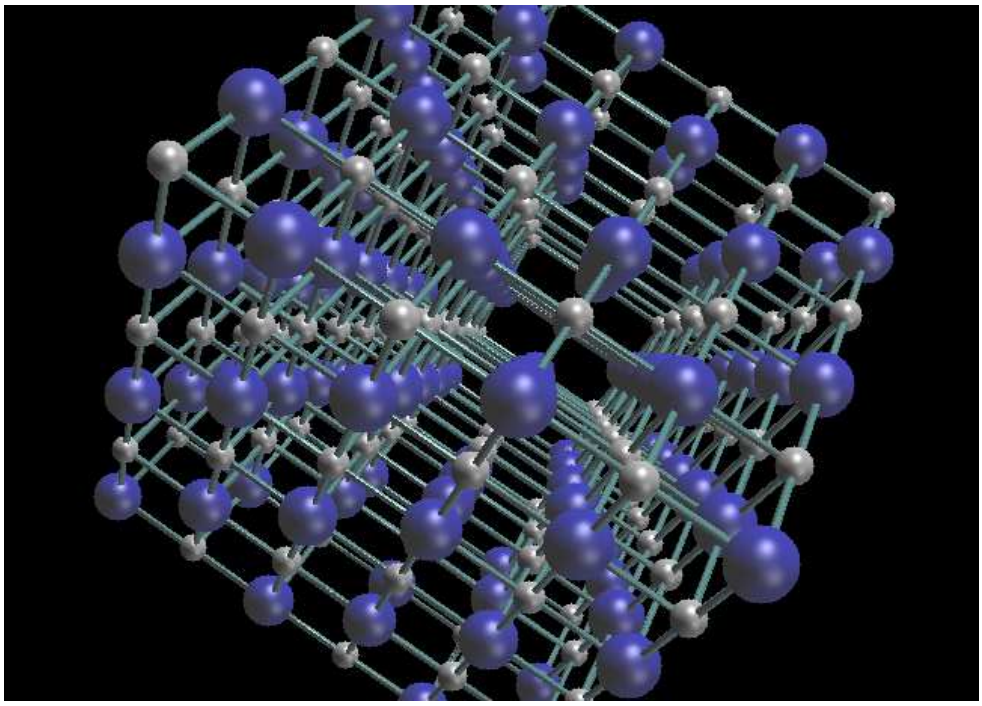

Universitat Politècnica de Catalunya

Dept. de Física i Enginyeria Nuclear

Barcelona, October 2005

Dissertation of the Doctoral Thesis supervised by Dr. Jordi Boronat

Abstract

Quantum solids conform an intriguing class of crystals where quantum effects have a leading relevance. Contrarily to their classical counterparts, quantum solids present both unusually *large* kinetic energy and mean displacement of the particles around the equilibrium positions of the crystalline lattice. By *large* it is understood a kinetic energy similar in magnitude to short–range interactions, and mean displacement comparable to the distance between nearest positions in the perfect lattice (large Lindemann's ratio). In fact, the constituents of these solids are characterized by small atomic masses and weakly attractive interactions acting among them. From a thermodynamic point of view, quantum solids are described by large compressibilities, low Debye temperatures and speeds of sound, non–ordinary melting properties, anharmonicity, etc. Point and line defects (vacancies, dislocations, etc.) are easily formed on their interior due to the wide excursions of the atoms around the lattice sites. These structural defects are expected to exist in quantum solids even at absolute zero temperature. Some illustrative examples of quantum solids are $^4\mathbf{He}$, $^3\mathbf{He}$, $\mathbf{H_2}$, $\mathbf{D_2}$, $\mathbf{LiH}$ and $\mathbf{LiD}$. In the outstanding case of solid helium, the possibility of superfluid-like behaviour has resulted in a long-standing topic of intense speculation. Recent experiments carried out by E. Kim and M. H. Chan in solid $^4\mathbf{He}$, seem to allow the existence of a practically suppressed superfluid fraction below 0.2K ($\sim$1-2%).

Early in the 60's, Quantum Monte Carlo (QMC) methods emerged in close relation to quantum many–body problems posed in the field of condensed matter. The QMC approach is a fully quantum one (it does not rely on any basic assumption or approximation), which it is best suited to deal with systems where quantum effects are dominant. The basic strategy underlying QMC methods is stochastic, that is, random number generation and probability theory are inherent to all of them. In this thesis, two different QMC techniques have been used to investigate the ground–state properties of quantum solids, namely, variational Monte Carlo (VMC) and diffusion Monte Carlo (DMC). The VMC approach relies on the variational principle and it provides accurate estimations of the total energy based on reliable models for the ground–state wave function. On the other hand, the DMC method allows us to solve

exactly the imaginary time-dependent Schrödinger equation of interest, providing asymptotically its ground–state solution. Accurate estimations of the total energy and expected values of operators which commute with the Hamiltonian are yielded in this scenario with affordable computational effort.

Comprehensive studies of the energy and structural properties of the solids cited above (made the exception of ^{3}**He**) and **Ne**, which is a crystal in the middle–way between quantum and classical behaviour, have been carried out with the two mentioned QMC approaches. In the case of solid ^{4}**He**, we have also tried to shed more light on the issue of superfluidity. Actually, the species investigated in the present work turn out to be representative elements of the quantum solid class; the importance of quantum effects as well as the dimensionality chosen for their study are assorted.

Table of Contents

To my Parents, Brother and Sister

Acknowledgements

De forma muy especial y sincera, quiero agradecer a Jordi Boronat la ayuda que a distintos niveles y tan generosamente me ha brindado a lo largo de estos años (Boro, moltes gràcies per la teva sensibilitat i dedicació).

De igual manera agradezco a mis padres el incondicional apoyo que ya de bien pequeño he recibido siempre de ellos (gracias por motivarme en tantos aspectos y tan ricamente, aunque entendáis poco o nada de lo aquí se dice os dedico por completo este manuscrito). Juan y Laura, *idem* para vosotros.

A Marta le doy un fuerte abrazo por animarme a participar en esta carrera. Júlia, un beso muy especial, gracias por toda tu motivación y apoyo en mi investigación científica y personal, especialmente durante este *sprint* final y cuesta arriba.

Marco (o también agua, solucionador de problemas, hermano de chistorra, tio cojonudo,...), Ester (o també aire, d'Igualada, aigua de Ribes, poma, la meva amiga especial,...) i Kostas (o también fuego, planificador, limón, griego tenaz,...) aunque nos hayamos visto los caretos tantos días (y también noches) os echaré de menos, ¿con quién podré discutir tanto y sobre temas tan variados?.

Un abrazo a mis dicharacheros vecinos de despacho, siempre tan alegres y bien dispuestos (Rubén, figura, cuida de nuestras alumnas más sobresalientes; Nuri, cuando peles una naranja acuérdate de mi; Oscar, mándame mensajes siempre que quieras; Toni, ánimo con los chavales). Michele, Vicente, Agustí y Ramón, por estar en el otro pasillo no os vais a librar, ¡marchando más abrazos!.

Un saludo a los "cuñaos" de Sant Adrià, en especial a Dani con quien comparto muchas ilusiones; después de tantas maratones de fiesta juntos, quedarán en pié solo las neuronas más capaces (¡a reventar el medallero!).

En general, agradezco a cada miembro de la sección (Dept. Física i Enginyeria Nuclear de la Facultad de Informática de Barcelona) la cordialidad y animosidad con la que me habéis tratado desde el primer día en que pisé el departamento, muchas gracias a todos.

General Introduction

Monte Carlo (MC) methods have been vastly used for solving a great variety of mathematical problems for the last decades. From complex systems to nuclear physics they have provided fruitful results and interesting new approaches, due to their natural ability in dealing with huge numbers of variables and easy implementation on computers. Stochasticity, which in essence includes probability theory and random number generation, is inherent to all these techniques.

The name "Monte Carlo" was first applied by the scientists working on the atomic bomb in Los Alamos (1940's) to a certain class of mathematical methods based on chance-game outcoming. They inspired in the famous city of Monaco where is actually common to try one's luck in drawing the dices and roulettes. These stochastic techniques, which at the beginning were just didactic examples and/or pure mathematical entertainment, have become powerful tools in simulating real systems.

The first quantitative MC result dates from the early 1950's, when Metropolis *et al.* developed a probability based method to study the classical gas. In this pioneering work [1], Metropolis *et al.* introduced a general method for making feasible the generation of stochastic variables from non–trivial probability distribution functions. This method, known in short as Metropolis sampling, has been applied for solving a great deal of problems in material science, nuclear physics, condensed matter, etc.

Quantum Monte Carlo (QMC) groups the techniques which aim to study atoms, molecules and electronic configuration at the regime of low temperature, where quantum effects have a fundamental role [2, 3, 4]. With these methods it is possible to perform a fully quantum–mechanics approach at the microscopic level and remove the constraints of variational theory or truncation series schemes [5] (Correlated Basis Functions -CBF- and HyperNetted Chain -HNC-, Coupled–Cluster Theory -CC-, etc.). On the contrary, the convergence to the solution in the QMC scenario, which is equivalent to CPU time on practice, will depend on the complexity of the interactions and size of the system.

The central issue on this thesis is the theoretical study of bosonic quantum solids at zero temperature through the quantum Monte Carlo approach. Quantum crystals, in contrast with their classical counterparts, exhibit both large kinetic energies and mean squared displacements of the particles around the equilibrium positions; these differences come from the light mass of their constituents and weak interactions acting among them. Early in the development of quantum mechanics, the importance of quantum effects in the thermodynamics of these solids (^{4}**He**, ^{3}**He**, $\mathbf{H_2}$, etc.) was recognized. The first theoretical models devised to deal with them assumed spherical particles interacting through harmonic forces. Later on, most of the related works were devoted to include the noticeable contributions of nonharmonic interactions into this too simplified quantum description.

In fact, QMC methods is one of the best suited fully quantum approaches for treating quantum solids. As it is shown in the following chapters, theoretical calculations carried out on them are obtained with high accuracy and affordable computational effort.

Thesis' Outline

The contents of this thesis are grouped in three different parts (Introduction, Development and Conclusions).

The first one includes Chapters 1 and 2 and aims to give a general overview of Quantum Solid Physics as well as the computational methods we have used to dive into it. This part does not fit to an exhaustive description of such topics, but instead, to an exposition of the main concepts and the strategies employed in the second part of this work.

The second part embraces from Chapter 3 to 6, and is devoted to the exposition of the results we have achieved in the last years within the field of Quantum Solid Simulation. In Chapter 3, we present an exhaustive study of two–dimensional $\mathbf{H_2}$ and $\mathbf{D_2}$ at zero temperature; also therein the superfluid–like behaviour of a $\mathbf{H_2}$ film on different alkali substrates is investigated. Chapter 4 contains a variational study of the ionic species **LiH** and **LiD**; the theoretical results concerning them are contrasted with some recent neutron scattering experiments. In Chapter 5, we report results for the ground–state energy and structural properties of solid **Ne**; one of the purposes of this study is

to shed some more light on the connections between scattering experiments and quantum calculations of quantum solids. The last chapter of this part is devoted to an accurate study of the energy, structural and superfluid–like properties of solid ^{4}**He**, the quantum crystal for excellence.

The last part corresponds to Chapter 7 (*General Conclusions*); therein, the main results and conclusions reported in the second part of this work are reviewed and presented together in order to provide a general view of them.

Chapter 1
Quantum Solids and variational approach

1.1 Introduction

1.1.1 When a system is a quantum system?

If we were able to observe the atoms of a solid or a liquid while cooling them down to a temperature of few kelvins, we would realize from a certain moment on that Newtonian Mechanics would not be correct. We would have reached then the quantum regime of the system. The degree of quantumness of a system may be drawn from the thermal $De\ Broglie$ wavelength [6], λ^*, associated to a particle of mass m,

$$\lambda^* = \frac{h}{\sqrt{2mk_BT}} \tag{1.1}$$

where h is the Planck's constant, k_B the Boltzmann's constant and T the temperature.

When the typical length of the system we are studying (interparticle distance a, for example) is comparable in magnitude to λ^*, Quantum Mechanics is required. This can be understood by the overlap between wave functions associated to different particles that appears when $\lambda^* \approx a$ and that gives rise to quantum interference patterns. Hence, it can be deduced from relation (1.1) that systems composed by light mass elements and at very low temperature are clear candidates to present quantum behaviour.

Just as an example, if we think in a pub crowded of people where the typical distance is of order 10^{-1}m, we would refer to it as a $classical$ system because the De Broglie wavelength associated to a person of 60 Kg weight

at a temperature of 300 K is around 10^{-24} m. In contrast, the corresponding wavelength for an atom with few protons on its nuclei and at 1 K of temperature, would be of order 10^{-10} m, a common scale in microscopic systems. In this case, a full quantum approach would be required to get the relevant properties of the atom. This means, to tackle the Schrödinger equation,

$$i\hbar\frac{\partial\Psi\left(\mathbf{r},t\right)}{\partial t}=-\frac{\hbar^{2}}{2m}\nabla^{2}\Psi\left(\mathbf{r},t\right)+V\left(\mathbf{r}\right)\Psi\left(\mathbf{r},t\right) \tag{1.2}$$

where $V(\mathbf{r})$ is the interatomic potential. Once the wave function $\Psi\left(\mathbf{r},t\right)$ associated to any particle or set of particles is known explicitly, the maximum amount of information concerning it turns out to be accessible.

1.1.2 The QMC scenario

The study of strongly correlated quantum many-body systems has been for several decades one of the most active areas in the field of condensed matter. By strongly correlated system we mean a system where the interactions and typical lengths are so, that particles can not be treated independently. This fact implies that the whole wave function of such a system can not be described exactly by a product of monoparticular states, but instead, by some interparticle correlation functions.

Bearing in mind the arduous subject of quantum correlations, it should be realized that solving the Schrödinger equation corresponding to a many–body interacting system could result in an extremely complicate, and in most cases impossible, task. Quantum Monte Carlo (QMC) methods emerged in close relation with problems of this type; originally they were applied successfully to the study of helium, the paradigmatic quantum fluid, and soon became settled between the best well suited tools devised to deal with these problems.

The QMC method is a microscopic approach (the only input is the interaction between particles) which allows us to solve stochastically the imaginary time–dependent Schrödinger equation of the system. Many different techniques have been developed on this and related frameworks along the last decades (Green Function Monte Carlo -GFMC- [7], [8], Diffusion Monte Carlo -DMC- [9], Path Integral Monte Carlo -PIMC- [10], etc), and they have provided very accurate results, in excellent agreement with experiments, and

deep physical insight. Moreover, when tackling specific condensed matter topics with few or inexistent experimental evidence (helium and hydrogen clusters [11, 12], low dimensional systems at ultralow temperature, etc...) QMC predictions are usually taken as benchmark results which can motivate experimental challenges.

Although these numerical methods are highly suitable to use in problems where Quantum Mechanics is crudely demanding (quantum dots, neutron matter and light nuclei, molecular systems, etc), their effectiveness decreases when the number of particles or degrees of freedom , N, is increased (typically $N \sim 10^{2-3}$), since the growth of computational effort raises according to N^{2-3}. The rapid development of computing machinery together with the design of new and more efficient algorithms can alleviate to some extent this requirement. In fact, few problems (quantum dynamics in general, electronic structure in real materials, biophysics problems,...) still have not been tackled satisfactorily using this approach because either it is not possible in practice or the proper methods are still under development. Nevertheless, this is not the case of the topics exposed in the present thesis.

Next, we present a general microscopic and thermodynamic description of quantum solids, often comparing them with their classical counterparts. Further on, we make a brief review of the variational approaches to get a deeper insight on present Solid State subjects and also an understandable description of the models used in the simulations. To this end, we also bring up some notes about related aspects in liquids, which historically were first devised and actually represent the starting stage of the simulation of solids.

1.2 Quantum solids

1.2.1 General properties

Solid phase is characterized by the periodic distribution of particles according to a precise Bravais lattice defined by a set of primitive vectors [13, 14]. Within a classical framework and in the low temperature regime, these particles rest practically frozen and centered on their lattice positions (defined by linear combinations of the primitive vectors) since the atomic motion is only motivated by thermal excitations, and the crystalline order corresponds to the

configuration of minimum free energy. This fact is reflected on the Classical Equipartition Principle [15], which states that the kinetic energy per particle of a N-body system is proportional to the temperature.

$$\frac{1}{N}\left\langle E_k^{class}\right\rangle = \frac{1}{N}\left\langle \frac{1}{2m}\mathbf{P^2}\right\rangle = \frac{3}{2}k_BT \tag{1.3}$$

As a consequence of the well–defined periodicity in classical solids, structural functions like the pair–radial distribution function and static–structure factor present sharp peaked shapes (see Figure 1.1). Indeed, these structural characteristics together with the whole thermodynamic properties, are deduced from the Maxwell–Boltzmann statistics which assumes that particles are distinguishable.

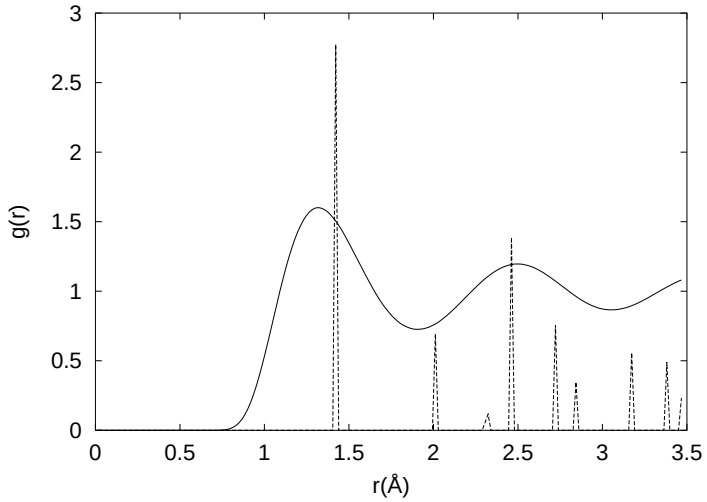

Figure 1.1: Pair–radial distribution functions corresponding to a quantum solid (solid line) and a classical solid (dashed line) at the same density and hcp symmetry. The peaks in the classical case are divided by a factor 20 in order to provide a more easy comparison.

However, the description made above is not valid for quantum solids. Although the periodic order is maintained, particles in quantum solids move noticeably around their lattice sites, not only due to thermal excitations but to their inherent quantumness (see Figure 1.2).

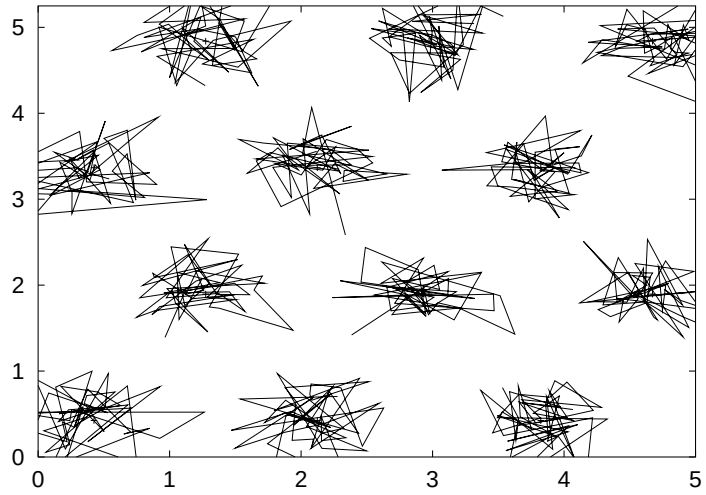

Figure 1.2: The excursions described by particles around the lattice points in a quantum solid are comparable to the lattice parameter. In the figure, the successive positions of some $\mathbf{H_2}$ molecules in a VMC simulation are connected with a solid line.

Behind this statement there is the Uncertainty Principle of Heisenberg,

$$(\Delta x)^2 (\Delta p_x)^2 \geq \frac{\hbar^2}{4} \tag{1.4}$$

where $\Delta x = \sqrt{\langle x^2 \rangle - \langle x \rangle^2}$ and $\Delta p_x = \sqrt{\langle p_x^2 \rangle - \langle p_x \rangle^2}$ are respectively the uncertainties of coordinate x and momentum p_x [16]. In virtue of (1.4), the absolute location of any particle, namely $\Delta x = 0$, is no more possible because otherwise it would imply an inconsistent infinite uncertainty on its momentum, $\Delta p_x \to \infty$. Therefore, quantum particles are in motion, even at zero temperature.

From relation (1.4) it can be derived an equivalent one which is more appropriate for solids

$$\langle E_k \rangle = \frac{\mathbf{p^2}}{2m} \qquad \left\langle \mathbf{u^2} \right\rangle = (\Delta x)^2 + (\Delta y)^2 + (\Delta z)^2$$

$$\left\langle \mathbf{u^2} \right\rangle \langle E_k \rangle \geq \frac{9\hbar^2}{8m} \tag{1.5}$$

that is, expressed in terms of the mean squared displacement $\langle \mathbf{u^2} \rangle$ and monoparticular kinetic energy $\langle E_k \rangle$.

Quantum solids are properly characterized by *large* kinetic energies per particle and *large* mean squared displacements around the equilibrium positions. By *large* it is meant a kinetic energy similar in magnitude to the short–range interactions ($\gg k_B T$), and a mean squared displacement comparable to the distance between two neighbouring positions in the crystalline lattice. In accordance with the previous definition and relation (1.5), quantum solids must be composed of light particles. However, this condition is not sufficient for considering a solid as a quantum solid since it is also necessary to take into account the strength of the interparticle interactions. Thinking about energy minimization, one realizes that particles interacting via strongly attractive potentials would tend to remain close to the equilibrium positions because the increase in the kinetic energy due to the effect of location (see equation 1.5) is lower than the gain in cohesion. As a consequence of this, representative quantum solids must be composed of particles of light mass interacting via weakly attractive potentials in order to fulfill the conditions of large kinetic energy and mean squared displacement.

The relevance of quantum effects on a certain atomic species, can be deduced *a priori* through the de Boer parameter [17]

$$\Lambda^* = \frac{h}{\sqrt{m\epsilon\sigma^2}} \quad , \tag{1.6}$$

where m is the atomic mass, ϵ the well depth of the interparticle pair–potential and σ is the core of the atom (defined as $V(\sigma) = 0$).

This indicator is proportional to the quotient between the de Broglie wavelength (1.1), substituting $k_B T$ by ϵ, and the length scale σ. The greater this parameter is the more relevant quantum effects are in the description of the solid. The Λ^* parameter decreases rapidly when increasing the mass of the atoms and the strength of the attractive potential, that is, moving towards the classical regime (some illustrative values are shown in Table 1.1).

$Crystal$	$\epsilon(K)$	σ (Å)	Λ^*
^{3}**He**	10.22	2.556	2.89
^{4}**He**	10.22	2.556	2.50
Ne	49.05	3.054	0.54
Ar	153.52	3.741	0.17
Kr	210.45	3.999	0.10
Xe	296.27	4.355	0.06

Table 1.1: Quantum de Boer parameters corresponding to rare gases crystals (found in Refs.[30, 32]).

Quantum statistics and particle exchanges

According to Quantum Mechanics, identical particles grouped within the same system are indistinguishable. The general wave function describing them can only be symmetric or antisymmetric under particle exchange. If we think on a set of N particles of the same species, each one labeled with index 1,2,...,N and all governed by the wave function $\Psi(\mathbf{r_1}, \mathbf{r_2}, ..., \mathbf{r_N})$, the previous sentence states that

$$\begin{aligned} \Psi(\mathbf{r_1}, \mathbf{r_2}, ..., \mathbf{r_N}) &= \Psi(\mathbf{r_2}, \mathbf{r_1}, ..., \mathbf{r_N}) \qquad \text{if symmetric} \\ \Psi(\mathbf{r_1}, \mathbf{r_2}, ..., \mathbf{r_N}) &= -\Psi(\mathbf{r_2}, \mathbf{r_1}, ..., \mathbf{r_N}) \quad \text{if antisymmetric} , \end{aligned}$$

where subindexes 1 and 2 are exchanged arbitrarily.

At the same time, particles are classified into two different categories depending on their spin number: boson (integer spin number) or fermion (half-integer spin number). As a consequence of the spin–statistics theorem enunciated by Pauli in 1940 [18], any system composed of identical bosons must be described by a symmetric wave function, and complementarily, any system composed of identical fermions must be described by an antisymmetric wave function. This general classification of quantum systems into bosonic or fermionic, implies two different statistics [15], namely the Bose and Fermi statistics. Certainly, these two statistics lay on the explanation of any many–body quantum phenomenon occurring in the low temperature regime (Bose–Einstein condensation, superfluidity, etc.), and they consistently

tend towards the Maxwell–Boltzmann one (1.7) as the classical regime is approached (T$\gg$0K).

As it has been exposed above, particles composing the same quantum system are indistinguishable and therefore can not be *labeled* in order to be identified. In solids, however, the interactions of a particle with the rest of the system force it to remain near certain equilibrium position; in fact, the diffusion of the particles within crystals is drastically reduced in comparison with the liquid or gas phases. In these conditions, particles turn out to be rather localized and quantum exchange processes just would involve atoms in neighbouring positions. Presumably, the exchange rate in such processes depend on the temperature, strength of the interactions, atomic mass and density (in analogy with the tunnel effect).

For instance, quantum exchanges in crystal $^{\mathbf{3}}\mathbf{He}$ are crucial to understand its magnetic nature [19, 20]. Spin atomic exchanges in this fermionic solid may involve permutations of pairs, triplets and more particles (multiple–exchange model), and occur roughly every 10^5 atomic vibrations. Concerning solid $^{\mathbf{4}}\mathbf{He}$, recent experiments at very low temperature (few tenths of K) seem to allow the possibility of a supersolid phase (a long–standing speculation), based on the observation of a non–classical inertial response (NCIR) to rotation [21, 22]. The NCIR phenomenon could be explained in terms of atomic diffusion within the solid, which indeed requires from active particle exchanges (probably vacancies and/or some other types of crystalline defects might play an important role on this issue). Nevertheless, it is worth noticing that atomic exchanges in quantum solids have a negligible effect on the total energy and related thermodynamic properties (as it will be shown later), since the energy scale involving them is around the mK.

Momentum distribution and anharmonicity

The momentum distribution of a system, $n(\mathbf{k})$, yields the probability for any arbitrary particle of having momentum $\mathbf{p} = \hbar\mathbf{k}$. In a classical framework, the momentum distribution of isotropic solids, liquids and gases are described by the Maxwell–Boltzmann (MB) distribution [23, 24]

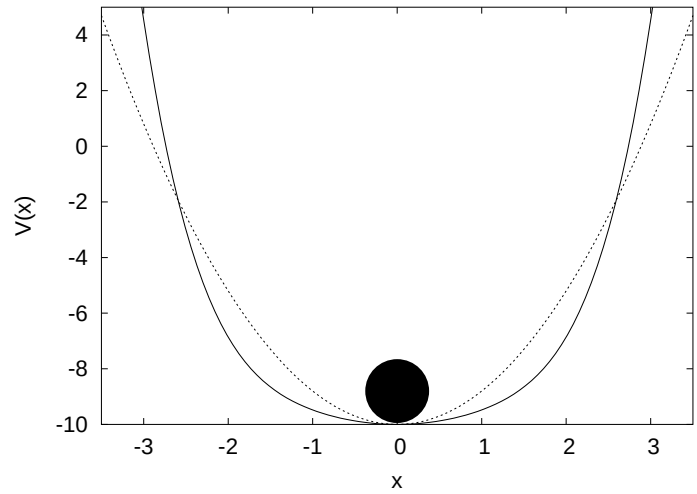

Figure 1.3: The mean potential (arbitrary units) felt by one particle (huge point) around its equilibrium position in a certain quantum solid as a result of the interaction with the rest of the system (solid line). The dashed line corresponds to a general harmonic potential.

$$n(\mathbf{k})^{MB} = \left(\frac{1}{2\pi\alpha}\right)^{3/2} e^{-\frac{\mathbf{k}^2}{2\alpha}} \quad , \tag{1.7}$$

where $\alpha = mk_BT/\hbar^2$. In fact, this distribution is deduced assuming distinguishable particles and treating their respective momenta, $\mathbf{p}$'s, and positions, $\mathbf{r}$'s, as independent variables; as a consequence of this $n(\mathbf{k})$ does not depend on the interparticle interactions V($\mathbf{r}$). Therefore, it is straightforward to deduce with Eq. (1.7) the kinetic energy per particle for any classical system (second moment of the $n(\mathbf{k})$ distribution), which is equal to $\frac{3}{2}k_BT$ (in accordance with the Equipartition Theorem).

As far as one could expect, $n(\mathbf{k})$ in quantum systems is different from $n(\mathbf{k})^{MB}$ because of the non–commutability between the atomic momentum and position operators, and indistinguishability as well. Few experimental determinations of $n(\mathbf{k})$ in highly quantum systems are found to date (liquid and solid $^4\mathbf{He}$ [25, 26], liquid $\mathbf{Ne}$ [27] and $\mathbf{H}$ atoms in $\mathbf{KH_2PO_4}$ [28]). Due to its difficult extraction from scattering data, Quantum Monte Carlo methods

are at present the most suitable theoretical approaches to provide reliable knowledge on this subject [29, 10].

There are not physical arguments to predict the shape of $n(\mathbf{k})$ in a highly quantum solid. Recent experiments and theoretical predictions seem to rule out the possibility of a Gaussian form (made the exception of Ref. [29]). One illustrative example is yielded by solid ^{4}**He** at T$\sim$2 K, in which the experimental momentum distribution is observed to be more sharply peaked than a Gaussian due to larger occupations of the low momentum states [26].

Another special characteristic of quantum solids is their anharmonicity, which is assessed in the neutron-scattering experiments at high momentum transfer [30, 26]. Due to large excursions of the atoms around the crystalline sites, the repulsive region of the pair–interaction with the nearest neighbours is sampled, and subsequently, harmonic approximations of the mean potential felt by any particle become inaccurate [30]. In Figure 1.3 the mean potential felt by an arbitrary particle as a result of the interaction with the rest of the system, is schematically depicted around its equilibrium position. As can be observed in the figure, an harmonic assumption of such mean potential would inevitably be a too simple approximation.

Thermodynamic properties

Early in the development of Quantum Mechanics, the importance of quantum effects in the thermodynamics of solids at low temperature was recognized. The first successful attempt assumed the particles as simple points which interact each other through harmonic forces (Debye model). Subsequently, most of the theoretical efforts regarding the thermodynamic behaviour of solids at low temperature (Self-Consitent Phonon theory, $ab\ initio$ Molecular Dynamics, etc.) have been devoted to include realistic deviations from this harmonic model (anharmonic effects).

In 1912, P.J.W. Debye extended the Einstein model of solids by including the contributions of low–frequency phonons. Particles in this model are considered as points which interact through harmonic forces. The Hamiltonian of such a model allows certain linear coordinate transformations which decouple the system into a collection of $3N$ one–dimensional and non–interacting harmonic oscillators, with frequencies ranging from zero to the cut–off up-

$Crystal$	θ_D(K)
Diamond	2200
Titanium	420
Silver	225
Ice	192
Helium	25

Table 1.2: The Debye temperature, θ_D, corresponding to different substances [31] at 298 K. Helium's one corresponds to ^{4}**He** at 1 K [30].

per limit ω_D (Debye's frequency) [15]. The main achievement of this model is the T^3 dependence of the heat capacity in solids at low temperatures, and the Dulong-Petit law at high temperatures,

$$C_v^D = \begin{cases} \frac{12\pi^4}{5} N k_B \left(\frac{T}{\theta_D}\right)^3 & T \ll \theta_D \\ 3Nk_B & T \gg \theta_D \end{cases} \tag{1.8}$$

where N is the number of longitudinal phononic modes and θ_D is the Debye temperature. The Debye temperature yields the temperature at which thermal individual excitations and phononic collective excitations turn out to be of the same order,

$$\begin{aligned} \theta_D &= \frac{\hbar\omega_D}{k_B} \\ \omega_D^3 &= 18\pi^2\rho\left(\frac{1}{c_L^3} + \frac{2}{c_T^3}\right)^{-1} \end{aligned} \tag{1.9}$$

ρ being the particle density and c_L (c_T) the longitudinal (transverse) speed of sound. In Table 1.2, we have listed some crystals and their corresponding Debye temperature; it is observed that when atomic bonds become more constrained θ_D increases. This occurs because the speeds of sound appearing in equation (1.9) will increase if the compressibility of the material is decreased. Hence, from a thermodynamic point of view, quantum solids are characterized by low Debye temperatures, owing that the soft interaction among the atoms provides high compressibilities, and then, small speeds of sound.

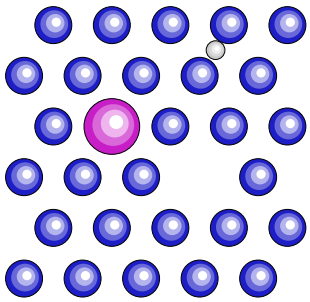

Figure 1.4: Schematic representation of various crystalline point defects (from top to bottom: interstitial, substitutional and vacancy).

Regarding the thermodynamics of the melting transition, quantum solids are also peculiar. In melting transitions, it is generally accepted the Lindemann's criterion, which asserts that the ratio between the radial mean squared vibrational amplitude and the interatom spacing, $\gamma = \langle u^2 \rangle^{1/2}/R$, is constant along the melting curve. However, this is not the case for helium, the quantum solid per excellence, where γ reduces as the melting pressure increases [30]. It is noted, however, that crystals in the middle–way between quantum and classical behaviour (**Ne** and **Ar**, for instance) still fit quiet correctly to the melting Lindemann's model [32].

Vacancies and other crystalline defects

Crystal defects (point, line and/or plane types) are easily created on quantum solids due to the large zero point motion of the atoms. Point defects such as vacancies (see Figure 1.4) have attracted special attention during the last decades; some theoretical calculations have suggested that they might exist on such solids even at absolute zero [33]. From a classical point of view this hypothesis has nonsense because it would imply a total non-zero entropy which would violate the third principle of thermodynamics.

Apart from this illustrative quantum–classical confrontation, other special features are expected from vacancies at ultralow temperatures. For instance, in solid ^{4}**He** the zero–point vacancies must behave like bosons, and therefore, could undergo a Bose–Einstein condensation (BEC). This reasoning leads to a plausible argument in favour of the aforementioned supersolid transition in ^{4}**He**. However experimental attempts focusing on the observation of such zero–point vacancies have not succeeded to date, owing to their extremely small concentration (x_0^{vac} <6·10^{-7}) and the low critical temperature required for their condensation (T_c <1.5 mK) [35].

It is worthwhile noticing the increasing of technological and fundamental interest in crystalline defects; these types of excitation are present in a great deal of quantum processes and different systems (crystal growing, semiconductors, optical excitations, etc.), which are being nowadays the objective of intensive research [36, 37].

1.2.2 Variational approach

Essentially, atomic pair-potentials are characterized by a strong repulsion at short distances (hard–core) which describes the overlap between electronic clouds of different atoms, and a weak attractive tail resulting from the dipole-dipole interaction at long distances (see Figure 1.5).

The variational approach is a well suited method for carrying out approximate calculations on the ground state of an interacting many–atom (or molecule) system. The advantages of this approach rely on two facts: 1) repulsive divergences coming from the interparticle interactions can be avoided with a careful choice of the trial wave function, which indeed must be null on there, and 2) the variational method provides upper bounds to the ground–state energy whose quality can be progressively improved by devising more and more accurate trial wave functions.

The trial wave function, ψ_T, depends on the degrees of freedom of the represented system (atomic positions, total spin, angular momentum,...), and contains some variational parameters to be optimized. This optimization relies on the variational principle, which asserts that the expectation value of a given Hamiltonian with an arbitrary wave function, ψ_T, will always exceed

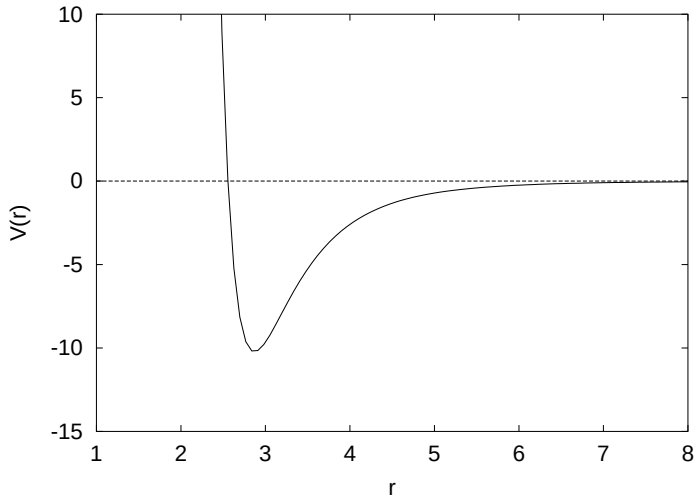

Figure 1.5: Atomic radial pair–potentials are characterized by a nearly hard–core at short distances and a weak attractive tail. In the figure, the Lennard-Jones potential for helium is represented ($V(r)$ is in K and distance r in Å).

the corresponding exact ground–state energy E_0 with exact wave function ϕ_0,

$$E_0 = \frac{\langle \phi_0 \mid H \mid \phi_0 \rangle}{\langle \phi_0 \mid \phi_0 \rangle} \leq \frac{\langle \psi_T \mid H \mid \psi_T \rangle}{\langle \psi_T \mid \psi_T \rangle} = E_T \quad . \tag{1.10}$$

In 1965, McMillan applied the method of random number generation from an arbitrary probability density function (proposed few years before by Metropolis *et al.* [1]) to the study of quantum systems for the first time [38]. This method, known as variational Monte Carlo (VMC), was first devised to investigate the liquid phase of $^4\mathbf{He}$, and nowadays it is widely used in a great variety of quantum problems (electronic structure [39], systems in confined geometries [40], nuclear physics [41], etc.).

The trial wave function proposed by McMillan was a Jastrow factor ψ_J [42, 43] expressed as a product of radial pair–correlation functions, f_2, depending

on the relative distances between the particles, $\{r_{ij}\}$,

$$\psi_J(\mathbf{r_1}, \mathbf{r_2}, ..., \mathbf{r_N}) = \prod_{j>i}^{N} \mathrm{f}_2(r_{ij}) \; . \tag{1.11}$$

He used a model,

$$\mathrm{f}_2(r_{ij}) = e^{-\frac{1}{2}\left(\frac{b}{r_{ij}}\right)^c} \tag{1.12}$$

which fits the asymptotic solution of the time–independent Schrödinger equation at short distances corresponding to the two–particle problem, assuming a Lennard–Jones (L–J) interaction,

$$V(r) = -4\epsilon \left[\left(\frac{\sigma}{r}\right)^6 - \left(\frac{\sigma}{r}\right)^{12} \right] \quad . \tag{1.13}$$

The function in (1.12) is hereafter referred to McMillan pair–correlation fac-

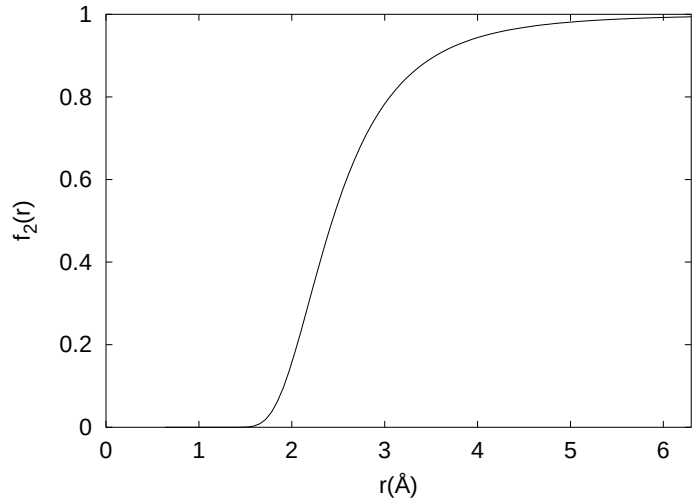

Figure 1.6: McMillan two-body correlation factor. The repulsive core of the potential is avoided approaching f_2 to zero at short distances.

tor (it can be also found in the literature referred to Schiff–Verlet factor). The zero cut–off and sharpness of f_2 are both controlled by the parameters b and c, respectively; for instance, in the case of bulk liquid ^{4}**He** near equilibrium

(σ=2.556Å and ϵ=10.22K), the values $b = 1.3\sigma$ and $c = 5$ yield the best variational energy quoted with ψ_J.

McMillan pair-correlation function has been widely used in the study of condensed matter systems using both L–J and more realistic potentials. The reason for this is that short–range correlations are treated in an accurate and feasible manner. The ground–state energy of liquid ^{4}**He**, for example, is around 2 K above the experimental result, which is -7.17 K [38].

Nevertheless, McMillan pair-correlation factor is manifestly not the optimal one because it does not deal with the middle and long–range correlations. An illustrative example of this is provided once again by helium, where the asymptotic dependence of the static–structure factor, $S(k)$, when $k \to 0$ is Ak (A being a constant) , which implies the behaviour $\mathrm{f}_2(r) \to 1 - A/r^2$ when $r \to \infty$, not included in function (1.12).

The full way to obtain the optimal pair–correlation factor would imply to solve the Euler-Lagrange equation

$$\frac{\delta \langle H \rangle}{\delta \mathrm{f}_2(r)} = 0 \tag{1.14}$$

through an iterative and self–consistent procedure. It has been shown [44] that the solution of Eq.(1.14) integrates optimal intermediate and long-range behaviours; however, the gain in the binding energy per particle with respect to (1.12) is not large (approximately 0.2 K in ^{4}**He**).

Among the various proposals for improving f_2, we remark the one proposed by Reatto [45] which incorporates approximately middle-range structure through the expression

$$\mathrm{f}_2(r) = \exp\left[-\frac{1}{2}\left(\frac{b}{r}\right)^5 - \frac{L}{2}\exp\left[-\left(\frac{r-\lambda}{\Lambda}\right)^2\right]\right] \quad , \tag{1.15}$$

λ, b and Λ being variational parameters.

Apart from improving the variational description by modifying the pair–correlation factor, one may introduce higher–order correlation factors,

$$\psi_{JT}(\mathbf{r_1}, \mathbf{r_2}, ..., \mathbf{r_N}) = \prod_{i<j}^{N} \mathrm{f}_2(r_{ij}) \prod_{i<j<k}^{N} \mathrm{f}_3(r_{ij}, r_{ik}, r_{jk}) \; . \tag{1.16}$$

This approach was first pursued for liquid $^4\mathbf{He}$ by Chang and Campbell in the framework of Correlated Basis function theory (CBF) [46]; the improvement in the energy introduced by (1.16) was variationally calculated giving an upper bound only 5% higher than experiment. Variational estimations of the ground–state energy in solid helium are also notably improved by the introduction of three–body correlation factors [48].

Some of the QMC techniques used to simulate bulk systems demand the explicit declaration of the condensed phase to be studied, contrarily to classical simulations or other fully quantum approaches. Indeed, this implies that quantum solids and liquids belonging to the same chemical species are simulated differently; in our case, this is accomplished through the specific form of the trial wave function. In the case of solids, the most widespread used trial wave function presents the form of a localized Jastrow factor, ψ_{JG}, which is commonly referred in the literature to the Nosanow–Jastrow model,

$$\psi_{JG}(\mathbf{r_1}, \mathbf{r_2}, ..., \mathbf{r_N}) = \prod_{i>j}^{N} \mathrm{f}_2(r_{ij}) \prod_{i}^{N} \mathrm{g}_1(|\mathbf{r_i} - \mathbf{R_i}|) \; . \tag{1.17}$$

Early in the 60's Nosanow suggested this function to deal with solids [49], and few years later, Hansen and Levesque carried out the first variational Monte Carlo calculation in crystal $^4\mathbf{He}$ and $^3\mathbf{He}$ with it [50, 51]. The f_2 factors in (1.17) are adopted in the form of (1.12), and the one–body factors g_1 usually are expressed as Gaussians,

$$\mathrm{g}_1(|\mathbf{r_i} - \mathbf{R_i}|) = e^{-\frac{1}{2}a(|\mathbf{r_i}-\mathbf{R_i}|)^2} \; . \tag{1.18}$$

These one–body factors introduce the position of the crystalline lattices (sites) defined by the vectors $\{\mathbf{R_i}\}$, and localize the particles around them. On the other hand, the pair-correlation factors $\mathrm{f}_2(r)$ correlate the relative motion between pairs of atoms as in liquids.

The variational parameter in $\mathrm{g}_1(r)$, a, is related to the mean squared displacement of the particles from their equilibrium positions. If two–body correlation factors are not included in ψ_{JG}, the resulting trial wave function corresponds to the exact solution of N uncorrelated particles moving around positions $\{\mathbf{R_i}\}$ under the effect of an external harmonic trap of frequency ω=$\frac{\hbar a}{m}$. In this case, the mean squared displacement corresponding to any particle is

$$\left\langle \mathbf{u^2} \right\rangle = \frac{1}{N} \sum_{i=1}^{N} \frac{\int (\mathbf{r_i} - \mathbf{R_i})^2 e^{-\frac{1}{2}a(\mathbf{r_i}-\mathbf{R_i})^2} d\mathbf{r_i}}{\int e^{-\frac{1}{2}a(\mathbf{r_i}-\mathbf{R_i})^2} d\mathbf{r_i}} \approx \frac{3\sqrt{3}}{\sqrt{\pi}a} \quad , \tag{1.19}$$

which depends inversely on the parameter a. According to this uncorrelated model, when the Gaussian factors are stressed (a is increased), the mean squared displacement (1.19) would decrease and the kinetic energy per particle (equal to the harmonic one $\langle E_k \rangle^{harm} = \frac{3}{4}\hbar\omega$) would increase (consistent with the uncertainty principle of Heisenberg (1.4)). Otherwise, if the Gaussian factors are spread (a is decreased) the mean squared displacement would increase and the particles would become less localized. However, although the g_1 factors by themselves can reproduce some of the main features in quantum solids, pair–correlation factors are required to yield their trustworthy description.

When attention is paid to equation (1.17), one realizes that ψ_{JG} is neither symmetric nor antisymmetric under particle exchanges, and also, that translational invariance is missing. Taking into account the arguments exposed in the previous subsections, one must realize that these mathematical properties are physically incorrect:

$$\begin{aligned} \psi_{JG}\left(\mathbf{r_1}, \mathbf{r_2}, ..., \mathbf{r_N}\right) &\neq \psi_{JG}\left(\mathbf{r_2}, \mathbf{r_1}, ..., \mathbf{r_N}\right) \\ \psi_{JG}\left(\mathbf{r_1}, \mathbf{r_2}, ..., \mathbf{r_N}\right) &\neq \psi_{JG}\left(\mathbf{r_1} + \mathbf{R}, \mathbf{r_2} + \mathbf{R}, ..., \mathbf{r_N} + \mathbf{R}\right) \ . \end{aligned}$$

Nevertheless, it has been checked variationally in several crystalline systems that this lack of symmetrization of the trial wave function does not affect the calculations of the static properties, as for example the energy and related thermodynamics functions [52, 10]. This occurs because exchange of particles in bosonic solids are relatively infrequent, and also, because their contribution to the total energy is worthless (on the scale of mK).

Several variational approaches have focused on the design of trial wave functions for solids correctly symmetrized [52, 53, 54]. In the case of bosonic solids, the first proposal, in analogy with the Slater determinant for fermions, is a permanent of g_1 factors

$$\sum_{\{\sigma_i\}} \mathrm{g}_1\left(|\mathbf{r_1} - \mathbf{R}_{\sigma_1}|\right) \mathrm{g}_1\left(|\mathbf{r_2} - \mathbf{R}_{\sigma_2}|\right) \cdots \mathrm{g}_1\left(|\mathbf{r_N} - \mathbf{R}_{\sigma_N}|\right) \quad , \tag{1.20}$$

where the summation runs about all possible permutations of particles among the sites of the lattice. However, the present state of the art in the computation of an NxN permanent is still rather demanding for our purposes ($2^{N-1}N$ operations per permanent [55]) making this option not manageable in practice.

A possible solution to this problem is provided by the Shadow Wave Function formalism (SWF) [53], which introduces some subsidiary (shadow) variables in the trial wave function in order to avoid the explicit introduction of a lattice structure,

$$\begin{aligned} \psi_T^{SWF}(\mathbf{r}) &= \int \Omega(\mathbf{r},\mathbf{S})\, d\mathbf{S} \\ \Omega(\mathbf{r},\mathbf{S}) &= \exp\left[-\frac{1}{2}\sum_{i<j} u(r_{ij}) - \sum_k \phi(\mathbf{r_k}-\mathbf{s_k}) - \sum_{l<m} v(s_{lm})\right]. \end{aligned} \quad (1.21)$$

In equation (1.21) $u(r)$ and $v(s)$ are functions which describe separately the correlations between the real and shadow particles, while $\phi(z)$ accounts for the mixed real–shadow interactions. This approach provides only a gain of few tenths of K in the variational binding energy of solid ^{4}**He** respect to the ψ_{JG} case. Unfortunately, the sampling of the trial wave function ψ_T^{SWF} is very time–consuming, and contrarily to ψ_{JG}, its present range of applicability is restricted to the variational level.

Chapter 2
Quantum Monte Carlo methods

In this chapter we present an introduction to the variational Monte Carlo (VMC) and diffusion Monte Carlo (DMC) methods, which are the main computational tools used to obtain the results reported on this work.

The term Quantum Monte Carlo (QMC) covers several techniques which are aimed to describe the quantum states of an interacting N–body system. Common strategies range from providing approximate values of the total ground–state energy up to solve the imaginary–time dependent Schrödinger equation. The general approach adopted in QMC calculations is stochastic. For instance, the DMC strategy relies on successive iteration of short–time approximations for the N–body Green's function. On the other hand, VMC implements efficiently the evaluation of multidimensional integrals based on trial models for the wave function and the variational principle.

Some basic elements of probability theory and random number generation are put forward in section 2.1. In the same section, we introduce the concept of importance sampling, devised to improve the sampling efficiency, and the general Metropolis algorithm. Next on, in sections 2.2 and 2.3, we properly described the VMC and DMC methods and attach pseudocodes of both methods. Finally, in section 2.4 we explain the pure estimator technique which allows for exact estimations of any operator which does not commute with the Hamiltonian.

2.1 Introduction to MC methods

Generally, physical problems which can be tied to a probability density function (pdf) are treated with simulation when the complexity in solving them is quite demanding (i.e. the number of independent variables is rather large). In a general sense, simulation means to evolve the physical system of interest statistically, that is, according to one (or several independent) pdf(s). Therefore, once a problem is mathematically modelized the central issue of simulation is to provide successive sequences of random numbers generated according to the pdf(s) governing it.

2.1.1 Random walks and the Metropolis algorithm

Let's consider a general pdf, $f(x)$, depending on a continuous variable x defined in the $\Re$-space. It is assumed that the analitycal form of $f(x)$ is known and that it is linked to some problem we want to solve with simulation. Then, the arising question is : how can one generate sequences of random numbers according to $f(x)$?. By *sequences of random numbers generated according to f(x)* we mean that if we construct an histogram with the numbers obtained in the simulation, $\{x_1, x_2, ..., x_N\}$ (assuming $N \to \infty$), the height of each box centered on x_i (width $\Delta x << 1$) would be proportional to the probability $f(x_i)\Delta x_i$ (see Figure 2.1).

Basically, there are two strategies to do this: a direct estimation, based on change of variables, and the Metropolis algorithm. In this subsection, we only comment the second one which is the more general and allows the sampling of multivariate functions (see p.e. Ref. [59] for a comprehensive explanation of the first). The Metropolis algorithm [1], also known as the MR^2T^2 method, is presented next without performing its rigorous proof; the objective of the present subsection is mainly descriptive. Straightforward and tutorial reviews on the topic can be found in References [2, 59, 60].

The Metropolis method starts assuming an initial value of the x variable. As a requirement, we must be able to generate random movements from a certain transition probability distribution $T(x \to x')$. Such transition probability distribution fixes the probability for moving from point x to x' within an allowed interval $[0, L]$. In fact, some computational routines of random number generation [61], may fulfill the proper conditions of transition probability

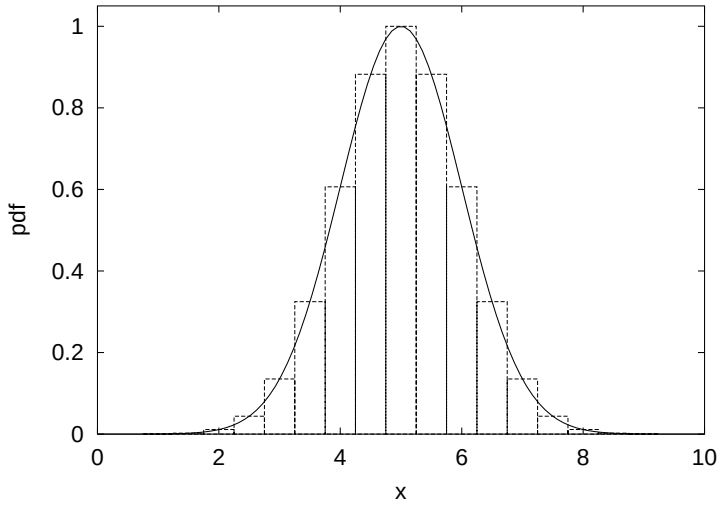

Figure 2.1: Histogram concerning a serie of radom numbers (boxes) generated according to a Gaussian pdf (solid line). The width of the boxes in the graphic have not been assumed $\Delta x << 1$ in virtue of a better understanding.

distribution; one trivial example is built up with the uniform pdf (hereafter referred to U(0,L)), which generates any real number within the interval $[0, L]$ with equal probability, that is, $T(x \to x') = 1/L$.

Let's assume a certain value of the variable x, namely x_i. Then, the next random point in the sampling of $f(x)$, x_{i+1}, is generated according to (Metropolis step):

$\longrightarrow$ *Generate a random shift of the variable x from T(*$x \to x'$*),*

$$x' = x_i + \zeta$$

$\longrightarrow$ *Accept the trial move to* x' *with probability*

$$A(x_i \to x') = \min\left(1, \tfrac{f(x')T(x' \to x_i)}{f(x_i)T(x_i \to x')}\right)$$

$\longrightarrow$ *If* x' *is accepted* $x_{i+1} = x'$*, otherwise* $x_{i+1} = x_i$

The acceptation step is easily carried out by comparing $A(x \to x')$ with an arbitrary output, ϵ, of the uniform distribution U(0,1) : if $A(x \to x') > \epsilon$ accept x', otherwise reject it.

After an equilibration period, a probabilistic steady equilibrium in the x–space must be reached. This equilibrium implies that the probability of going from position x to position x' must be equal to the probability of going from position x' to position x (detailed balance condition)

$$f(x)P(x \to x') = f(x')P(x' \to x) \ , \tag{2.1}$$

where $P(a \to b) = T(a \to b)A(a \to b)$ is the probability of proposing movement $a \to b$ and then accept it.

Certainly, from equation (2.1) it is deduced the complementary condition

$$\frac{A(x \to x')}{A(x' \to x)} = \frac{T(x' \to x)f(x')}{T(x \to x')f(x)} \tag{2.2}$$

which is properly accomplished by the acceptance distribution $A(x \to x')$ proposed in the previous sketch. It is worth noticing that in most cases the use of symmetric probability distributions, that is $T(x \to x') = T(x' \to x)$, could result advantageous from a computational point of view, owing that $A(x \to x')$ reduces to $\min(1, f(x')/f(x))$ and the random displacements are easily generated with the uniform or Gaussian distributions.

Concerning the technical aspects of the simulation, it is mandatory to take into account the acceptance rate of the proposals to discern if the sampling is being effective or not. A common agreement is that it should be ranged between 50-75%.

Despite we have restricted the above description to the one–variable case $f(x)$, the Metropolis method is in fact the best suited strategy (if not the only) to sample multivariate functions ($f(\mathbf{R})$, where $\mathbf{R} = \{x_1, x_2, ..., x_N\}$). The increase in the number of variables does not imply more involved calculations, just additional computational effort, since the move of each variable is applied independently and the collective displacement $\mathbf{R} \to \mathbf{R}'$ is accepted or rejected according to $A(\mathbf{R} \to \mathbf{R}') = \min\left(1, \frac{f(\mathbf{R}')T(\mathbf{R}' \to \mathbf{R})}{f(\mathbf{R})T(\mathbf{R} \to \mathbf{R}')}\right)$.

2.1.2 MC integration and importance sampling

MC methods are well suited tools for computing integrals.

$$I = \int_a^b h(x)dx \tag{2.3}$$

From the MC point of view, the definite integral in Eq.(2.3) is estimated through the mean value of function $h(x)$ over a set of points $\{x_1, x_2, ..., x_M\}$ generated from the U(a,b) distribution.

$$I = \int_a^b h(x)dx \approx \frac{1}{M}\sum_{i=1}^{M} h(x_i) \tag{2.4}$$

The crude MC estimation (2.4) would become exact if M was infinite. However, this is never the case and as any statistical estimation requires we must compute its variance , σ_I, to get a qualitative idea of its accuracy.

$$\sigma_I^2 = \frac{1}{(M-1)}\left[\left(\frac{1}{M}\sum_{i=1}^{M} h(x_i)^2\right) - \left(\frac{1}{M}\sum_{i=1}^{M} h(x_i)\right)^2\right] \tag{2.5}$$

Importance sampling in MC is a strategy devised to decrease this variance by making the sampling of I more effective. Basically, it consists in dividing and multiplying the integrand $h(x)$ by a new pdf $f(x)$.

$$I = \int_a^b h(x)dx = \int_a^b \left(\frac{h(x)}{f(x)}\right) f(x)dx \approx \frac{1}{M}\sum_{i=1}^{M}\left(\frac{h(x_i)}{f(x_i)}\right) \tag{2.6}$$

Now, in expression (2.6), the set of points $\{x_1, x_2, ..., x_M\}$ is not generated from U(a,b) but from the new pdf $f(x)$. It can be proved analytically that as far as $f(x)$ resembles to $h(x)$, while maintaining constant M, the variance reduces [62]. Another advantage of importance sampling with respect to crude MC integration, is that the integral of an arbitrary integrand containing some singularities can be computed by choosing $f(x)$ conveniently.

2.2 Variational Monte Carlo (VMC)

The VMC is an approximate method which relies on the variational principle,

$$E_T = \frac{<\psi_T|\mathrm{H}|\psi_T>}{<\psi_T|\psi_T>} \geq E_0 \tag{2.7}$$

where E_0 is the exact ground–state energy corresponding to the Hamiltonian H, and ψ_T is the function proposed to mimic its ground state (trial wave function, twf). In fact, the accuracy of variational calculations depend enterely on the resemblance between the trial wave function and the true (though unknown) ground state. Generally, ψ_T is expressed in terms of some parameters that may be chosen in virtue of total energy (and/or energy variance) minimization: the lower the associated trial energy E_T is, the better energy description of the system is attained.

The VMC strategy relies on the computation of ground–state properties expressed in the appropriate integral form

$$E_T = \int \psi_T \mathrm{H} \psi_T^* d\mathbf{R} = \int E_L(\mathbf{R}) |\psi_T|^2 d\mathbf{R} = \frac{1}{M} \sum_i^M E_L(\mathbf{R_i}). \tag{2.8}$$

Making use of the contents exposed in the previous section, equation (2.8) turns out to be understandable: the total energy E_T is calculated by evaluating the local energy estimator, $E_L(\mathbf{R}) = \mathrm{H}\psi_T/\psi_T$, in each of the random points generated according to the probability distribution $|\psi_T|^2$. This approach results feasibly affordable with the Metropolis algorithm, since ψ_T is a multivariate real function depending on the positions of the N particles conforming the quantum system under study.

The VMC method is then doubly–valued. On one hand it provides physical insight of the quantum system, and on the other, selects good-quality trial wave functions required for effective samplings in more involved methods like for example diffusion Monte Carlo.

The following is a general sketch describing a VMC step,

$\longrightarrow$ *Assume an initial point* $\mathbf{R} = \{x_1, x_2, ..., x_N\}$

$\longrightarrow$ *Propose a symmetric move of the system,* $\mathbf{R} \rightarrow \mathbf{R'}$

$\longrightarrow$ *Evaluate the acceptance factor* $A\left(\mathbf{R} \rightarrow \mathbf{R}'\right) = \min\left(1, \frac{|\psi_T(\mathbf{R}')|^2}{|\psi_T(\mathbf{R})|^2}\right)$

$\longrightarrow$ *Apply Metropolis accept/reject criterion*

$\longrightarrow$ *If accept update positions* $(\mathbf{R}' \rightarrow \mathbf{R})$*, otherwise continue*

$\longrightarrow$ *Calculate local energy* $E_L\left(\mathbf{R}\right)$

$\longrightarrow$ *Accumulate statistics and go to the next step.*

After iterating some VMC steps a steady probabilistic equilibrium is reached. From then on, one accumulates statistics to estimate E_T correctly.

2.3 Diffusion Monte Carlo (DMC)

DMC is a method which enables us to calculate the exact ground–state energy and related eigenvalues of the many–particle system of interest at zero temperature. The DMC technique is based on a short–time approximation for the Green's function corresponding to the imaginary time-dependent Schrödinger equation, which is solved up to a certain order of accuracy within an infinitesimal interval $\Delta\tau$. This method is simpler than domain Green function Monte Carlo [7, 8], but contrarily presents some $(\Delta\tau)^n$ bias coming from the factorization of the imaginary time propagator $e^{-\frac{\Delta\tau}{\hbar}\mathrm{H}}$.

The simplest DMC implementation (linear DMC, accurate up to order $(\Delta\tau)^2$) presents a systematic $\Delta\tau$ bias which is removed by studying the linear dependence of the results with $\Delta\tau$, and then extrapolating to $\Delta\tau \rightarrow 0$. However, second-order algorithms (Quadratic Diffusion Monte Carlo -QDMC-, accurate up to order $(\Delta\tau)^3$) control more efficiently the time-step bias in the sense that the $\Delta\tau \rightarrow 0$ extrapolation is nearly eliminated by choosing a sufficiently small $\Delta\tau$.

Some years ago, Chin [56] developed and proved the quadratic efficiency of second-order propagators in several models. Since then, this quadratic DMC approach has been used in the microscopic study of quantum fluids and solids, mainly $^{\mathbf{4}}\mathbf{He}$ [57] and $^{\mathbf{3}}\mathbf{He}$ [58], and it is the one implemented in our codes. In the following, the DMC method is described with some detail

putting special emphasis on the particular QDMC case.

Given an arbitrary Hamiltonian, H, expressed in the form

$$\mathrm{H} = -\sum_{i=1}^{N} \frac{\hbar^2}{2m_i}\nabla_i^2 + \sum_{i<j}^{N} V(r_{ij}) + \sum_{i=1}^{N} V_{ext}(\mathbf{r}_i) \ , \tag{2.9}$$

where m_i is the mass of the i^{th} particle, $V(r_{ij})$ the interparticle interaction and $V_{ext}(\mathbf{r})$ an external potential field, the corresponding Schrödinger equation is

$$i\hbar\frac{\partial\Psi(\mathbf{R},t)}{\partial t} = (\mathrm{H} - E)\,\Psi(\mathbf{R},t) \quad , \tag{2.10}$$

where $E \approx E_0$ is a constant. This equation can be formally solved by expanding the solution $\Psi(\mathbf{R},t)$ in the basis set of eigenfunctions $\{\phi_n\}$

$$\Psi(\mathbf{R},t) = \sum_{n=0}^{\infty} c_n e^{-\frac{it}{\hbar}(E_n - E)}\phi_n\left(\mathbf{R}\right) \tag{2.11}$$

where

$$\mathrm{H}\phi_n = E_n\phi_n \quad . \tag{2.12}$$

Indeed, when equation (2.10) is solved in imaginary time, that is $\tau = it$, the corresponding solution (2.11) would tend to the ground state ϕ_0 for an infinite imaginary time, $\tau \to \infty$, because the rest of the terms within the summatory would vanish ($E_n > E$ if $n \neq 0$),

$$\lim_{\tau\to\infty} \Psi\left(\mathbf{R},\tau\right) \to c_0\phi_0 \quad . \tag{2.13}$$

At the same time, the expected value of the Hamiltonian also would tend to the ground–state value E_0.

$$\lim_{\tau\to\infty} \frac{\langle\Psi|\mathrm{H}|\Psi\rangle}{\langle\Psi|\Psi\rangle} = \frac{\langle\phi_0|\mathrm{H}|\phi_0\rangle}{\langle\phi_0|\phi_0\rangle} = E_0 \tag{2.14}$$

Making use of the hermiticity of the Hamiltonian, it is stated that

$$\frac{\langle\phi_0|\mathrm{H}|\phi_0\rangle}{\langle\phi_0|\phi_0\rangle} = \frac{\langle\phi_0|\mathrm{H}|\psi_T\rangle}{\langle\phi_0|\psi_T\rangle} \quad , \tag{2.15}$$

where ψ_T it is a convenient trial wave function. Hence, the ground–state energy in the configurational space of the particles, $\mathbf{R} = \{\mathbf{r_1}, \mathbf{r_2}, ..., \mathbf{r_N}\}$, is calculated by solving the integral

$$E_0 = \lim_{\tau \to \infty} \int_V E_L(\mathbf{R}) f(\mathbf{R}, \tau) \, d\mathbf{R} \tag{2.16}$$

where $f(\mathbf{R}, \tau) = \Psi(\mathbf{R}, \tau) \psi_T(\mathbf{R})$, and $E_L(\mathbf{R})$ is the local energy defined as

$$E_L(\mathbf{R}) = \frac{\mathrm{H}\psi_T(\mathbf{R})}{\psi_T(\mathbf{R})} \quad . \tag{2.17}$$

The introduction of $\psi_T(\mathbf{R})$ in $f(\mathbf{R}, \tau)$ corresponds to importance sampling which, in fact, improves the accuracy in the computation of the integral (2.16) by introducing explicitly that $\psi_T(\mathbf{R}) = 0$ when $r_{ij} \leq \sigma$ (core of the interatomic interaction).

From (2.10) it is derived the imaginary time evolution of the probability distribution function $f(\mathbf{R}, \tau)$ (making $\hbar = m_i = 1$),

$$-\frac{\partial f(\mathbf{R}, \tau)}{\partial \tau} = -\frac{1}{2} \nabla^2_{\mathbf{R}} f(\mathbf{R}, \tau) + \frac{1}{2} \nabla_{\mathbf{R}} (\mathbf{F}(\mathbf{R}) f(\mathbf{R}, \tau)) + (E_L(\mathbf{R}) - E) f(\mathbf{R}, \tau) \quad , \tag{2.18}$$

where $\mathbf{F}(\mathbf{R}) = 2\psi_T(\mathbf{R})^{-1} \nabla \psi_T(\mathbf{R})$ is called the drift force, in spite of having velocity units. Equation (2.18), therefore, can be rewritten in the form of three operators, $\{O_i\}$, acting on the function $f(\mathbf{R}, \tau)$

$$-\frac{\partial f(\mathbf{R}, \tau)}{\partial \tau} = (O_1 + O_2 + O_3) f(\mathbf{R}, \tau) \equiv O f(\mathbf{R}, \tau) \quad . \tag{2.19}$$

The imaginary time evolution of the pdf $f(\mathbf{R}, \tau)$ can also be expressed within the Green's function formalism in the form

$$f(\mathbf{R}, \tau + \Delta\tau) = \int G\left(\mathbf{R}, \mathbf{R}', \Delta\tau\right) f\left(\mathbf{R}', \tau\right) d\mathbf{R}' \quad , \tag{2.20}$$

where $G\left(\mathbf{R}, \mathbf{R}', \tau\right)$ is defined as

$$G\left(\mathbf{R}, \mathbf{R}', \tau\right) = \left\langle \mathbf{R} | e^{-O\tau} | \mathbf{R}' \right\rangle \tag{2.21}$$

and which is interpreted as the probability distribution governing the transition of the system $\mathbf{R}' \to \mathbf{R}$ in an imaginary time interval τ.

The basic strategy underlying the DMC method consists in breaking the whole Green's function into several factors, $G\left(\mathbf{R},\mathbf{R}^{'},\Delta\tau\right)$, which are analytically known.

In virtue of the Baker–Campbell–Hausdorff formula

$$e^{-(A+B)\Delta\tau}=e^{-A\Delta\tau}e^{-B\Delta\tau}e^{-C\Delta\tau^{2}} \quad , \tag{2.22}$$

where $C\equiv 1/2[B,A]-\Delta\tau\left(1/6[B,[B,A]]-1/3[[B,A],A]\right)+\cdots$, and the brackets represent $[A,B]=AB-BA$, the bias provided by the factorization of $G\left(\mathbf{R},\mathbf{R}',\tau\right)$ may be deduced in the form of some power of $\Delta\tau$.

The simplest factorization performed in (2.21) corresponds to,

$$e^{-O\Delta\tau}=e^{-O_{1}\Delta\tau}e^{-O_{2}\Delta\tau}e^{-O_{3}\Delta\tau}+\epsilon\left((\Delta\tau)^{2}\right) \tag{2.23}$$

which generates an error linearly dependent with the time step (linear DMC).

Concerning our work, we have implemented second order algorithms (QDMC) with the aim of increasing the computational efficiency. One possible quadratic factorization of the imaginary time propagator $e^{-O\Delta\tau}$ is

$$\begin{aligned} e^{-O\Delta\tau}=e^{-O_{1}\frac{\Delta\tau}{2}}e^{-O_{2}\frac{\Delta\tau}{2}}e^{-O_{3}\Delta\tau}\times \\ e^{-O_{2}\frac{\Delta\tau}{2}}e^{-O_{1}\frac{\Delta\tau}{2}}+\epsilon\left((\Delta\tau)^{3}\right) \quad , \end{aligned} \tag{2.24}$$

which written in the integral form becomes

$$\begin{aligned} f\left(\mathbf{R},\tau+\Delta\tau\right)=\int\left(G_{1}\left(\mathbf{R},\mathbf{R_{1}},\frac{\Delta\tau}{2}\right)G_{2}\left(\mathbf{R_{1}},\mathbf{R_{2}},\frac{\Delta\tau}{2}\right)G_{3}\left(\mathbf{R_{2}},\mathbf{R_{3}},\Delta\tau\right)\times\right. \\ \left.G_{2}\left(\mathbf{R_{3}},\mathbf{R_{4}},\frac{\Delta\tau}{2}\right)G_{1}\left(\mathbf{R_{4}},\mathbf{R}^{'},\frac{\Delta\tau}{2}\right)\right)f\left(\mathbf{R}^{'},\tau\right)d\mathbf{R_{1}}...d\mathbf{R_{4}}d\mathbf{R}^{'} \quad . \end{aligned} \tag{2.25}$$

The $\{G_i\}$ functions in (2.25) are the Green functions corresponding to the differential equations

$$-\frac{\partial f\left(\mathbf{R},\tau\right)}{\partial\tau}=O_{i}f\left(\mathbf{R},\tau\right) \quad , \tag{2.26}$$

where the operators $\{O_i\}$ are defined in Eq.(2.19).

In the first case, G_1 describes an isotropic and Gaussian diffusion of the particles (kinetic propagator)

$$G_1\left(\mathbf{R},\mathbf{R}^{'},\tau\right)=(4\pi D\tau)^{-\frac{3N}{2}}\exp\left(-\frac{\left(\mathbf{R}-\mathbf{R}^{'}\right)^2}{4D\tau}\right) \quad . \tag{2.27}$$

On the other hand, G_2 corresponds to a deterministic movement guided by the drift force $\mathbf{F}(\mathbf{R})$

$$G_2\left(\mathbf{R},\mathbf{R}^{'},\tau\right)=\delta\left(\mathbf{R}-\mathbf{R}^{'}(\tau)\right) \tag{2.28}$$

where the evolution of $\mathbf{R}^{'}$ is governed by

$$\begin{cases}\mathbf{R}^{'}(0)=\mathbf{R}^{'}\\ \frac{d\mathbf{R}^{'}(\tau)}{d\tau}=D\mathbf{F}\left(\mathbf{R}^{'}(\tau)\right)\end{cases} \quad . \tag{2.29}$$

It is worth noticing, that equation (2.29) must be also solved up to order $(\Delta\tau)^3$ to ensure the quadratic convergence of the algorithm.

The third Green function, G_3, is known as the branching factor and it associates to each walker (configuration) a certain weight dependent on its local energy.

$$G_3\left(\mathbf{R},\mathbf{R}^{'},\tau\right)=exp\Big(-\left(E_L(\mathbf{R}^{'})-E\right)\tau\Big)\delta\left(\mathbf{R}-\mathbf{R}^{'}\right) \tag{2.30}$$

In this way, each walker is replicated if its local energy is close enough to the ground state or killed otherwise.

Next, we present the general time evolution which follows an arbitrary walker, $\mathbf{R}_0$, within a certain time step $\Delta\tau$ in our QDMC algorithm. The full simulation of the system is equivalent to iterate this sketch for each walker, as many times as necessary, in order to reach the asymptotic ground state and accumulate statistics on it (τ^{sim}=N$\Delta\tau$ being N$\rightarrow\infty$). The magnitudes E_L^0 and $D=\hbar^2/2m$ are the initial walker's local energy and the diffusion constant, while the int(α) function outputs the integer part of the real number α.

$\longrightarrow$ *Walker* $\mathbf{R}_0$ *is shifted by* $\mathbf{G}$ *according to the pdf* $\exp(-\mathbf{G}^2/4D\Delta\tau)$

$$\mathbf{R}_1=\mathbf{R}_0 + \mathbf{G}$$

$\longrightarrow$ *Drift force is calculated at* $\mathbf{R}_1$, $\mathbf{F}(\mathbf{R}_1)$

$\longrightarrow$ *Configuration* $\mathbf{R}_2$ *is calculated with the drift force* $\mathbf{F}(\mathbf{R}_1)$

$$\mathbf{R}_2 = \mathbf{R}_1 + D\frac{\Delta\tau}{2}\mathbf{F}(\mathbf{R}_1)$$

$\longrightarrow$ *Drift force is calculated at* $\mathbf{R}_2$, $\mathbf{F}(\mathbf{R}_2)$

$\longrightarrow$ *Configuration* $\mathbf{R}_1$ *is displaced to* $\mathbf{R'}_2$

$$\mathbf{R'}_2 = \mathbf{R}_1 + D\frac{\Delta\tau}{2}\left(\frac{\mathbf{F}(\mathbf{R}_1)+\mathbf{F}(\mathbf{R}_2)}{2}\right)$$

$\longrightarrow$ *Local energy* E_L*, drift force and other properties are calculated at* $\mathbf{R'}_2$

$\longrightarrow$ *Configuration* $\mathbf{R}_1$ *is displaced with the drift force* $\mathbf{F}(\mathbf{R'}_2)$

$$\mathbf{R}_3 = \mathbf{R}_1 + D\Delta\tau\mathbf{F}(\mathbf{R'}_2)$$

$\longrightarrow$ *Branching factor* n_w *is calculated*

$$n_w = \exp\left(-\Delta\tau\left(\frac{E_L+E_L^0}{2} - E\right)\right)$$

$\longrightarrow$ *Walker* $\mathbf{R}_3$ *is replicated with probability* int(n_w + U(0,1))

$\longrightarrow$ *If walker is replicated : each offspring is initialized* $\mathbf{R}_0$=$\mathbf{R}_3$

$\longrightarrow$ *If walker is not replicate : finish*

It is worthwhile noticing that the total number of walkers will vary along the simulation due to the killing/replication processes. Though this, the total population of walkers must be periodically normalized to some limit number

in order to avoid its monotonous growth and the subsequent loss of computational effectiveness. Finally, the value of E found in n_w corresponds to the mean local energy of the walkers present in the previous time step; in this way, the replication of the better gifted walkers is reinforced while punished on the contrary.

2.4 Pure and mixed estimators

As it has been established in the previous section, the DMC method is an excellent technique devised to compute exact ground–state energies. Once the asymptotic limit ($\tau \rightarrow \infty$) is reached, the sampling of the integrals is performed with the distribution function $\phi_0\psi_T$ instead of $\mid \phi_0 \mid^2$. In the estimation of the energy this does not introduce any bias. Unfortunately, if $[O, \mathrm{H}] \neq 0$ equations (2.14) and (2.15) become vaguely incorrect when the operator O substitutes the Hamiltonian. As a consequence, the estimator

$$\langle O(\mathbf{R})\rangle_m = \frac{\langle \phi_0 | O(\mathbf{R}) | \psi_T\rangle}{\langle \phi_0 | \psi_T\rangle} = \frac{1}{M}\sum_{i=1}^{M} O(\mathbf{R}_i) \ , \tag{2.31}$$

known as the mixed estimator, is to some extend biased by the trial wave function ψ_T (as it can be proved considering $|\phi_0\rangle = |\psi_T\rangle + \delta|\psi_T\rangle$ in the above equation). A more accurate estimation of $\langle O(\mathbf{R})\rangle$ is provided by

$$\langle O(\mathbf{R})\rangle_e = 2\langle O(\mathbf{R})\rangle_m - \langle O(\mathbf{R})\rangle_v \tag{2.32}$$

which is called the extrapolated estimator and involves the knowledge of the mixed (2.31) and variational (2.33) ones.

$$\langle O(\mathbf{R})\rangle_v = \frac{\langle \psi_T | O(\mathbf{R}) | \psi_T\rangle}{\langle \psi_T | \psi_T\rangle} \tag{2.33}$$

The expected value obtained through equation (2.32) also depends on the trial wave function used for the importance sampling [57]; despite it results more reliable than $\langle O(\mathbf{R})\rangle_m$ when both are calculated with the same ψ_T, its error is still not predictable (of order $\delta^2|\psi_T\rangle$).

In order to remove the bias introduced by ψ_T one has to tackle the exact, or also called pure, estimation

$$\langle O(\mathbf{R})\rangle_p = \frac{\langle\phi_0|O(\mathbf{R})|\phi_0\rangle}{\langle\phi_0|\phi_0\rangle} \quad , \tag{2.34}$$

which can be expressed in the form

$$\langle O(\mathbf{R})\rangle_p = \frac{\left\langle\phi_0|O(\mathbf{R})\frac{\phi_0(\mathbf{R})}{\psi_T(\mathbf{R})}|\psi_T\right\rangle}{\left\langle\phi_0|\frac{\phi_0(\mathbf{R})}{\psi_T(\mathbf{R})}|\psi_T\right\rangle} \quad . \tag{2.35}$$

It has been demonstrated within the DMC formalism [63], that factors $\phi_0(\mathbf{R})/\psi_T(\mathbf{R})$ are proportional to the asymptotic offspring of the corresponding walker configuration $\mathbf{R}$. Then, in virtue of (2.35), $\langle O(\mathbf{R})\rangle_p$ can be calculated associating a weight factor, $W(\mathbf{R})$, to each walker generated in the sampling of $\phi_0\psi_T$.

$$\langle O(\mathbf{R})\rangle_p = \frac{\sum_i O(\mathbf{R}_i) W(\mathbf{R}_i)}{\sum_i W(\mathbf{R}_i)} \tag{2.36}$$

The problem with the $W(\mathbf{R}_i)$ weights is that the number of future descendants of every ith walker must be known at any present time step. This issue becomes a tedious task when tagging algorithms are implemented with this purpose [64, 65]. However, a modified storage of $\{O(\mathbf{R}_i)\}$ along the whole sampling provides a more direct and simple solution to this technical problem [66]. The schedule of the corresponding algorithm is the following.

The set of walkers at a given time $\{\mathbf{R}_i\}$ and the values that the operator O takes on them $\{O_i\}$ evolve, after a time step to

$$\{\mathbf{R}_i\} \rightarrow \{\mathbf{R}'_i\} \, , \tag{2.37}$$

$$\{O_i\} \rightarrow \{O'_i\} \, . \tag{2.38}$$

In the same time interval, the number of walkers M changes to M'. In order to sample the pure estimator of O, we introduce an auxiliary variable $\{P_i\}$, associated to each walker, with an evolution law given by

$$\{P_i\} \rightarrow \{P'_i\} = \{P^t_i\} + \{O'_i\} \, , \tag{2.39}$$

where $\{P_i^t\}$ is the old set $\{P_i\}$ *transported* to the new one, in the sense that each element P_i is replicated as many times as the walker $\mathbf{R}_i$, without any other changes. The set $\{P_i\}$ is initialized to zero when the run starts.

With this procedure, after K addition steps (2.39) we end up with a set of M_f values $\{P_i\}$. A pure estimator of O is given by

$$\langle O(\mathbf{R})\rangle_p = \frac{1}{M_f \times K}\sum_{i=1}^{M_f}\{P_i\}\ . \tag{2.40}$$

The contribution to the $\{P_i\}$ entering in Eq.(2.40) coming from the set of walkers at a past time τ, $\{\mathbf{R}_i(\tau)\}$, can be determined by following the evolution of the series. The population as a whole has been evolving with branching from a starting time $\tau = 0$, giving as a result at time τ a population of walkers $\{\mathbf{R}_i(\tau)\}$ with a distribution probability given by the trial wave function times the exact one. Now, the values $\{O(\mathbf{R}_i)\}$ existing at time τ enter in the pure estimator with weight 1 (although they contribute together with other values corresponding to previous times which have already been weighted). From now on, if any of the descendants of $\mathbf{R}(\tau)$ disappears or replicates, the former contribution does so. As a result, $O(\mathbf{R}(\tau))$ appears in as many rows of $\{P\}$ as descendants of $\mathbf{R}(\tau)$ exist, and therefore its contribution to Eq.(2.40) is proportional to the weight $W(\mathbf{R}(\tau))$. Notice that no overlap exists between the time interval where the branching was used to obtain the trial function times the exact one and the interval where the branching has provided the additional weight to sample the exact ground state.

A final consideration concerning the implementation of the algorithm must be noted. In Eq.(2.39), the *transport* operation accounts for the replication of the $O(\mathbf{R})$ contribution. In order to ensure the asymptotic condition $W(\mathbf{R}) \to \phi_0(\mathbf{R})/\psi_T(\mathbf{R})$, the series are continued for a while only with the reweighting law $\{P_i\} \to \{P_i'\} = \{P_i^t\}$. Since a calculation is usually divided into several blocks, one can collect data during a block and allow for a further reweighting in the following one. In this second block, new information can be accumulated to be reweighted in the next block. This mechanism can be incorporated in the algorithm in a rather simple way. The final result is that, after a first initialization block, each new block gives a value for the pure expectation value of O.

Chapter 3
Two-dimensional p–$\mathrm{H_2}$ and o–$\mathrm{D_2}$ at $\mathrm{T} = 0$

3.1 Introduction

Unlike helium, bulk molecular hydrogen and deuterium solidify at any given pressure if a sufficiently low temperature is reached [67]. In spite of the light weight and bosonic character of these molecules, the strong–attractive interaction between them causes their crystallization, and consequently, frustrates any possibility of observing superfluidity (SF) or Bose–Einstein condensation (BEC).

Molecular hydrogen becomes a solid at a temperature significantly greater (T$\sim$14 K) than the critical temperature at which BEC and SF probably occur (T$\sim$4 K). Despite of this, many attempts have focused on supercooling bulk liquid p–$\mathbf{H_2}$ along the last decades [68, 69], but unfortunately, none has succeeded on a direct record of SF or BEC. A plausible way for inducing superfluidity in molecular hydrogen consists in lowering its melting temperature, that is, increasing the delocalization degree of molecules, by reducing its dimensionality and/or confining it to restricted geometries. Attending to this proposal, several studies of a $\mathbf{H_2}$ film adsorbed on different substrates have been carried out [70, 71, 72, 73]; as an example, two–dimensional hydrogen is observed to freeze at temperatures around 5 K when it is placed onto an exfoliated graphite plate [74]. Recently it has been shown that a purely one-dimensional array of $\mathbf{H_2}$ molecules remains in the liquid phase even at absolute zero [75]. On the other hand, recent experiments have observed that small para–hydrogen clusters immersed in $^{\mathbf{4}}\mathbf{He}$ droplets behave like a superfluid [76]. In fact, at the beginning of the 90's Sindzingre *et al.* [77] predicted

by means of the Path Integral Monte Carlo method such superfluid–like behaviour in small clusters of pure $\mathbf{H_2}$ (N<20) at temperatures below 2 K.

In this chapter, we present a comprehensive Quantum Monte Carlo study of two–dimensional p–$\mathbf{H_2}$ at zero temperature by means of the DMC technique. We have investigated both liquid and solid phases in order to discern which is the stable one once the dimensionality is reduced respect to the bulk case. To this end, we have calculated the equation of state (EOS) of solid and liquid $\mathbf{H_2}$. From this, one knows that a) at zero pressure the stable phase corresponds to the one with the lowest energy, and b) first order solid–liquid phase transitions are easily calculated on these curves (freezing and melting densities) with the double–tangent Maxwell's construction.

Our results regarding two–dimensional p–$\mathbf{H_2}$ at zero temperature evidence that the solid phase is the stable one along the whole range of permited densities ($\rho \geq \rho_S$, being ρ_S the spinodal density). No solid–to–liquid phase transition is allowed. In view of this, we have focused on a comprehensive study of the p–$\mathbf{H_2}$, and complementarily o–$\mathbf{D_2}$, solid films (sections 3.1 and 3.3, respectively). Referring to these studies, we have calculated physical magnitudes as the pressure, compressibility and speed of sound, all of them dependent on density. Some structural information have been obtained from the theoretical computation of the radial distribution function, g(r). Also, we have calculated the Lindemann's ratio, mean squared displacement and kurtosis using the pure estimator technique, in order to improve the accuracy of the DMC estimation.

In the special case of the p–$\mathbf{H_2}$ monolayer we have explored variationally the quality of two different trial wave functions (Nosanow–Jastrow functions using Gaussian and Padé forms), giving both similar results. In order to introduce the correct symmetry of the solid trial wave function, we have sampled variationally the permutational space of particles distributed in the crystalline sites. This sampling would be equivalent to the one performed with a permanent of one-body factors in the trial wave function. However, exchanges between molecules in the $\mathbf{H_2}$ film result very unlikely to occur, and consequently, the differences with the unsymmetrized wave function case are negligible.

In section 3.2, we present an alternative way to induce superfluidity in 2D molecular hydrogen, based on the idea suggested by Gordillo and Ceperley, consisting in the adsorbtion of $\mathbf{H_2}$ molecules on an alkali substrate [78].

Since the attraction between the alkali atoms and molecular hydrogen is softer than the $\mathbf{H_2}$–$\mathbf{H_2}$ one, and because a non–negligible effect of excluded surface, the freezing of the p–$\mathbf{H_2}$ film is frustrated. In particular, we report the study of two–dimensional $\mathbf{H_2}$ immersed on two different alkali substrates, namely Rb and Na, at zero temperature. Molecular hydrogen on both alkali surfaces presents superfluid–like behaviour to some extent.

3.2 Molecular para–hydrogen

The $\mathbf{H_2}$ molecule is composed by two $\mathbf{H}$ atoms joined by a covalent bond, which in the para–hydrogen state (angular momentum J=0) has spherical symmetry. Besides this, the energy scale involved in electronic excitations is orders of magnitude greater ($\sim 10^5$ K) than the atomic one ($\sim 10^1$ K). Therefore, the modelization of the $\mathbf{H_2}$–$\mathbf{H_2}$ interaction in the form of a radial pair–potential and point–like molecules, turns out to be justified. Indeed, such pair–potential is currently adopted in the form of the semiempirical Silvera-Goldmann one (3.1),

$$V(r) = \epsilon \left[\exp\left(\lambda - \xi r - \mu r^2\right) + f(r) \left(\sum_{i=6,8,10} \frac{C_i}{r^i} + \frac{C_9}{r^9} \right) \right] \tag{3.1}$$

$$f(r) = \begin{cases} \exp\left[-\left(\frac{1.28 r_m}{r} - 1 \right)^2 \right] & r < 1.28 r_m \\ 1 & r \geq r_m \end{cases}$$

$\epsilon = 315780.23$ K	$C_6 = -0.2665780864$ KÅ^6
$\lambda = 1.713$	$C_8 = -1.323274508$ KÅ^8
$\xi = 2.96139099$ Å^{-1}	$C_{10} = -8.289086326$ KÅ^{10}
$\mu = 0.03546070218$ Å^{-2}	$C_9 = 0.4656378451$ KÅ^9
$r_m = 3.41$ Å	

which actually results reliable in the low temperature and pressure regimes [79].

In the next subsection, we present a VMC study of 2D p–$\mathbf{H_2}$ in order to provide the most convenient trial wave function for the subsequent DMC

calculations (subsection 3.2.2), and also to get some initial physical insight on the system. The greater variational effort has been devoted to the achievement of an accurate description of the monolayer.

Regarding the solid structure of the film, the triangular lattice is the realistic one since molecules distributed according to it minimize their total energy. This statement has been checked through several VMC and DMC simulations of hydrogen molecules on a squared lattice at different densities.

3.2.1 VMC and trial wave functions

The liquid phase is described by a Jastrow wave function

$$\psi_J(\mathbf{r_1}, \mathbf{r_2}, ..., \mathbf{r_N}) = \prod_{i<j}^{N} \mathrm{f}_2(r_{ij}) \quad . \tag{3.2}$$

The solid phase requires of an additional one–body term (Nosanow–Jastrow model):

$$\psi_{JL}(\mathbf{r_1}, \mathbf{r_2}, ..., \mathbf{r_N}) = \psi_J \prod_{i}^{N} \mathrm{g}_1^{\mathrm{L}}(|\mathbf{r_i} - \mathbf{R_i}|) \tag{3.3}$$

with two different models for $\mathrm{g}_1^{\mathrm{L}}$:

$$\mathrm{g}_1^{\mathrm{G}}(r) = \exp\left(-\frac{a}{2}r^2\right) \tag{3.4}$$

$$\mathrm{g}_1^{\mathrm{P}}(r) = \exp\left(-\frac{ar^2}{1+cr}\right) \quad . \tag{3.5}$$

The index L in equation (3.3) can be either G or P, and the pair–correlation factor f_2 is taken in the McMillan's form, $\exp\left(-0.5\,(b/r)^5\right)$. The Gaussian and Padé functions, equations (3.4) and (3.5) respectively, are one–body factors which localize the particles around the crystalline sites (defined by the set of vectors $\{\mathbf{R_i}\}$). Both functions are quite similar, but they present two differences (see Figure 3.1): 1) the asymptotes in the Padé function tend to zero in a smoother way than in the Gaussian, and 2) the central region around the origin is somehow narrower in $\mathrm{g}_1^{\mathrm{P}}$ than in $\mathrm{g}_1^{\mathrm{G}}$. These differences might allow particles simulated with $\mathrm{g}_1^{\mathrm{P}}$ to move a bit far away around their equilibrium

b (Å)	a(Å^{-2})	$E/N(K)$
3.32	1.60	$-16.7(2)$
3.32	1.44	$-17.3(2)$
3.32	1.29	$-18.3(2)$
3.32	0.98	$-20.4(2)$
3.32	0.83	$-21.0(1)$
3.32	0.67	$-21.2(1)$
3.32	0.52	$-21.0(1)$
3.32	0.37	$-19.0(3)$
3.45	0.67	$-22.0(1)$

Table 3.1: Optimization process corresponding to the Gaussian function, $\mathrm{g}_1^{\mathrm{G}}$, in ψ_{JG} at the density ρ= 0.060 Å^{-2}. The parameter b corresponds to the McMillan factor.

a(Å^{-2})	c(Å^{-1})	$E/N(K)$
0.30	0.39	$-17.7(3)$
0.34	0.59	$-15.8(4)$
0.28	0.20	$-19.7(2)$
0.40	0.20	$-20.9(2)$
0.46	0.20	$-21.2(2)$
0.50	0.20	$-21.1(2)$
0.54	0.31	$-21.0(2)$
0.54	0.47	$-21.0(2)$
0.54	0.59	$-20.4(2)$
0.63	0.39	$-21.1(2)$

Table 3.2: Optimization process corresponding to the Padé function, $\mathrm{g}_1^{\mathrm{P}}$, in ψ_{JP} at the density ρ= 0.060 Å^{-2}. The value of parameter b in all the reported cases is 3.32Å.

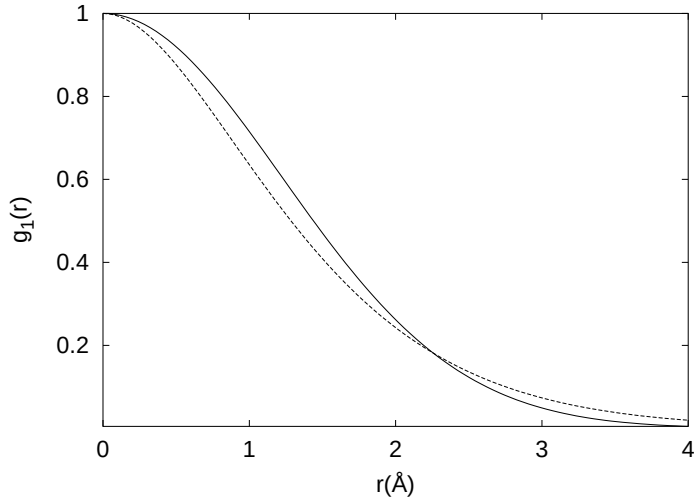

Figure 3.1: The solid and dashed lines correspond to the optimized Gaussian and Padé functions, respectively. The asymptotes in the last case tend to zero rather smooth, while its central region is somewhat narrower.

positions than in the $\mathrm{g}_1^{\mathrm{G}}$ case. In Tables 3.1 and 3.2, some selected variational energies calculated along the optimization procedures of the trial wave functions ψ_{JG} and ψ_{JP} are put forward. It is observed from them that the lowest energy obtained with the $\mathrm{g}_1^{\mathrm{P}}$ factors is appreciably higher than the one corresponding to the Gaussians ($\sim$1K of difference). Therefore, trial wave function ψ_{JG}, with best parameters $b = 3.45$ Å and $a = 0.67$ Å^{-2}, is the one chosen for the subsequent DMC study. Concerning the optimization of ψ_J in the liquid phase, the optimal parameter results $b = 3.70$ Å.

3.2.2 DMC results

Most of the simulations of this section have been performed with 90 particles within a rectangular plane with periodic boundary conditions applied on the two orthogonal directions. The critical number of walkers is 250 and the time step $5{\cdot}10^{-4}$ K^{-1}; these parameters have been adjusted to reduce a possible bias from them down to the typical statistical noise.

In Table 3.3 we present the ground–state energies per particle, E/N, cor-

responding to a p–$\mathbf{H_2}$ film at different densities; the corresponding mixed estimations of the potential, $\langle V \rangle$, and kinetic energies, $\langle T \rangle$, are also quoted therein. These results contain energy tail corrections, namely $\langle \Delta V \rangle^{tail}$ and $\langle \Delta T \rangle^{tail}$, in order to compensate the finite–size errors introduced by the finite size of the simulation box (plane) (Eq. 3.6 and 3.7). Kinetic and potential energy tails may be calculated analytically if one assumes that the pair–radial distribution function, g(r), equals one from a certain radial distance R_{max} (generally equal to one half the length of the simulation box) to infinite (Eq. 3.8 and 3.9).

$$\langle T \rangle = \langle T \rangle^{sim} + \langle \Delta T \rangle^{tail} \tag{3.6}$$

$$\langle V \rangle = \langle V \rangle^{sim} + \langle \Delta V \rangle^{tail} \tag{3.7}$$

$$\frac{\langle \Delta T \rangle^{tail}}{N} = -2\pi D\rho \int_{R_{max}}^{\infty} \nabla^2 \ln \mathrm{f}_2(r) r \, dr \tag{3.8}$$

$$\frac{\langle \Delta V \rangle^{tail}}{N} = \pi\rho \int_{R_{max}}^{\infty} V(r) r \, dr \tag{3.9}$$

In equations (3.6) and (3.7) the subscript ^{sim} means obtained directly from the simulation, while the factors N, ρ and D (=$\hbar^2/2m$) are the number of particles, density and diffusion constant, respectively.

The equations of state in liquid and solid 2D p-$\mathbf{H_2}$ at zero temperature are depicted in Figure 3.2; the curves in the figure correspond to the polynomial fit [80]

$$\frac{E}{N} = e(\rho) = e_0 + B\left(\frac{\rho - \rho_0}{\rho_0}\right)^2 + C\left(\frac{\rho - \rho_0}{\rho_0}\right)^3 . \tag{3.10}$$

The pressure, compressibility and speed of sound are then easily deduced from (3.10) according to the expressions,

$$P(\rho) = \rho^2 \frac{\partial e(\rho)}{\partial \rho} \tag{3.11}$$

$$\kappa(\rho) = \frac{1}{\rho}\left(\frac{\partial \rho}{\partial P}\right)_T \tag{3.12}$$

$$c(\rho) = \left(\frac{1}{m\kappa\rho}\right)^{\frac{1}{2}} . \tag{3.13}$$

ρ(Å^{-2})	E/N (K)	$\langle V\rangle/N$ (K)	$\langle T\rangle/N$ (K)
0.050	$-17.89(2)$	$-31.91(1)$	$14.02(1)$
0.056	$-20.76(1)$	$-38.58(1)$	$17.82(2)$
0.060	$-22.21(1)$	$-42.96(1)$	$20.75(1)$
0.067	$-23.41(1)$	$-50.06(1)$	$26.65(1)$
0.073	$-22.37(1)$	$-54.65(1)$	$32.28(1)$
0.080	$-17.78(2)$	$-57.29(2)$	$39.51(1)$
0.086	$-9.55(2)$	$-56.41(2)$	$46.85(1)$
0.091	$-1.22(2)$	$-53.56(2)$	$52.33(1)$

Table 3.3: Ground–state energy, E/N, potential energy, $\langle V\rangle/N$, and kinetic energy, $\langle T\rangle/N$, per particle in solid 2D p–$\mathbf{H_2}$. The potential and kinetic energies are mixed estimations. The parameters of the simulations are, $\Delta\tau = 5\cdot 10^{-4}\mathrm{K}^{-1}$, $n_w = 250$ (critical walker's population) and $N = 90$.

The polynomial fit to the solid film data yields $e_0 = -23.453(3)$K, $\rho_0 = 0.0673(1)$Å^{-2}, $B = 121(2)$K and $C = 152(8)$K, where e_0 and ρ_0 are the equilibrium energy per particle and density, respectively. The compressibility and speed of sound at the equilibrium density are $\kappa(\rho_0) = 0.0615(8)$Å^2/K and $c(\rho_0) = 998.6(1)$m/s. Figures quoted in parenthesis are the statistical errors.

Another interesting characteristic which is deduced from the EOS is the spinodal density, ρ_S. At this density the system becomes mechanically instable, that is, its compressibility growns to infinite (speed of sound becomes zero), and consequently, an homogeneous phase is no longer possible. We have calculated such limit density in the p–$\mathbf{H_2}$ monolayer using the law (3.10), and we have obtained ρ_S= 0.0548(1) Å^{-2}.

In Figure 3.2 it is observed that the solid phase is the stable one in the whole depicted range, owing that its energy is systematically lower than the one corresponding to the liquid. In principle, in the regime of negative pressures, it could be suggested a liquid–solid phase transition within the interval $[\rho_S, \rho_0]$ and a very dilute 2D liquid. However, we have simulated the liquid film at densities up to the 0.039 Å^{-2} (presumably down to the spinodal density corresponding to this hypothetical phase) and no first order transition is observed. Therefore, it may be stated with confidence that a liquid phase of

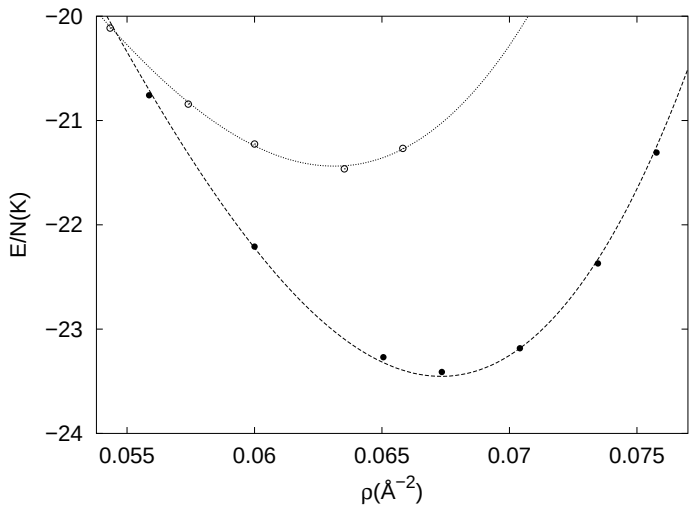

Figure 3.2: Equation of state of liquid (dotted line) and solid (dashed line) 2D p-$\mathbf{H_2}$ at zero temperature. The curves are the polynomial curves (3.10) which best fits to our results (empty and filled circles); the statistical errors bars are smaller than the symbols.

2D p–$\mathbf{H_2}$ at zero temperature can not be induced as a result of reducing the dimensionality from 3D to 2D.

Two theoretical works based on the PIMC approach [78, 81], may be commented in relation to our DMC results. In Ref [78], Gordillo *et al.* estimate the equilibrium density of solid 2D p–$\mathbf{H_2}$ at T=1K in 0.064Å^{-2}; the authors also report the figure of the equation of state, where the minimum energy is located around -22.0K. On the other hand, a more systematic study of the same solid film is presented by Boninsegni in Ref. [81]. There, the total energy per particle and chemical potential at different densities in the temperature range 1-8 K are quoted. An extrapolation of these low temperature results to absolute zero is performed, yielding $\rho_0^{PIMC} = 0.0668(5)$Å^{-2}, $e_0^{PIMC} = -23.25(5)$K and $\rho_S^{PIMC} = 0.0585(10)$Å^{-2}. It is observed that the agreement between these zero–extrapolated PIMC values and our DMC results is fairly good, specially in the case of ρ_0 where both results are coincident.

To get some insight on the structural properties of the molecular hydro-

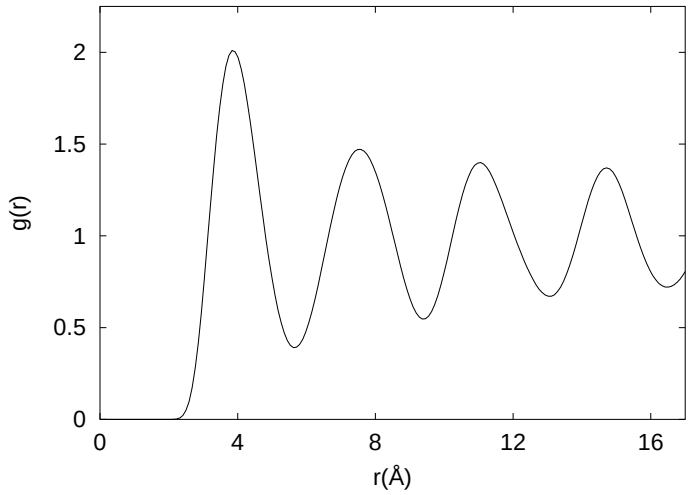

Figure 3.3: The ground–state radial pair–distribution function of two-dimensional molecular hydrogen at the equilibrium density $\rho_0 = 0.067\text{Å}^{-2}$.

gen film, we have calculated the radial pair–distribution function, g(r). The g(r) function, defined in equation (3.14), is proportional to the probability of finding two particles at an interparticle distance r.

$$g(r) = \frac{N-1}{\rho} \frac{\int |\Psi(\mathbf{r_1}, \mathbf{r_1}+\mathbf{r}, ..., \mathbf{r_N})|^2 d\mathbf{r_1} d\mathbf{r_3} ... d\mathbf{r_N}}{\int |\Psi(\mathbf{r_1}, \mathbf{r_2}, ..., \mathbf{r_N})|^2 d\mathbf{r_1} ... d\mathbf{r_N}} \tag{3.14}$$

The result obtained at equation (3.14) is shown in Fig. 3.3. In this figure, a pattern of periodic oscillations is observed; this pattern describes the characteristic spatial order of the molecules in the solid, and the position of the first peak coincides with the parameter of the lattice.

A common estimator in the study of quantum solids is the Lindemann's ratio, which is defined as

$$\gamma = \frac{1}{a} \sqrt{\langle \frac{1}{N} \sum_{i=1}^{N} (\mathbf{r_i} - \mathbf{R_i})^2 \rangle} = \frac{\langle \mathbf{u^2} \rangle^{\frac{1}{2}}}{a} \tag{3.15}$$

a being the distance between nearest neighbours in the perfect crystalline lattice. This quantity yields the mean squared displacement of any particle

around its lattice site scaled by the parameter a : the greater is γ the more relevant quantum effects are. Apart from providing some microscopic information, the Lindemann's ratio is also related to the Debye–Waller factor, M_Q, which yields the attenuation of the emergent radiation in coherent scattering experiments [30],

$$I\left(Q,T\right) \propto exp\left(-2M_Q\right) \ . \tag{3.16}$$

In equation (3.16), $I\left(Q,T\right)$ represents the intensity of the outgoing radiation scattered by the target, while the modulus vector $Q \equiv \hbar|\mathbf{k_f} - \mathbf{k_i}|$ corresponds to the transfer vector of the incident wave. The Debye–Waller factor admits the cumulant expansion [82]

$$2M_Q = \langle u_Q^2\rangle Q^2 - \frac{1}{12}\left(\langle u_Q^4\rangle - 3\langle u_Q^2\rangle^2\right) Q^4 + O(Q^6) \ , \tag{3.17}$$

where $\langle u_Q^2\rangle$ is the mean squared value of the projections $\{\widehat{\mathbf{Q}}\cdot(\mathbf{r_i} - \mathbf{R_i})\}$. When the spatial distribution of particles around their equilibrium positions is well described by a Gaussian pattern, the Debye–Waller factor reduces to $\langle u_Q^2\rangle Q^2$ because the magnitude ζ_Q, known as kurtosis and defined below, vanishes.

$$\zeta_Q = \frac{\langle u_Q^4\rangle}{\langle u_Q^2\rangle^2} - 3 \tag{3.18}$$

Results concerning the Lindemann's ratio and related microscopic properties in two–dimensional p–$\mathbf{H_2}$ are reported in Table 3.4. We have investigated the density distribution around the equilibrium positions in the solid film by 1) calculating $\langle u_Q^2\rangle$ in two orthogonal directions (results do not depend on the direction), and 2) quoting the kurtosis in several directions (it always vanishes). In view of our results, it can be asserted that the density distribution of the hydrogen molecules around the lattice sites is isotropic and Gaussian.

In a recent PIMC work [83], Draeger and Ceperley used this strategy to detect possible anisotropies of the Debye–Waller factor in bulk solid $^4\mathbf{He}$ at temperatures near 20 K; in fact, they computed ζ for one characteristic direction of the crystal and subsequently found a non–negligible k^4 contribution to M_Q. According to this result, the authors concluded that the density distribution around the lattice sites in solid helium is not Gaussian.

It is illustrative to note the large Lindemann's ratio in two–dimensional molecular hydrogen at equilibrium, γ_0 ∼0.18, which puts in evidence the un-

$\rho(\text{Å}^{-2})$	γ	$\zeta_{(10)}$	$\zeta_{(01)}$	$\langle \mathbf{u^2} \rangle (\text{Å}^2)$
0.0582	0.212(1)	0.00(2)	0.00(2)	0.19(1)
0.0600	0.197(1)	0.02(2)	0.00(2)	0.15(1)
0.0650	0.183(1)	0.02(2)	0.02(3)	0.12(1)
0.0673	0.178(1)	−0.01(1)	−0.02(2)	0.11(1)
0.0704	0.170(1)	−0.02(1)	0.00(2)	0.09(1)
0.0758	0.158(1)	0.00(2)	0.01(1)	0.07(1)
0.0834	0.146(1)	0.01(2)	0.01(1)	0.06(1)

Table 3.4: Lindemann's ratio, γ, kurtosis, ζ, and mean squared displacement, $\langle \mathbf{u^2} \rangle$, of 2D $\mathbf{H_2}$ at different densities close to the equilibrium one.

avoidable quantum character of such system; as a matter of comparison, the one corresponding to 2D solid $^4\mathbf{He}$ near melting is $\gamma^{\text{He}} \sim$0.24 [84].

3.2.3 Symmetrized Trial wave functions

In this subsection, we summarize the variational results obtained with two different trial wave functions correctly symmetrized.

The first proposal consists in a productory of sums in the form

$$\psi_{JL}^{S}\left(\mathbf{r_1}, \mathbf{r_2}, ..., \mathbf{r_N}\right) = \psi_J \prod_{i=1}^{N} \left(\sum_{j=1}^{N} \exp\left(-\frac{a}{2} \left(\mathbf{r_i} - \mathbf{R_j} \right)^2 \right) \right). \tag{3.19}$$

This trial wave function provides compact and manageable expressions of the drift force and kinetic energy. However, the results obtained are worse than the ones obtained within the Nosanow–Jastrow model (see Table 3.5). Additionally, some other variational calculations using the same functional form (3.19) but replacing the Gaussians by Padé functions were carried out (see Table 3.6). The conclusions in both cases are identical: the energies obtained are always larger than the best one corresponding to the Nosanow–Jastrow model (-22.0(1)K).

The physical inconsistency arising from trial wave function (3.19) comes from the excessive diffusion of the particles within the solid. Such unphysical diffusion occurs because the sum of two neighbouring Gaussians is quite

b_J (Å)	a (Å^{-2})	$E/N(K)$
3.32	0.34	$-12.9(8)$
3.32	0.67	$-17.4(4)$
3.58	0.34	$-17.3(4)$
3.58	0.38	$-17.9(2)$
3.70	0.34	$-17.7(4)$
3.70	0.43	$-17.3(3)$
3.70	0.49	$-17.4(3)$
1.50	0.34	$-16.3(3)$

Table 3.5: Variational results obtained with the symmetrized trial wave function (3.19), where the g_1 factors are adopted in the form of Gaussians.

large within the intermediate overlapping zone, and also, because multiple occupation of the same lattice site by different particles is allowed. In spite of stressing the Gaussian factors in order to avoid this unrealistic diffusion within the solid, the rapid increase of the kinetic energy makes the total energy worse. Variational energies obtained on this ansatz result very similar to the ones calculated in the liquid phase with the Jastrow factor (-17.4(2)K).

As a second alternative, we have introduced a permanent of monoparticular functions in the one–body part of the solid trial wave function. Additional to a description of the lattice structure, such permanent contains the $N!$ possible permutations of the N indistinguishable particles among the different lattice sites.

$$\psi^S_{JL}(\mathbf{r_1}, \mathbf{r_2}, ..., \mathbf{r_N}) = \psi_J \sum_P \prod_{i=1}^{N} \mathrm{g}_1 \left(\mathbf{r_i} - \mathbf{R_{Pi}}\right) \tag{3.20}$$

Due to the algebraic difficulties arising in the implementation of permanents (contrarily to determinants), our random walk is divided into two different samplings: one performed on the configurational space of the particles and the other on the permutational one [52]. Consistently, the Metropolis acceptance of any proposed movement of the ith particle, $\mathbf{r_i} \rightarrow \mathbf{r'_i}$, must be

$$q = min\left(1, \frac{\psi_J(\mathbf{r'})^2 \mathrm{g}_1(\mathbf{r'_i} - \mathbf{R_i}) \mathrm{g}_1(\mathbf{r'_i} - \mathbf{R_{Pi}})}{\psi_J(\mathbf{r})^2 \mathrm{g}_1(\mathbf{r_i} - \mathbf{R_i}) \mathrm{g}_1(\mathbf{r_i} - \mathbf{R_{Pi}})}\right) \tag{3.21}$$

b_J (Å)	a (Å^{-2}), b(Å^{-1})	$E/N(K)$
3.32	0.63, 0.39	$-12.4(4)$
3.58	0.63, 0.39	$-17.4(3)$
3.70	0.63, 0.39	$-17.7(3)$
3.83	0.63, 0.39	$-16.8(3)$
3.70	0.69, 0.39	$-17.9(4)$
3.70	0.69, 0.47	$-17.7(2)$
3.70	0.73, 0.47	$-17.6(3)$
3.70	0.73, 0.59	$-17.7(3)$

Table 3.6: Variational results obtained with the symmetrized trial wave function (3.19), but with Padé functions instead of the Gaussians.

where the subindex $\mathbf{Pi}$ can take any of the N lattice possible values.

On the other hand, the Metropolis acceptance of any proposed site permutation between the ith and the jth particles, $\mathbf{R_{Pi}} \leftrightarrow \mathbf{R_{Pj}}$, must be

$$q_p = min\left(1, \frac{\mathrm{g}_1(\mathbf{r_j} - \mathbf{R_{Pi}})\mathrm{g}_1(\mathbf{r_i} - \mathbf{R_{Pj}})}{\mathrm{g}_1(\mathbf{r_j} - \mathbf{R_{Pj}})\mathrm{g}_1(\mathbf{r_i} - \mathbf{R_{Pi}})}\right) . \tag{3.22}$$

The results obtained within this framework are presented in Tables 3.7 and 3.8, which correspond to Gaussian and Padé functions replacing the g_1 factors in (3.20), respectively. When comparing them with best results in Tables 3.1 and 3.2 (-22.0(1) and -21.2(2)K respectively), one realizes that no significant differences between the symmetrized and unsymmetrized trial wave function cases exist. This occurs because, as is reflected in the columns of the acceptance rate, site permutations between different molecules are unlikely to occur. Moreover, whether the width of the g_1 factors is enlarged in order to increase such acceptance rate (a is decreased), the total energy of the system inevitably increases.

In conclusion, the correct symmetrization of the trial wave function describing the ground state of the 2D p-$\mathbf{H_2}$ film has a negligible effect in the evaluation of the total energy, owing that site–exchanges between different molecules are very unlikely to occur. Therefore, the use of unsymmetrized

a(Å^{-2})	$E/N(K)$	acceptance(%)
0.918	$-20.8(1)$	10^{-4}
0.842	$-21.6(2)$	$5 \cdot 10^{-4}$
0.765	$-21.2(1)$	10^{-3}
0.673	$-21.0(2)$	$5 \cdot 10^{-3}$
0.459	$-20.2(2)$	0.15
0.383	$-19.7(3)$	0.5

Table 3.7: Variational energies obtained with Gaussian factors in the general symmetrized trial wave function (3.20). The acceptance column corresponds to the acceptance rate in the sampling of the permutational space.

a(Å^{-2}),	b(Å^{-1})	$E/N(K)$	acceptance(%)
0.627,	0.391	$-21.0(1)$	0.10
0.627,	0.587	$-21.0(2)$	0.75
0.689,	0.391	$-20.8(1)$	0.05
0.689,	0.587	$-20.8(2)$	0.5
0.536,	0.587	$-18.7(5)$	2.5
0.536,	0.391	$-20.8(3)$	0.35

Table 3.8: Variational energies obtained with Padé factors in the general symmetrized trial wave function (3.20). The acceptance column corresponds to the acceptance rate in the sampling of the permutational space.

trial wave functions when computing exact ground–state energies within the DMC formalism turns out to be justified in the present case.

3.3 Two-dimensional molecular hydrogen on alkali substrates

We have carried out several DMC calculations of 2D p-$\mathbf{H_2}$ with fixed alkali impurities distributed according to a realistic solid lattice [85]. The simulations have been carried out with Rb and Na, since they present in nature the proper lattices which frustrate the $\mathbf{H_2}$ crystallization (lattice order ~ 10 Å) [86, 87, 88]. The results obtained show in the case of Rb a highly structured liquid phase with a superfluid fraction practically suppressed, while in the Na case the corresponding superfluid fraction results appreciably large due to a larger diffusion of the molecules. Indeed, the cause of this difference relies on the fact that the Na-$\mathbf{H_2}$ interaction is less repulsive than the Rb-$\mathbf{H_2}$ one, and therefore, a higher concentration of hydrogen molecules is allowed in the *holes* of the surface (free space between the atoms of the substrate).

Furthermore, we have calculated the EOS, radial distribution function and condensate fraction of the p–$\mathbf{H_2}$ molecules in both cases. We have found that the condensate fraction, n_0, is practically null in both systems.

Actually, there are few potentials in the literature which correctly describe the alkali-$\mathbf{H_2}$ interaction [90]; we believe that for a final and more conclusive answer on this matter, quite more accurate and versatile modelizations of such interatomic interactions would be required.

3.3.1 2D p–$\mathbf{H_2}$ on Rb

The trial wave function for the present problem contains correlations between N $\mathbf{H_2}$ molecules ($\mathrm{f}_2(r_{ij})$) and between $\mathbf{H_2}$ and the n Rb atoms ($\mathrm{F}_2(R_{ij})$),

$$\psi\left(\mathbf{r}_1, \mathbf{r}_2, \ldots, \mathbf{r}_N\right) = \prod_{i<j}^{N} \mathrm{f}_2(r_{ij}) \prod_{i,k}^{N,n} \mathrm{F}_2(R_{ik}) \; . \tag{3.23}$$

Both two–body correlation factors have been chosen of McMillan form $exp(-0.5(b/r)^5)$, the parameters being selected through a previous variational Monte Carlo (VMC) calculation. The optimal values are b= 3.7 and 6.4 Å for the pairs $\mathbf{H_2}$-$\mathbf{H_2}$ and $\mathbf{H_2}$-Rb, respectively.

ρ(Å^{-2})	E/N(K)	$\langle V\rangle/N$(K)	$\langle T\rangle/N$(K)
0.011	$-43.40(6)$	$-58.14(8)$	$14.74(3)$
0.015	$-43.28(3)$	$-57.78(3)$	$14.50(3)$
0.018	$-44.06(1)$	$-59.83(1)$	$15.78(1)$
0.023	$-44.68(3)$	$-61.46(9)$	$16.77(8)$
0.026	$-44.48(2)$	$-64.26(2)$	$19.78(1)$

Table 3.9: Total and partial energies per particle of liquid $\mathbf{H_2}$ immersed in the Rb lattice

The internal structure of the para-$\mathbf{H_2}$ molecules is neglected and their interactions are modeled by the standard Silvera–Goldman potential [79]. The interaction between $\mathbf{H_2}$ and alkali atoms is much less known. We have taken for it a Lennard–Jones potential with the parameters reported in Ref. [90]. In particular, for Rb-$\mathbf{H_2}$ these are σ= 4.54 Å and ϵ= 28.0 K, which are appreciably much larger than the ones used in Ref.[78] for the interaction K-$\mathbf{H_2}$.

Both the Rb atoms and the $\mathbf{H_2}$ molecules are arranged in a strictly two–dimensional geometry. The Rb atoms are considered as fixed impurities distributed according to a triangular solid phase with lattice parameter 10 Å. As commented previously, this solid Rb film is realistic since it has been observed experimentally adsorbed in a Ag plate [86]. The number of alkali impurities in the simulation box is kept fixed to 30 and the number of $\mathbf{H_2}$ molecules is progressively increased to obtain the equation of state.

It is worth noticing that a solid $\mathbf{H_2}$ film commensurate with this substrate is not possible if the size of the core of the alkali–hydrogen interaction is taken into account. Commensurability between two crystalline lattices is fulfilled when both respective Bravais lattices are of the same type, and each point of the reciprocal lattice of one of them is included in the reciprocal lattice of the other (p.e. the triangular and $\sqrt{3}R30^\circ$ triangular lattices) [89]. In the present case, commensurability would force the equilibrium distance between any Rb atom and its nearest hydrogen molecule to be, at least, $d \sim 0.29a$ (equal to the distance between the circumcenter and any of the vertexes in an equilater triangle of side a), a being the lattice parameter of the commensurate hydrogen solid film. Therefore, making d equal to the core of the $\mathbf{H_2}$-Rb interaction (σ),

parameter a is deduced to be $\sim$15Å. Certainly, this result has nonsense since the hydrogen molecules would be separated by an excessive distance which is even greater than the Rb-Rb one.

The energy of 2D p-$\mathbf{H_2}$ with the fixed array of alkali impurities is calculated using the DMC method for different numbers of $\mathbf{H_2}$ molecules in a fixed simulation box. The results obtained for the total and partial energies when the substrate is Rb are reported in Table 3.9. The equilibrium point is obtained through a polynomial fit to the data (3.10); it is located at a density 0.023 Å^{-2} with a ground–state energy -44.68 K. This point is rather far from that corresponding to a pure solid $\mathbf{H_2}$ film (see Table 3.3): the density is much larger, 0.067 Å^{-2}, and the energy is smaller, -23.41 K. The sizeable increase in the total energy is due to the potential energy between the substrate and $\mathbf{H_2}$.

If the Rb substrate is replaced by a K one, with the same lattice constant, the equilibrium point is nearly unchanged since the Lennard–Jones parameters (σ,ϵ) for the pair K-$\mathbf{H_2}$ do not differ significantly of the ones for Rb-$\mathbf{H_2}$ [90]. The results change dramatically if one considers the K-$\mathbf{H_2}$ parameters estimated in Ref. [78]. (σ= 3.75 Å,ϵ= 9.54 K). Our calculation for this latter case gives an energy -20.17 K corresponding to an equilibrium density of 0.038 Å^{-2}. This result for the equilibrium density is in agreement with the one reported in Ref. [78] but our energy is larger due to the fact that we have reduced the size effects in the simulation.

The relatively large core of the Rb-$\mathbf{H_2}$ interaction does not leave much space for the diffusion of the $\mathbf{H_2}$ molecules. This feature is reflected in the $\mathbf{H_2}$-$\mathbf{H_2}$ and Rb-$\mathbf{H_2}$ pair–radial distribution functions shown in Fig.3.4. The $g_{H_2-H_2}(r)$ shows a periodic–like structure which slowly vanishes at long distances; the position of the peaks correspond to an hexagonal pattern corresponding to the *holes* in the middle of the triangles of the Rb lattice. This most probable position for the $\mathbf{H_2}$ molecules appears also clearly as the main peak of the mixed distribution $g_{Rb-H_2}(r)$.

A fundamental magnitude which characterizes the expected superfluid character of liquid $\mathbf{H_2}$ is the non–zero condensate fraction n_0. The value of n_0 is obtained as $n_0 = \lim_{r\to\infty} \varrho(r)$, with $\varrho(r)$ the one–body density matrix

$$\varrho(r) = \rho \, \frac{\int \Psi\left(\mathbf{r_1}+\mathbf{r}, ..., \mathbf{r_N}\right) \Psi^*\left(\mathbf{r_1}, ..., \mathbf{r_N}\right) d\mathbf{r_1}...d\mathbf{r_N}}{\int \left|\Psi\left(\mathbf{r_1}, ..., \mathbf{r_N}\right)\right|^2 d\mathbf{r_1}...d\mathbf{r_N}} \; . \tag{3.24}$$

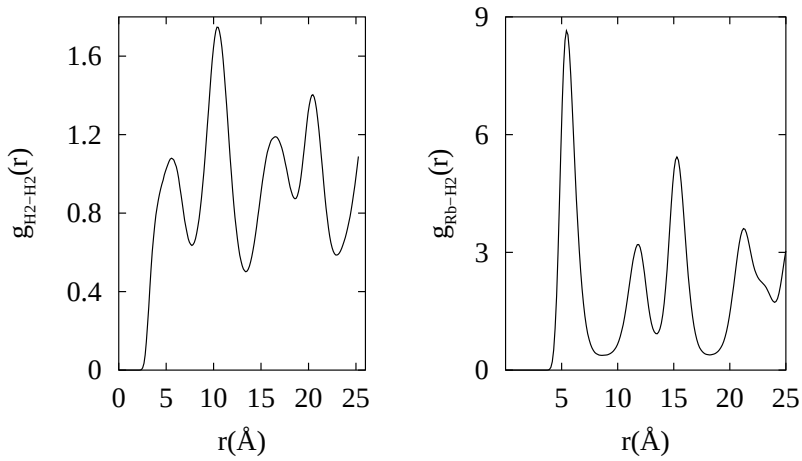

Figure 3.4: Left: $\mathbf{H_2}$–$\mathbf{H_2}$ radial distribution function. Right: Rb–$\mathbf{H_2}$ radial distribution function. Both calculated at a density σ= 0.023 Å^{-2}.

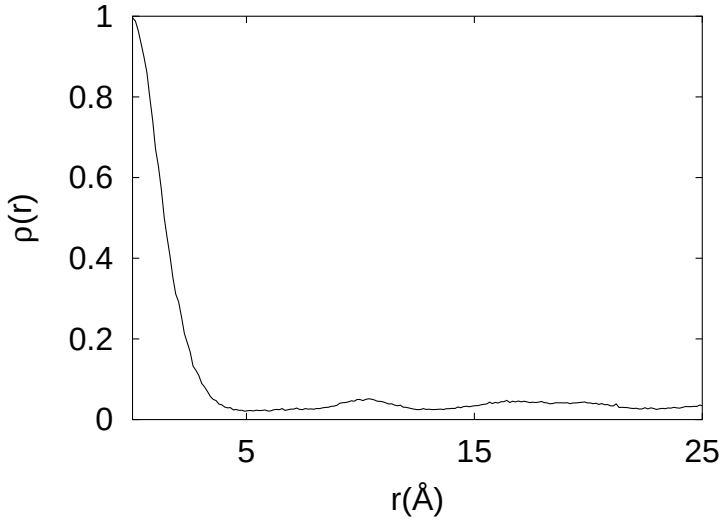

Figure 3.5: One–body density matrix of 2D $\mathbf{H_2}$ in the Rb substrate.

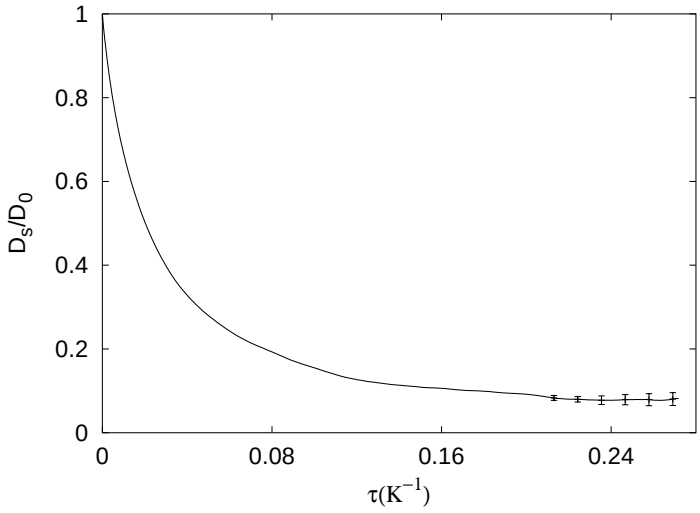

Figure 3.6: Diffusion coefficient of the center of mass in imaginary time. The asymptotic value is the DMC estimation of the $\mathbf{H_2}$ superfluid density in the Rb substrate.

The result for $\varrho(r)$ at the equilibrium density is shown in Fig.3.5. As one can see, $\varrho(r)$ becomes constant at large distances in spite of some oscillations induced by the substrate. The condensate fraction extracted from $\varrho(r)$ is very small, about 0.03; this value is approximately seven times smaller than n_0 in 2D ^{4}**He** at zero temperature.

In order to complete the description of the system, we have calculated its superfluid fraction ρ_s/ρ. This quantity is accessible in a DMC calculation by extending to zero temperature the winding–number technique employed in PIMC calculations, as discussed for bosons in a lattice in Ref. [91]. In 2D, the superfluid fraction is obtained as the ratio of two diffusion constants $\rho_s/\rho = D_s/D_0$ when $\tau \to \infty$, with $D_0 = \hbar^2/(2m)$ and

$$D_s = \lim_{\tau\to\infty} \frac{N}{4\tau} \frac{\int d\mathbf{R} f(\mathbf{R},\tau) \left[\mathbf{R}_{\rm CM}(\tau) - \mathbf{R}_{\rm CM}(0)\right]^2}{\int d\mathbf{R} f(\mathbf{R},\tau)} \tag{3.25}$$

being the diffusion constant of the *center of mass* of the system, i.e., $\mathbf{R}_{\rm CM} = (1/N)\sum_{i=1}^{N} \mathbf{r}_i$. In Fig.3.6, we show the result for D_s/D_0 at the equilibrium

ρ (Å^{-2})	$E/N(K)$	$\langle V\rangle/N$	$\langle T\rangle/N$
0.029	$-45.04(4)$	$-63.65(7)$	$18.61(7)$
0.031	$-45.66(3)$	$-65.52(5)$	$19.86(5)$
0.033	$-46.24(2)$	$-67.02(5)$	$20.78(5)$
0.036	$-46.93(2)$	$-69.36(7)$	$22.43(7)$
0.038	$-47.13(2)$	$-71.57(7)$	$24.44(7)$
0.040	$-46.86(3)$	$-72.95(5)$	$26.09(5)$

Table 3.10: Total, potential and kinetic energies per particle near the equilibrium density corresponding to the $\mathbf{H_2}$ molecules immersed in the Na substrate.

density. From the asymptote, one extracts the superfluid fraction; the result for the present system is 0.08, again a very small figure. In Ref. [78], with K instead of Rb and different Lennard–Jones parameters, a much larger value of the superfluid density was reported (0.25). This sizeable decrease is mainly due to the more attractive $\mathbf{H_2}$–alkali potential used in this work that we consider as more realistic. Also it is noted that the triangular lattice of K atoms with parameter 10Å is not a realistic one since it has never been experimentally observed.

3.3.2 2D p–$\mathbf{H_2}$ on Na

The trial wave function adopted for the present system also corresponds to equation (3.23). The optimal variational parameters are $b = 3.7$ and 5.62 Å for the $\mathbf{H_2}$–$\mathbf{H_2}$ and $\mathbf{H_2}$–Na pairs, respectively. The $\mathbf{H_2}$-Na interaction is modeled with the L–J potential, $\sigma = 4.14$Å and $\epsilon = 30$ K [90].

The substrate is considered a strict two-dimensional triangular lattice of parameter 10Å where the alkali atoms are assumed static and point–like. We are confident about the reliability of this sodium film [88, 87] which is found to be adsorbed on Ag(111) at very low temperatures (T<35 K).

In Table 3.10 we present the total, potential and kinetic energies per particle corresponding to the adsorbed p-$\mathbf{H_2}$ molecules at different densities, calculated by means of the DMC technique; the fit to the polynomial curve (3.10) gives the values B= 86.16 K, C= 221.69 K, ρ_0= 0.038 Å^{-2} and e_0= -47.13 K ,

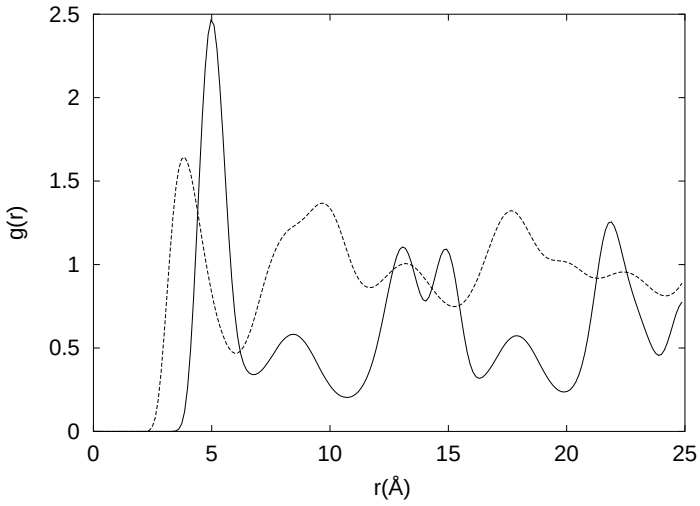

Figure 3.7: Radial pair–distribution functions corresponding to the $\mathbf{H_2}$-$\mathbf{H_2}$ (dashed line) and $\mathbf{H_2}$-Na (solid line) pairs. Both are calculated at the equilibrium density $\rho_0 = 0.038$ Å^{-2}.

where ρ_0 and e_0 are the equilibrium density and energy, respectively.

It is observed that the equilibrium density of molecular hydrogen immersed on Na is notably higher than the one on Rb (0.023 Å^{-2}). The ratio between the number of molecules and the number of alkali atoms at equilibrium is 10/3 in Na and 2/1 in Rb. The responsible of such increase in ρ_0 is the decrease of the repulsive core corresponding to the crossed interaction ($\sigma_{H_2-Na} < \sigma_{H_2-Rb}$), which makes larger the free surface available by the $\mathbf{H_2}$ molecules.

Making use of the formulas and methodology described in the previous subsection, we have calculated the condensate and superfluid fractions in the Na–$\mathbf{H_2}$ system. Our results evidence a very small condensate fraction ($n_0 \sim$ 0.02) and a considerably large superfluid fraction, ρ_s/ρ_0= 0.33 (2), at equilibrium. The increase of the superfluid fraction respect to the Rb substrate is related to the increase of the p-$\mathbf{H_2}$ concentration at the equilibrium. Predictably, if homogeneous 2D p-$\mathbf{H_2}$ was liquid at zero temperature its superfluid fraction would be equal to one and the equilibrium density would be 0.063 Å^{-2}

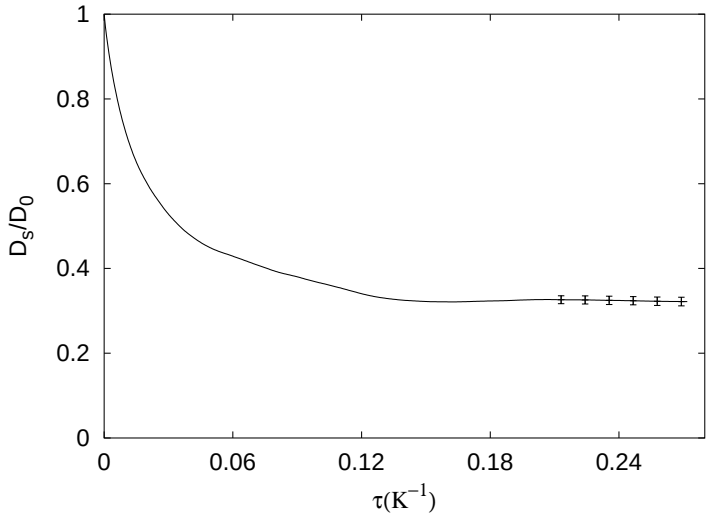

Figure 3.8: Diffusion coefficient of the center of mass in imaginary time. The asymptotic value is the DMC estimation of the $\mathbf{H_2}$ superfluid density immersed in the Na substrate, ρ_s/ρ_0= 0.33(2).

(as we have deduced previously in the pure liquid case, see Figure 3.2).

Attending to the results obtained on the Rb and Na substrates, it can be stated that small variations of the parameters entering the $\mathbf{H_2}$–alkali potential forms may provide noticeable differences on the computed properties of p–$\mathbf{H_2}$. This fact puts in evidence the need of more accurate and versatile potentials in order to get more reliable results.

It is worth noticing that the equilibrium density obtained for the Na case coincides with the result obtained by Gordillo and Ceperley [78] for the K substrate, and that both superfluid fractions are very similar ($\sim$ 0.30). Therefore,it is evidenced a strong dependence of this magnitude on the coverage, since the parameters entering both $\mathbf{H_2}$–alkali potentials are different.

In Figure 3.7 we depict the radial pair–distribution function corresponding to the $\mathbf{H_2}$-$\mathbf{H_2}$ and $\mathbf{H_2}$-Na pairs. Despite solid order is exhibited on them, the peaks are less sharp than the corresponding to the $\mathbf{H_2}$-Rb case (see Figure 3.4). This fact is in accordance with the larger diffusion of the molecules, feature that is behind the notable increase of the superfluid fraction.

3.3.3 Plausibility of the 2D model

Many experimental and theoretical studies of liquid $\mathbf{H_2}$ adsorbed onto different alkali substrates have been reported recently [92, 93, 94, 95]. Once we place a liquid above a certain surface at a pressure equal to the saturated vapor pressure, two possible behaviours are expected: spreading across the surface (wetting) or beading up to form a droplet (non–wetting). Experimental evidence shows that liquid $\mathbf{H_2}$ wets the surface of bulk alkalis at temperatures higher and around 20 K (for instance, $T_w \sim 18$K in Rb and $T_w \sim 21$ K in Cs) [92, 93]. On the other hand, few full–quantum finite temperature simulations are found to date to derive conclusive results concerning this wetting transition [94, 95]. Furthermore, these theoretical results depend on the form of the adsortion potential and generally do not take into account the effect of corrugation (substrate is assumed smooth). In any case, non–wetting transition of liquid $\mathbf{H_2}$ down to 15 K has been assessed, with the exception of Li.

Despite these facts, the general assumption in our 2D model regarding the alkali substrate (monolayer with lattice parameter 10Å) differs significantly from the aforementioned pure cases where the substrate is semi–infinite, smooth and denser (since it is at bulk equilibrium). As we have cited previously, Rb and Na are allowed to form low coverage triangular lattices when are adsorbed on Ag(111), because the valence electron of the atoms polarizes strongly toward the metallic substrate, and then the system results in an ensemble of mutually repulsive dipoles.

To be completely rigorous we should also include the interaction of the Ag substrate with the $\mathbf{H_2}$ molecules in the Hamiltonian of the model, which it is known to be strongly attractive [96]. One example which illustrates the *a priori* importance of including such interactions is found in recent work by Shi *et al.* [94]. In this reference, the authors compute the wetting transition temperature of liquid $\mathbf{H_2}$ above a 15Å thick film of Rb adsorbed on Au; they find that this transition temperature is few kelvins lower than the one predicted on pure Rb.

According to these considerations, Gordillo and Ceperley [78] carried out several simulations of the $\mathbf{H_2}$–Ag system, and deduced a constrained confinement of the hydrogen molecules in the z–direction at a mean distance 2.4Å from the top layer of silver. This height is practically equal to the distance

where alkali layers nucleate above the Ag(111) plane (2.8–3.0Å).

Therefore, the large confinement imposed by the Ag substrate in the z–direction and the weak interaction of the molecules with the alkali atoms in a parallel plane to the silver surface, are reasonable assessments to consider the proposed 2D $\mathbf{H_2}$–alkali model as realistic.

3.4 Molecular ortho–deuterium

Deuterium is a stable isotope of hydrogen two times heavier than it due to an adittional neutron. Analogously to $\mathbf{H}$, deuterium atoms, $\mathbf{D}$, join covalent bonds to form molecules, $\mathbf{D_2}$, which in view of the $\mathbf{H_2}$ bulk case, are expected to freeze at low temperatures in spite of their light weight (equal to that of $^4\mathbf{He}$). The deuterium molecule is a bosonic particle with total angular momentum equal either to 1 (para–$\mathbf{D_2}$) or to 0 (ortho–$\mathbf{D_2}$); our study is focused on the o–$\mathbf{D_2}$ state because is the one with spherical symmetry.

Next on, we present a complementary study to the one in section 3.1, where the isotopic effects concerning the ground state of the p–$\mathbf{H_2}$ film are explored by means of the exact DMC technique.

In our model, the o–$\mathbf{D_2}$ molecules are arranged in a triangular lattice and assumed point–like; the interaction between them is modeled with the Silvera-Goldman potential. The trial wave function adopted in this case is slightly different from (3.3) because the pair–correlation factors, f_2, depend on two variational parameters, namely b and c,

$$\psi_{JG}\left(\mathbf{r_1}, \mathbf{r_2}, ..., \mathbf{r_N}\right) = \prod_{i<j}^{N} e^{-\frac{1}{2}(b/r_{ij})^c} \prod_{i}^{N} e^{-\frac{a}{2}(|\mathbf{r_i}-\mathbf{R_i}|)^2} \ . \tag{3.26}$$

After carrying several VMC runs we found that the set of optimal parameters is b= 3.32 Å c= 7 and a= 0.67 Å^{-2}. All the DMC simulations have been performed with 120 particles within a rectangular plane with periodic boundary conditions applied on the two orthogonal directions. The critical number of walkers, n_w, is 250 and the time step, $\Delta\tau$, 5·10^{-4} K^{-1}.

In Figure 3.9, we have plotted the total energy per particle as a function of the density; the solid line represents the best fit to our data in the form of the polynomial curve (3.10). The value of the parameters are B= 241(3) K, C= 324(10) K, e_0= -42.30(5) K and ρ_0= 0.078 Å^{-2}.

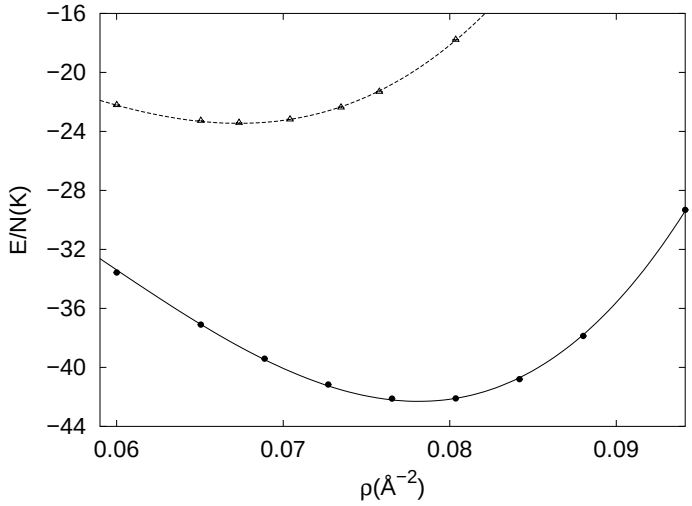

Figure 3.9: Equation of state of solid 2D $\mathbf{D_2}$ at zero temperature (solid line and filled circles). The EOS corresponding to 2D $\mathbf{H_2}$ is also shown (dotted line and empty triangles) for a direct comparison.

By direct comparison with the EOS corresponding to p-$\mathbf{H_2}$ (shown also in Fig.3.9, dotted line), one realizes that in the o–$\mathbf{D_2}$ case the equilibrium density is higher and the binding energy decreases substantially. The comparatively heavier mass of the o–$\mathbf{D_2}$ molecules, forces them to reduce the kinetic energy and mean squared displacement at any given density (see Tables 3.11, 3.12, 3.3 and 3.4). This fact allows the system to increase its equilibrium density in order to take advantage of the interparticle attraction.

With respect to the microscopic structure within the solid $\mathbf{D_2}$ film, we have calculated the radial pair–distribution function at the equilibrium density (Figure 3.10), Lindemann's ratio and kurtosis (Table 3.12). In Figure 3.10 we have shown the radial pair–distribution function of 2D o–$\mathbf{D_2}$ and p–$\mathbf{H_2}$, each of them at its own equilibrium density. The peaks on molecular deuterium are sharper and somehow closer than on hydrogen because the density and degree of localization of the particles are larger. This statement is also corroborated by the results contained in Table 3.12, where the Lindemann's ratio is invariably some tenths smaller than in $\mathbf{H_2}$ at the same density. As it could be expected from the previous study regarding the p–$\mathbf{H_2}$ film, kurtosis in $\mathbf{D_2}$ is

practically vanishing since none direction is preferred by the molecules moving around the equilibrium positions.

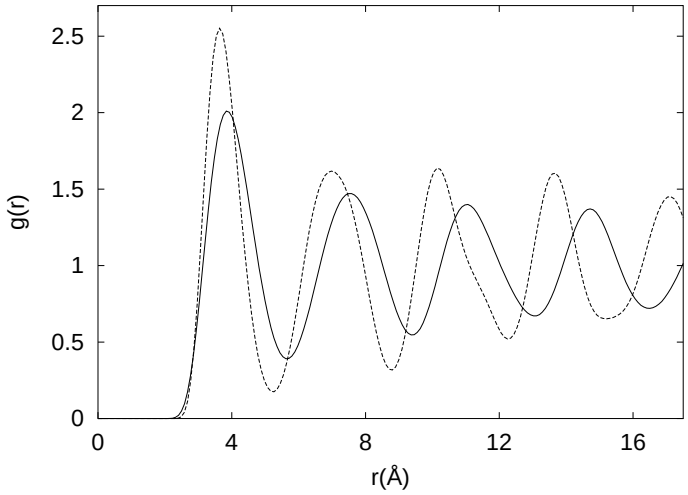

Figure 3.10: Radial pair–distribution functions of solid 2D $\mathbf{D_2}$ at the equilibrium density 0.078 ($Å^{-2}$) (dashed line), and p-$\mathbf{H_2}$ at the equilibrium density 0.068 ($Å^{-2}$) (solid line).

Once the existence of the 2D p-$\mathbf{H_2}$ liquid phase has been rigorously refused, it has no sense to wonder about the same issue in the o–$\mathbf{D_2}$ system, since the mass of the molecules is doubled and the strength of the potential is conserved. It is worth noticing that recent experimental evidence of a stable $\mathbf{D_2}$ liquid phase placed on a krypton pre–plated graphite substrate has been observed at temperature T$\sim$1.5 K [97]. On the expectance of new and more explanatory experimental and theoretical works, molecular deuterium may be regarded as a potential target where to observe similar quantum features to those expected in $\mathbf{H_2}$.

ρ (Å^{-2})	E/N (K)	$\langle V\rangle/N$ (K)	$\langle T\rangle/N$ (K)
0.046	$-22.40(2)$	$-29.12(1)$	$6.72(1)$
0.053	$-27.97(1)$	$-37.31(1)$	$9.34(1)$
0.060	$-33.57(1)$	$-46.26(1)$	$12.70(1)$
0.069	$-39.41(1)$	$-57.36(1)$	$17.96(1)$
0.076	$-42.12(1)$	$-65.81(1)$	$23.70(1)$
0.084	$-40.80(1)$	$-71.62(1)$	$30.82(1)$
0.094	$-29.32(2)$	$-71.97(1)$	$42.65(1)$

Table 3.11: Total and mixed potential and kinetic energies per particle as functions of the density corresponding to 2D $\mathbf{D_2}$ at absolute zero temperature.

ρ(Å^{-2})	γ	$\zeta_{(10)}$	$\zeta_{(01)}$
0.053	$0.204(1)$	$0.00(1)$	$-0.06(2)$
0.060	$0.187(1)$	$0.01(1)$	$0.00(1)$
0.069	$0.160(1)$	$0.00(2)$	$-0.01(1)$
0.073	$0.149(1)$	$-0.01(1)$	$0.01(1)$
0.078	$0.139(1)$	$0.00(1)$	$0.01(1)$
0.080	$0.135(1)$	$-0.02(1)$	$0.00(1)$
0.088	$0.124(1)$	$0.00(1)$	$-0.03(1)$
0.094	$0.117(1)$	$-0.02(1)$	$0.02(1)$

Table 3.12: Lindemann's ratio, γ, and kurtosis, ζ of 2D $\mathbf{D_2}$ are shown at different densities near the equilibrium.

Chapter 4
Ground–state properties of LiH and LiD

4.1 Introduction

Hydrogen forms stable stoichiometric hydrides by reaction with all of the alkali metals: Li, Na, K, Rb and Cs [98]. Since the first x-ray study [99] in 1931, it has been shown that **LiH**, NaH, KH, RbH and CsH (AlkH in short) crystallize with the rock-salt structure (i.e. a fcc with a two-atom basis: Li in $(0,0,0)$ and H (D) shifted by $(a/2)(\mathbf{i}+\mathbf{j}+\mathbf{k})$) at room temperature. In these materials, evidence seems consistent with hydrogen being present in the form of anions or modified anions. Some electron distribution investigations [100], estimated the ionic charge in **LiH** to fall in range from 0.4 to 1.0 electron-charges, indicating that the alkali hydrides are probably very similar to the alkali halides with respect to the electronic structure. In addition, calculations of the electronic charge density in **LiH**, based on the local density approximation, show that most of the electronic charge is transferred from Li to H [101]. Because of this fact, which gives rise to long-range interactions between hydrogen atoms, the H dynamics in these compounds is expected to be very different from the one in group III-VIII metal hydrides. However, only **LiH** and **LiD** have been studied in some detail [102], both theoretically and experimentally.

The choice of lithium hydride and deuteride have not been casual at all: they are rock-salt crystals having only four electrons per unit cell, which makes them the simplest ionic crystals in terms of electronic structure. Moreover, there is a large isotopic effect provided by proton and deuteron exchange. Last but not least, owing to the low mass of their constituent atoms, these two compounds represent a good case for the calculations of the zero-

point motion contribution to the lattice energy. In this respect, they are genuine quantum crystals, somehow related to the hydrogen ($\mathbf{H_2}$ and $\mathbf{D_2}$) [103] or the helium ($^3\mathbf{He}$ and $^4\mathbf{He}$) [30] families. By comparing an important anharmonicity parameter, namely the zero-temperature Lindemann's ratio [104] for H in **LiH**, $\gamma_{\mathrm{H}} = 0.12$, to the ones of other quantum crystals, one finds that H in **LiH** lies in between solid $\mathbf{H_2}$ ($\gamma = 0.18$) and solid **Ne** ($\gamma = 0.09$), placed very close to solid $\mathbf{D_2}$ ($\gamma = 0.14$). Because of these unique physical properties (and also because of their use in thermonuclear weapons) **LiH** and **LiD** are in general fairly well described, even in condition of very high pressure ($p > 10$ GPa), both structurally (neutron diffraction) [105] and dynamically (second-order Raman spectroscopy) [106], and through ab-initio electronic structure simulations [107].

However, as far as complete lattice dynamics works are concerned (i.e. including full phonon dispersion curves), the situation looks much less exhaustive. The **LiD** dispersion curves were measured by coherent inelastic neutron scattering in 1968 [108], even though the longitudinal optical branch was almost unobserved, and subsequently they were fitted through a 7-parameter shell model (SM7) and converted into equivalent **LiH** data. Later on [109], the same data have been fitted again through a more advanced method: a deformation dipole model with 13 adjustable parameters (DDM13), which also provided elastic and dielectric constants, effective charges, second order Raman spectra etc., all in good (or fair) agreement with the known experimental values. The only noticeable exception was represented by the H-projected density of phonon states (H-DoPS) for **LiH** [110],

$$Z_{\mathrm{H}}(\omega) = \frac{1}{3N} \sum_{\mathbf{q}} \sum_{j=1}^{6} |\mathbf{e}_{\mathrm{H}}(\mathbf{q}, j)|^2 \, \delta(\omega - \omega(\mathbf{q}, j)) \; , \tag{4.1}$$

where $\mathbf{q}$ is a phonon wave-vector contained in the first Brillouin zone, N is the number of these wave-vectors, j is labeling the six phonon branches, $\mathbf{e}_{\mathrm{H}}(\mathbf{q}, j)$ is the polarization vector for H, and $\omega(\mathbf{q}, j)$ is the phonon frequency.

Both **LiH** H-DoPS deduced from SM7 and DDM13 turned to be rather different from the old incoherent inelastic neutron scattering measurement [111]. In addition, both SM7 and DDM13 are force constant models and do not provide any suitable inter–ionic potential scheme for **LiH**.

The potential approach was first attempted by Hussain and Sangster [112], who tried to include alkali hydrides in a larger potential scheme derived for all the alkali halides making use of the Born-Mayer functional form. Considering the little number of adjustable parameters (i.e. 3), the **LiD** dispersion curves obtained from this potential are quite in good agreement with the coherent neutron scattering data [108]. However, the existence of some problems in this scheme for **LiH** (e.g. the H-H Pauling parameter turned out to be unphysical, the elastic constants were too large etc.), prompted Haque and Islam [113] to devise a new set of potentials (HI) for both **LiH** and NaH. Nevertheless, despite their better description of some of the macroscopic properties of **LiH** and their superior physical soundness, the HI potential does not provide any advantage over the older one as far as the dispersion curves are concerned.

Finally, it is worth mentioning an important ab-initio calculation of the **LiD** dispersion curves [114], which correctly included the zero-point effects in the lattice energy minimization procedure.

Regarding thermodynamics, accurate constant-pressure specific heat measurements on **LiH** and **LiD** in the temperature range T = (4-300) K are reported by Yates and co-workers [115]. These experimental results, once corrected for thermal expansion with the help of temperature dependent lattice parameters [116] were used to extract the effective Debye temperature, Θ_D, as a function of T. The relative thermal variation of Θ_D in **LiH** was found to be very large, 20% between 4 K and 80 K and more than 30% between 80 K and room temperature. This fact comes to reveal a strong anharmonicity in the **LiH** lattice dynamics. Later, a comparison between experimental $\Theta_D(T)$ data and the DDM13 results of Dyck and Jex [109] was made. The agreement was found quite good between 30 K and 300 K, while for temperature values below 20 K some anomalies in the behavior of the experimental specific heat were found. The measured heat capacity displays a peak at $T_c = 11.1$ K (for **LiH**), the origin of which has not yet been discovered, although the possibility of a phase transition to a CsCl-type structure has been suggested [115]. The specific heat measurements in the reported temperature range are mainly sensitive to the details of the phonon density of states in its low energy region (say $0 - 30$ meV) [117], which lies for **LiH** in the acoustic band, spanning the phonon energies in the $(0 - 70)$ meV range. Thus, unfortunately, thermody-

namics seems rather unable to probe the real H dynamics in **LiH**.

It is consistent to believe that the combined use of incoherent inelastic neutron scattering, from which the H-DoPS can be worked out, and of fully quantum simulations, from which important equilibrium physical quantities can be derived (mean squared displacement, mean kinetic energy and Einstein frequency), can provide a new and deep insight into the problem of quantum hydrogen dynamics in condensed matter.

This chapter is developed according to the following scheme: the experimental H-DoPS (Hydrogen-Density of Phonon State) deduced from a neutron scattering experiment on **LiH** and the indirect measurements derived from it, are firstly shown. Next, the simulation technique, namely the variational Monte Carlo, and the results obtained through it are presented. Then, a comparison between the quantities derived from the experimental spectra and the estimates obtained through the variational Monte Carlo simulations, and other less advanced techniques, is established. Finally, an analogous theoretical study of **LiD** is presented in order to study the isotopic effects induced on **LiH**.

4.2 Lithium Hydride

4.2.1 Experimental and data analysis

The referred neutron scattering experiment was carried out by D. Colognesi and M. Zoppi on TOSCA–II, a crystal-analyzer inverse-geometry spectrometer [118] operating at the ISIS pulsed neutron source (Rutherford Appleton Laboratory, Chilton,Didcot, UK). The technical aspects of the experiment are described with great detail in Ref. [119], here we just present the experimental output and its later analysis.

Once Colognesi and Zoppi obtained the experimental TOF (time-of-flight) spectra corresponding to **LiH** at room temperature T=20 K, they carried out non-trivial transformations and energy corrections on it, in order to deduce the H-projected density of phonon states in **LiH**, $Z_{\mathrm{H}}(\omega)$, defined as

$$
\begin{aligned}
Z_{\mathrm{H}}(\omega) &= \exp\left(2W(Q)\right)\ S_{s,1}(Q,\omega)\frac{4m_{\mathrm{H}}\omega}{\hbar Q^2}\left[\coth\left(\frac{\hbar\omega}{2k_BT}\right)+1\right]^{-1}\ , \\
2W(Q) &= \frac{\hbar Q^2}{2m_{\mathrm{H}}}\int_0^\infty d\omega\frac{Z_{\mathrm{H}}(\omega)}{\omega}\coth\left(\frac{\hbar\omega}{2k_BT}\right)
\end{aligned}
\tag{4.2}
$$

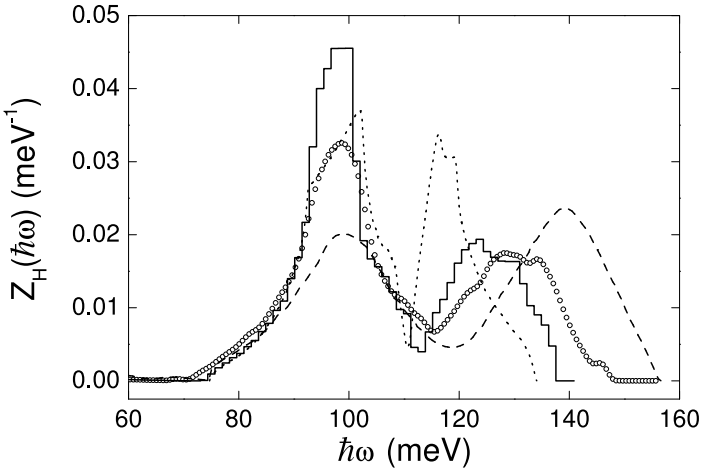

Figure 4.1: Hydrogen projected density of phonon states in **LiH**. The experimentally-determined result is plotted as circles, the full line represents a DDM13 lattice dynamics simulation [109], the dashed line a SM7 lattice dynamics simulation [108], and the dotted line the old neutron measurement [111].

where $S_{s,1}(Q,\omega)$ and $W(Q)$ are the one-phonon component of the experimental scattering law and Debye-Waller factor, respectively. The technicalities along the whole analytical process followed to obtain $Z_{\rm H}(\omega)$ are properly described in Ref. [120].

The resulting $Z_{\rm H}(\omega)$ is plotted in Fig.4.1. Equations (4.2), and the other in [120] used to work out $Z_{\rm H}(\omega)$, are formally exact only in the framework of the harmonic approximation, but they have a practical validity which is far more general, as explained by Glyde [30] in the context of solid helium. From $Z_{\rm H}(\omega)$, making use of normal and Bose-corrected moment sum rules [121], we are able to derive three important quantities related to the hydrogen dynamics in this hydride, namely the H mean squared displacement $\langle \mathbf{u}_{\rm H}^2 \rangle$, the H mean kinetic energy $\langle T_{\rm H} \rangle$, and the H Einstein frequency, $\Omega_{0,{\rm H}}$:

$$\begin{aligned}
\langle \mathbf{u}_{\mathrm{H}}^2 \rangle &= \frac{3\hbar}{2m_{\mathrm{H}}} \int_0^\infty d\omega \frac{Z_{\mathrm{H}}(\omega)}{\omega} \coth\left(\frac{\hbar\omega}{2k_B T}\right) , \\
\langle T_{\mathrm{H}} \rangle &= \frac{3\hbar}{4} \int_0^\infty d\omega Z_{\mathrm{H}}(\omega)\, \omega \coth\left(\frac{\hbar\omega}{2k_B T}\right) , \\
\Omega_{0,\mathrm{H}}^2 &= \int_0^\infty d\omega Z_{\mathrm{H}}(\omega)\, \omega^2 . \qquad (4.3)
\end{aligned}$$

The deduced experimental results are $\langle \mathbf{u}_{\mathrm{H}}^2 \rangle$ = 0.062(1) Å^2, $\langle T_{\mathrm{H}} \rangle$ = 80(1) meV, $\hbar\Omega_{0,\mathrm{H}}$ = 109.2(9) meV.

4.2.2 Variational Monte Carlo Simulation

We have studied the ground-state properties of solid **LiH** by means of the variational Monte Carlo (VMC) method [64]. VMC is a fully quantum approach which relies on the variational principle. Assuming only pair-wise interactions between the different atoms in the crystal, the Hamiltonian describing **LiH** is:

$$H = -\frac{\hbar^2}{2m_{\mathrm{H}}} \sum_{i=1}^{N_{\mathrm{H}}} \nabla_i^2 - \frac{\hbar^2}{2m_{\mathrm{Li}}} \sum_{i=1}^{N_{\mathrm{Li}}} \nabla_i^2 + \sum_{i<j}^{N_{\mathrm{H}}} V^{(\mathrm{H,H})}(r_{ij}) + \sum_{i<j}^{N_{\mathrm{Li}}} V^{(\mathrm{Li,Li})}(r_{ij}) + \sum_{i,j}^{N_{\mathrm{H}},N_{\mathrm{Li}}} V^{(\mathrm{H,Li})}(r_{ij}) \qquad (4.4)$$

where r_{ij} is the distance between the atoms composing an i,j pair; m_{Li} is the Li average atomic mass; N_{H} and N_{Li} stand for the number of H and Li atoms, respectively; and $V^{(\mathrm{H,H})}$, $V^{(\mathrm{Li,H})}$ and $V^{(\mathrm{Li,Li})}$ represent the three pair-wise interaction potentials.

The variational principle states that for a given trial wave function Ψ, the expected value of H is an upper bound to the ground-state energy E_0:

$$\frac{\langle \Psi | H | \Psi \rangle}{\langle \Psi | \Psi \rangle} = E \geq E_0 . \qquad (4.5)$$

The multidimensional integral required in the calculation of Eq.(4.5) can not be evaluated exactly by analytical summation methods, like the hypernetted

chain formalism [124]. However, a stochastic interpretation of this integral is rather straightforward, and this is actually the task carried out by the VMC method, with the only cost of some statistical noise.

The trial wave function chosen for importance sampling corresponds to the extensively tested Nosanow–Jastrow model [30, 7]

$$\Psi = F\Phi \; . \tag{4.6}$$

The Jastrow factor F contains two-body correlation functions between the different pairs $f^{(\mathrm{H,H})}$, $f^{(\mathrm{Li,Li})}$ and $f^{(\mathrm{H,Li})}$:

$$F = \prod_{i<j}^{N_{\mathrm{H}}} f^{(\mathrm{H,H})}(r_{ij}) \prod_{i<j}^{N_{\mathrm{Li}}} f^{(\mathrm{Li,Li})}(r_{ij}) \prod_{i,j}^{N_{\mathrm{H}},N_{\mathrm{Li}}} f^{(\mathrm{H,Li})}(r_{ij}) \; , \tag{4.7}$$

and Φ localizes each particle around the lattice equilibrium sites of the crystal phase $\mathbf{R}_i^{\alpha}$ through the functions $g^{(\mathrm{H})}$ and $g^{(\mathrm{Li})}$:

$$\Phi = \prod_{i}^{N_{\mathrm{H}}} g^{(\mathrm{H})}(|\mathbf{r}_i - \mathbf{R}_i^{\mathrm{H}}|) \prod_{i}^{N_{\mathrm{Li}}} g^{(\mathrm{Li})}(|\mathbf{r}_i - \mathbf{R}_i^{\mathrm{Li}}|) \; . \tag{4.8}$$

The VMC simulation is carried out at a molar volume v_0 = 10.059 cm^3 which is the experimentally estimated value at zero pressure and zero temperature [105, 122]. The lattice constant, derived from the experimental molar volume v_0, is a = 4.0578 Å. The calculation is worked out with a simulation box containing 108 particles of each type with periodic boundary conditions. We have checked that this number of particles is large enough for practically eliminating size effects on the more relevant quantities in the present study: the H mean kinetic energy, its mean squared displacement around the lattice sites, and its Einstein frequency.

As we have seen in the introductory section, **LiH** and the rest of hydrides and deuterides of light alkali metals are well described as ionic crystals. This nearly perfect ionic bonding allows for a model in which ions H^- and Li^+, both with a $1s^2$ electronic configuration, are occupying the lattice sites of the crystal. The present simulation relies on this model, assuming rigid closed-shell ions interacting via central interatomic potentials. The overlap repulsion potential between the ions is taken from the semi-empirical Born-Mayer interaction [123], and van der Waals attractive terms are also included to deal

with polarizability effects. According to this general scheme, as previously mentioned, Haque and Islam [113] proposed their pair potential $V_{\rm HI}^{(\alpha,\beta)}(r)$:

$$V_{\rm HI}^{(\alpha,\beta)}(r) = B_{\alpha\beta}\exp\left(-A_{\alpha\beta}r\right) - \frac{C_{\alpha\beta}}{r^6}\,, \tag{4.9}$$

with $\{\alpha,\ \beta\}$= Li, H. The set of parameters entering $V_{\rm HI}^{(\alpha,\beta)}(r)$ is reported in Table 4.1. In order to evaluate the influence of the interatomic potentials in our results we have also used the model proposed by Sangster and Atwood [125], $V_{\rm SA}^{(\alpha,\beta)}(r)$:

$$V_{\rm SA}^{(\alpha,\beta)}(r) = B_{\alpha\beta}\exp\left[A_{\alpha\beta}\left(E_{\alpha\beta}+F_{\alpha\beta}-r\right)\right] - \frac{C_{\alpha\beta}}{r^6} - \frac{D_{\alpha\beta}}{r^8}\,, \tag{4.10}$$

which incorporates a dipole-quadrupole attractive term. The parameters for **LiH**, which are taken from Hussain and Sangster [112], are reported in Table 4.2.

The main task in a variational approach like the present one is to seek for a good trial wave function Ψ (Eqs.(4.6- 4.8)). Like in solid helium calculations [7], we have chosen analytical two-body $f^{(\alpha,\beta)}(r)$ (see Eq.(4.7)) and one-body $g^{(\alpha)}(r)$ (see Eq.(4.8)) correlation factors with a set of free parameters to be optimized. In particular, $f^{(\alpha,\beta)}(r)$ is of McMillan type [38]:

$$f^{(\alpha,\beta)}(r) = \exp\left[-\frac{1}{2}\left(\frac{b_{\alpha\beta}}{r}\right)^5\right], \tag{4.11}$$

and the specific phase factor is a Gaussian centered on the sites of the crystal lattice:

$$g^{(\alpha)}(r) = \exp\left(-\frac{1}{2}\,c_\alpha r^2\right). \tag{4.12}$$

In the optimization search the absolute minimum of the internal energy $\langle H\rangle_\Psi$ is looked for. However, the number of parameters is large enough to make this optimization rather difficult. In order to discern between local minima of similar quality we have also calculated the energy of the solid including Coulomb contributions, considering the ions as point-like particles. Under this criterion, the final parameter set is the one which simultaneously minimizes the short-range energy and the total energy including Coulomb contributions. The values obtained, which are the same for the two short-range potentials $V_{\rm HI}$ and $V_{\rm SA}$, are: $c_{\rm Li}$ = 150 Å^{-2}, $c_{\rm H}$ = 15 Å^{-2}, $b_{\rm LiH}$ = 2.0 Å,

α	β	$A_{\alpha\beta}$(Å^{-1})	$B_{\alpha\beta}$(eV)	$C_{\alpha\beta}$(eVÅ^6)
Li	Li	7.3314	1153.80	0.0
Li	H	3.1000	187.29	0.0
H	H	5.5411	915.50	4.986

Table 4.1: Parameters of the $V_{\rm HI}^{(\alpha,\beta)}(r)$ potential by Haque and Islam [113].

α	β	$A_{\alpha\beta}$(Å^{-1})	$B_{\alpha\beta}$(eV)	$E_{\alpha\beta}$(Å)	$F_{\alpha\beta}$(Å)	$C_{\alpha\beta}$(eVÅ^6)	$D_{\alpha\beta}$(eVÅ^8)
Li	Li	38.48731	17.8000	0.2226	0.2226	0.0549073	0.0216285
Li	H	3.784068	0.17675	0.2226	1.9000	0.9568660	2.0013052
H	H	2.608380	0.01422	1.9000	1.9000	48.872096	185.18284

Table 4.2: Parameters of the $V_{\rm SA}^{(\alpha,\beta)}(r)$ potential proposed by Sangster and Atwood [125], estimated by Hussain and Sangster [112].

$b_{\rm LiLi}$ = 1.5 Å, and $b_{\rm HH}$= 1.0 Å. Among the three $b_{\alpha\beta}$ Jastrow parameters, the most important is the cross one ($b_{\rm LiH}$), since the first neighbours of a H^- ion are Li^+, and vice versa. It is worth noticing that the optimal values for c_α reflect the difference in the degree of localization around the sites between the two ions due to their significantly different masses, $c_{\rm H} << c_{\rm Li}$. Including the Coulomb potential in the energy, the energies per particle are -5.07(2) eV and -5.32(2) eV for the $V_{\rm HI}$ and $V_{\rm SA}$ short-range potentials, respectively.

Information on the spatial structure of the solid can be drawn from the two-body radial distribution functions $g^{(\alpha,\beta)}(r)$. In Fig.4.2, results for the three components $g^{(\alpha,\beta)}(r)$ are shown. As expected, the location of the peaks follows the interparticle pattern imposed by the lattice: each ion is surrounded by ions of opposite sign and ions of equal sign are distributed with the same periodicity. The major mobility of H^- with respect to Li^+ is also observed by comparing the height and the spreading around the sites of $g^{(\rm Li,Li)}(r)$, on one hand, and $g^{(\rm H,H)}(r)$ and to a lesser extend $g^{(\rm Li,H)}(r)$, on the other.

A structural quantity which can be directly compared with the present

experimental data is the mean squared displacement of the H^- ions, $\langle \mathbf{u}_{\rm H}^2 \rangle$

$$\langle \mathbf{u}_{\rm H}^2 \rangle = \frac{1}{N_{\rm H}} \left\langle \sum_{i=1}^{N_{\rm H}} \left(\mathbf{r}_i - \mathbf{R}_i^{\rm H} \right)^2 \right\rangle \ . \tag{4.13}$$

Using the trial wave function quoted above, the VMC result is $\langle \mathbf{u}_{\rm H}^2 \rangle$ = 0.074(2) Å^2. The resulting Lindemann's ratio:

$$\gamma_{\rm H} = \frac{2\sqrt{\langle \mathbf{u}_{\rm H}^2 \rangle}}{a} \ , \tag{4.14}$$

is 0.134. Additional insight on the spatial localization of H^- can be obtained by calculating the H^- density profile $u_{\rm H}(r)$, with r the distance of the ion to its site. The function $u_{\rm H}(r)$ is shown in Fig.4.3; it is very well parameterized by a Gaussian with the VMC expected value $\langle \mathbf{u}_{\rm H}^2 \rangle$ = 0.074(1) Å^2 (see the solid line in the same figure).

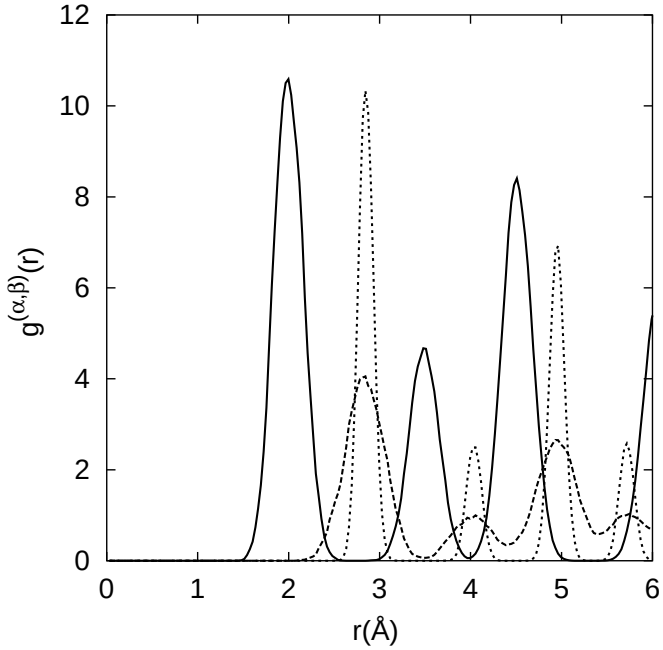

Figure 4.2: Two-body radial distribution functions in **LiH**: $g^{(\rm H,Li)}(r)$, solid line; $g^{(\rm H,H)}(r)$, dashed line; $g^{(\rm Li,Li)}(r)$, dotted line.

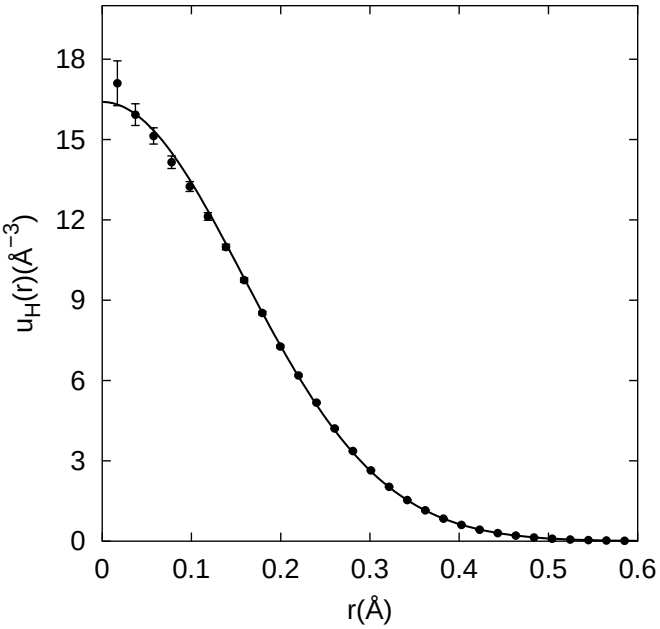

Figure 4.3: Variational Monte Carlo result for the H^- density profile, $u_{\rm H}(r)$, in **LiH**. The solid line corresponds to a Gaussian with a mean squared displacement equal to the variational Monte Carlo value $\langle \mathbf{u}_{\rm H}^2 \rangle$ = 0.074 Å^2.

The kinetic energy per particle of H^- is one of the partial contributions to the total energy of the solid, which is evaluated at each step of the VMC simulation. It is the expected value of the operator:

$$\langle T_{\rm H} \rangle = -\frac{\hbar^2}{2m_{\rm H}N_{\rm H}} \left\langle \sum_{i=1}^{N_{\rm H}} \frac{\nabla_i^2 \Psi}{\Psi} \right\rangle , \tag{4.15}$$

with configuration points generated according to the probability distribution function $|\Psi|^2$. As in the estimation of $\langle \mathbf{u}_{\rm H}^2 \rangle$, the H^- kinetic energy is the same for the two interatomic potentials (Eqs. 4.9,4.10) since the optimization procedure has led to the same variational wave function. The result obtained is $\langle T_{\rm H} \rangle$ = 84(1) meV.

The third physical quantity evaluated in the present experiment, the Einstein frequency $\Omega_{0,\rm H}$, can be calculated in a VMC simulation through its pro-

per definition:

$$\Omega_{0,\mathrm{H}}^2 = \frac{1}{3m_{\mathrm{H}}N_{\mathrm{H}}} \left\langle \sum_{i=1}^{N_{\mathrm{H}}} \nabla_i^2 V_{\mathrm{H}}(\mathbf{r}_i) \right\rangle , \tag{4.16}$$

where the expected value of $\nabla_i^2 V_{\mathrm{H}}(r)$ is calculated over the configurations generated by the probability distribution function $|\Psi|^2$, and $V_{\mathrm{H}}(r)$ is the potential felt by an ion H^-:

$$V_{\mathrm{H}}(\mathbf{r}_i) = \frac{1}{2}\sum_{j\neq i}^{N_{\mathrm{H}}} V^{(\mathrm{H,H})}(r_{ij}) + \frac{1}{2}\sum_{j=1}^{N_{\mathrm{Li}}} V^{(\mathrm{H,Li})}(r_{ij}) . \tag{4.17}$$

The result obtained applying Eq. (4.16) is $\hbar\Omega_{0,\mathrm{H}}$ = 110.3(5) meV.

4.2.3 Discussion

The aim of this discussion section is twofold: 1) comparing the outputs of the experimental and theoretical approaches, namely IINS and VMC simulations; 2) finally, shedding some light on the important point of the possible quantum anharmonic effects on the H^- dynamics in low-temperature **LiH**.

Comparison between IINS and VMC results

Since VMC is a ground-state method, $Z_{\mathrm{H}}(\omega)$ can not be directly evaluated. However, through the aforementioned normal and Bose-corrected moment sum rules in Eqs.(4.3), it was possible to describe the main features of the H-DoPS via $\langle \mathbf{u}_{\mathrm{H}}^2 \rangle$, $\langle T_{\mathrm{H}} \rangle$ and $\Omega_{0,\mathrm{H}}$, which are equilibrium quantities calculated by the VMC code. Before proceeding with this comparison, it is worth noticing that the VMC calculation is performed at zero temperature, whereas the measure is accomplished at T=20.1(1) K. But thermal effects are negligible since the Debye temperature of **LiH** is approximately 1100 K [102], and therefore the measured system can be certainly considered in its ground state, at least as far as the H^- ion dynamics is concerned. This assumption can be easily proved by calculating (always from the experimental $Z_{\mathrm{H}}(\omega)$) the zero-point values of the H mean squared displacement and mean kinetic energy, setting T=0 : $\langle \mathbf{u}_{\mathrm{H}}^2 \rangle(T=0)$ = 0.062(1) Å^2 and $\langle T_{\mathrm{H}} \rangle(T=0)$ = 80(1) meV, identical within the errors to the values estimated at T=20.1 K.

Going back to VMC, one can notice a value of the zero-point H mean squared displacement (0.074(2) Å^2) slightly higher than the IINS experimental measure. In addition these two figure have to be compared to the most recent neutron diffraction estimate by Vidal and Vidal-Valat [126] $\langle \mathbf{u}_{\mathrm{H}}^2 \rangle$ = 0.0557 (6) Å^2 (extrapolated at T=20 K by the present authors from the original data in the temperature range 93 K-293 K), which appears close but still discrepant from the VMC and IINS findings. However, it has to be pointed out that a previous room-temperature diffraction result by Calder *et al.* [100], $\langle \mathbf{u}_{\mathrm{H}}^2 \rangle$ = 0.068(1) Å^2, seems to exhibit a similar trend if compared to the Vidal and Vidal-Valat's figure in the same conditions: $\langle \mathbf{u}_{\mathrm{H}}^2 \rangle$ = 0.0650(6) Å^2. On the other hand, for the other two aforementioned physical quantities, the agreement between IINS ($\langle T_{\mathrm{H}} \rangle$ = 80(1) meV, $\hbar\Omega_{0,\mathrm{H}}$ = 109.2(9) meV) and VMC ($\langle T_{\mathrm{H}} \rangle$ = 84(1) meV, $\hbar\Omega_{0,\mathrm{H}}$ = 110.3(5) meV) is much more satisfactory, confirming the validity of our combined IINS-VMC method.

An interesting test on the obtained results can be accomplished in the framework of an approximate estimation known as the Self Consistent Average Phonon (SCAP) formalism [127, 32]. The SCAP approach relies on the well-known Self Consistent Phonon (SCP) method, but replacing the sums of functions of the phonon frequencies by appropriate functions of an average-phonon frequency [32]. Results for quasi-harmonic and harmonic solids like **Ne**, Kr, and Xe obtained using SCAP have shown good agreement with experimental data. The application of this formalism to quantum crystals seems however more uncertain due to the relevant increase of anharmonicity. As **LiH** seems to be a quantum crystal, but with less anharmonicity than for example ^{4}**He**, SCAP can somehow help in the present study. Normally SCAP is used to evaluate various physical quantities in an iterative way, employing lattice parameters and interatomic potentials only [127]. Here, on the contrary, the method will be applied in one single step, starting from "exact" values of $\Omega_{0,\mathrm{H}}$. To this end, we have calculated via SCAP (at $T = 0$) the H mean squared displacement and mean kinetic energy using the relations:

$$\begin{aligned} \langle \mathbf{u}_{\mathrm{H}}^2 \rangle^{(\mathrm{SCAP})} &= \frac{3\hbar}{2m_{\mathrm{H}}\Omega_{0,\mathrm{H}}} , \\ \langle T_{\mathrm{H}} \rangle^{(\mathrm{SCAP})} &= \frac{1}{2}\, m_{\mathrm{H}} \langle \mathbf{u}_{\mathrm{H}}^2 \rangle^{(\mathrm{SCAP})} \Omega_{0,\mathrm{H}}^2 = \frac{3}{4}\hbar\Omega_{0,\mathrm{H}} . \end{aligned} \tag{4.18}$$

The results obtained through this approximation are: $\langle \mathbf{u}_{\mathrm{H}}^2 \rangle^{(\mathrm{SCAP-VMC})}$ = 0.0564(3) Å^2, $\langle \mathbf{u}_{\mathrm{H}}^2 \rangle^{(\mathrm{SCAP-IINS})}$ = 0.0570(5) Å^2, $\langle T_{\mathrm{H}} \rangle^{(\mathrm{SCAP-VMC})}$ = 82.7(4) meV, and $\langle T_{\mathrm{H}} \rangle^{(\mathrm{SCAP-IINS})}$ = 81.9(7) meV. By comparing these approximated values with the microscopic ones, one realizes that the H mean kinetic energy values come out very close, but the SCAP values of the mean squared displacement are significantly smaller, actually not far from the neutron diffraction result by Vidal and Vidal-Valat [126]. The physical meaning of these results is straightforward: both SCAP equations are exact at $T = 0$ in presence of a purely harmonic Einstein solid (i.e. if $Z_{\mathrm{H}}(\omega) = \delta(\omega - \Omega_{0,\mathrm{H}})$). But if the solid system exhibits a broader H-DoPS, $\langle \mathbf{u}_{\mathrm{H}}^2 \rangle^{(\mathrm{SCAP})}$ comes out rather underestimated because $\Omega_{0,\mathrm{H}}^2$ is exactly computed stressing the high-frequency part of $Z_{\mathrm{H}}(\omega)$ via the integrand factor ω^2 (as in Eqs. (4.3)). In this way, one somehow corrects for this bias by expressing the zero-point mean kinetic energy as the product of $\langle \mathbf{u}_{\mathrm{H}}^2 \rangle^{(\mathrm{SCAP})}$ times $\Omega_{0,\mathrm{H}}^2$, because $\langle T_{\mathrm{H}} \rangle$ would be exactly evaluated via the integrand factor ω (see Eqs.(4.3)), which still stress the high-frequency part of $Z_{\mathrm{H}}(\omega)$ but less than $\Omega_{0,\mathrm{H}}^2$. Nevertheless, it is quite remarkable the good accuracy achieved by this relatively simple approach in evaluating the mean kinetic energy, probably beyond what is a priori expected for a system with a possible quantum-crystal character like **LiH**.

Possible quantum anharmonic effecs in LiH

Given the relatively large value of the H Lindemann's ratio in **LiH** (γ_{H}= 0.13 as seen above), it is natural to inquire on the low-temperature anharmonic effects in the H^- ion dynamics. In this respect our tools are well suited since VMC is a microscopic quantum technique wich neither assumes the harmonic approximation, as the usual lattice dynamic calculations does, nor the semi-classical treatment of the particle motion, as the molecular dynamics approach considers [128]. The method applied to test the existence of possible quantum anharmonic effecs in **LiH** (at $T = 0$) was simply devised running the same VMC code in a "harmonic way", i.e. replacing for every atomic pair

i, j the exact pair potential value $V^{(\alpha,\beta)}(r_{ij})$ by [117]:

$$V^{(\alpha,\beta)}(r_{ij}) \simeq V^{(\alpha,\beta)}(r_{0,ij}) + \frac{1}{2}\left(\mathbf{u}_i - \mathbf{u}_j\right)^{\mathrm{T}} \left(\frac{\partial^2 V^{(\alpha,\beta)}}{\partial \mathbf{r}_{ij} \partial \mathbf{r}_{ij}}\right)_{r_{ij}=r_{0,ij}} \left(\mathbf{u}_i - \mathbf{u}_j\right) \ , \tag{4.19}$$

where $\mathbf{r}_i$ and $\mathbf{u}_i$ are the instantaneous position of an i atom and its displacement from the equilibrium position, respectively, while $\mathbf{r}_{ij}$ stands for the vector $\mathbf{r}_i - \mathbf{r}_j$, and $r_{0,ij}$ is the equilibrium separation of an atomic pair i, j. It is worth noting that both the static potential energy $V^{(\alpha,\beta)}(r_{0,ij})$ and the Hessian components are all calculated only once per each atomic pair i, j, since they depend only on the equilibrium distance $r_{0,ij}$. However the "harmonic" results from VMC did not show any significant difference (within their uncertainties) from the "exact" ones, proving at least that in the framework of the semi-empirical pair potentials employed quantum anharmonic effects are totally negligible in the evaluation of $\langle \mathbf{u}_{\mathrm{H}}^2 \rangle$ of $\langle T_{\mathrm{H}} \rangle$ at $T = 0$.

Summary

Dynamical properties of solid **LiH** at low temperature have been studied using a neutron scattering experiment with higher accuracy than previous measures. The analysis of the scattering data has allowed for the estimation of three relevant quantities intimately related to the microscopic dynamics of H in the solid: its mean squared displacement, kinetic energy, and Einstein frequency. Apart from the intrinsic interest in an accurate quantitative determination of these magnitudes we have tried to shed light on two fundamental questions on the physical nature of **LiH**, i.e., its quantum character and its degree of anharmonicity. To this end, and also to make a direct comparison with theory, we have carried out a quantum microscopic calculation of the same three quantities quoted above using VMC.

The consideration of solid **LiH** as a quantum solid is already justified by its Lindemann's ratio which is smaller than the two paradigms, ^{4}**He** and ^{3}**He**, but still appreciably larger than the common values in classical solids. From a theoretical viewpoint, it supposes the unavoidable introduction of at least two-body correlations to account correctly for its ground-state properties. We

have verified using VMC that this feature also holds in solid **LiH**. A somehow more quantitative check of its quantum nature [30] is the comparison between the zero-point kinetic energy from the Debye model and the VMC kinetic energy, which agrees with the experimental one. In the Debye model, the zero-temperature kinetic energy is estimated to be $T_{\rm D} = 9/16\,\theta_{\rm D}$, with $\theta_{\rm D}$ the Debye temperature; considering $\theta_{\rm D}$ = 1100 K, $\langle T_{\rm H}\rangle \simeq 1.7 T_{\rm D}$, not far from the factor 2 estimated in solid ^{4}He [30].

The degree of anharmonicity has been established by comparing the full VMC calculation with another one in which the real interatomic potentials have been substituted by harmonic approximations (Eq. 4.19). As commented in the previous Section, both VMC simulations generate identical results and then possible anharmonic effects are not observed. This situation is different from the one observed in solid **^{4}He** where quantum character and anharmonicity appear together. Apart from the appreciable difference between both systems looking at their respective Lindemann's ratios, a relevant feature that can help to understand the absence of anharmonicity in **LiH** is the significant difference between the interatomic potentials at short distances in both systems. Helium atoms interact with a hard core of Lennard-Jones type whereas the short-range interaction between the components of the mixture **LiH** is much softer (exponential type) according to the Born-Mayer model.

The agreement achieved between the neutron scattering data and the variational Monte Carlo calculation is remarkably good and probably better than what initially could be expected from the use of semiempirical interactions. The VMC predictions for the H kinetic energy and Einstein frequency coincide within error bars with the experimental measures. On the contrary, the H mean squared displacement is $\sim$15% larger. This points to probable inaccuracies of the model potentials, in particular, to cores of size smaller than the real ones. The *ab initio* calculation of more realistic pair interactions could help enormously to improve a microscopic description of **LiH** and justify for the future the use techniques beyond VMC like the diffusion Monte Carlo (DMC) or path integral Monte Carlo (PIMC) methods.

	T_α(meV)	u^2_α(Å^2)	$\hbar\Omega_{0,\alpha}$(meV)	γ_α
H^-	84(1)	0.074(2)	110.3(5)	0.134
D^-	67(1)	0.043(2)	93.6(5)	0.102

Table 4.3: Kinetic energy per particle T_α, mean squared displacement u^2_α, Einstein frequency $\hbar\Omega_{0,\alpha}$, and Lindemann's ratios γ_α for H^- and D^- ions in **LiH** and **LiD**. The figures in parenthesis are the statistical errors.

4.3 Lithium Deuteride

In the present section, we present microscopic results for the ground state of the D^- ions in solid **LiD** by using the variational Monte Carlo (VMC) method [129]. Keeping in mind the previous agreement between our theoretical calculations in **LiH** and the corresponding incoherent inelastic neutron scattering data, we have extended our study to **LiD** in order to elucidate the relevance of quantum isotopic effects.

The crystalline structure of **LiD** is a fcc lattice with a two-atom basis involving the Li^+ and D^- ions and parameter equal to 4.044 Å [102]. The Coulomb interaction between the ions is the responsible of the cohesion of the solid, while short-range interactions are globally repulsive and smaller in magnitude. The overlap repulsion potential takes the form of the Born-Mayer interaction and includes the usual van der Waals attractive term. We have adopted the Sangster and Atwood [125] interatomic potential which additionally incorporates a term for the dipole-quadrupole attraction (equation (4.10)). The values of the parameters are the same that in the H^- case (see Table 4.2).

The trial wave function used in the VMC calculations is also described by equations (4.6), (4.7) and (4.8) with parameters $b_{\rm DD} = 1.5$ Å, $b_{\rm LiLi} = 1.5$ Å, $c_{\rm D} = 30$ Å^{-2}, and $c_{\rm Li} = 150$ Å^{-2}.

We have estimated the mean squared displacement, mean kinetic energy and the Einstein frequency of the D^- ion. The results are shown in Table 4.3 where the same magnitudes referred to the H^- ion have been included to facilitate the comparison.

Observing the results for H^- and D^- one can see that the larger mass of

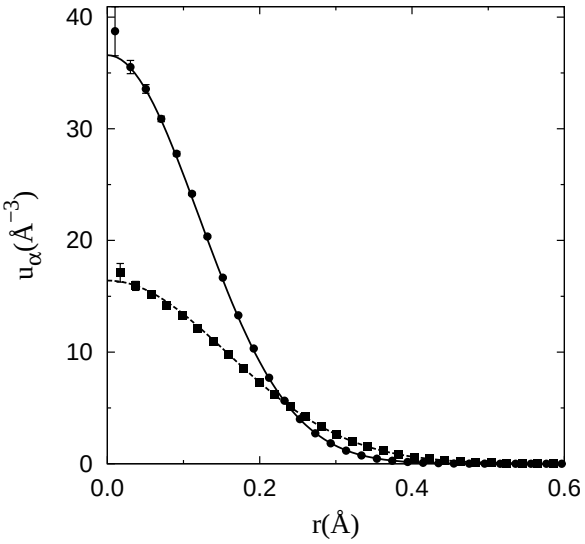

Figure 4.4: H^- (circles) and D^- (squares) density profiles in **LiH** and **LiD**, respectively. The lines on top of the data correspond to Gaussians with the mean displacement reported in Table 4.3.

D^- translates into a lower kinetic energy and mean squared displacement; a comparison between the density profiles of both ions is shown in Fig.4.4.

Using SCAP theory [127, 32], the mean squared displacement and the kinetic energy are simple analytical functions of the Einstein frequency. Considering the values for $\hbar\Omega_{0,\alpha}$, reported in Table 4.3, the SCAP results are: $T_{\rm H}^{\rm (SCAP)}$ = 82.7(4) meV, $T_{\rm D}^{\rm (SCAP)}$ = 70.2(4) meV, $u_{\rm H}^{2\,\rm (SCAP)}$ = 0.0564(3) Å^2, and $u_{\rm D}^{2\,\rm (SCAP)}$ = 0.0332(3) Å^2. The SCAP results are not far from the VMC ones, with a better agreement in the prediction for the kinetic energies. The larger discrepancies in u_α^2 are mainly due to the simplification of the SCAP density of phonon states which corresponds to an Einstein solid (a delta function centered in $\Omega_{0,\alpha}$).

In a purely harmonic approach, and neglecting the slight differences in the lattice constants for **LiH** and **LiD**, the isotopic correction by substituting H by D would be in the Einstein frequency $\hbar\Omega_{0,\rm D}^{\rm h} = 1/\sqrt{2}\,\hbar\Omega_{0,\rm H}$. Then, using SCAP, $T_{\rm D}^{\rm h} = 1/\sqrt{2}\,T_{\rm H}$, and $u_{\rm D}^{2,\rm h} = 1/\sqrt{2}\,u_{\rm H}^2$. These values are $\hbar\Omega_{0,\rm D}^{\rm h}$ = 78 meV, $T_{\rm D}^{\rm h}$ = 59.4 meV, and $u_{\rm D}^{2,\rm h}$ = 0.052 Å^2. The significant differences between these

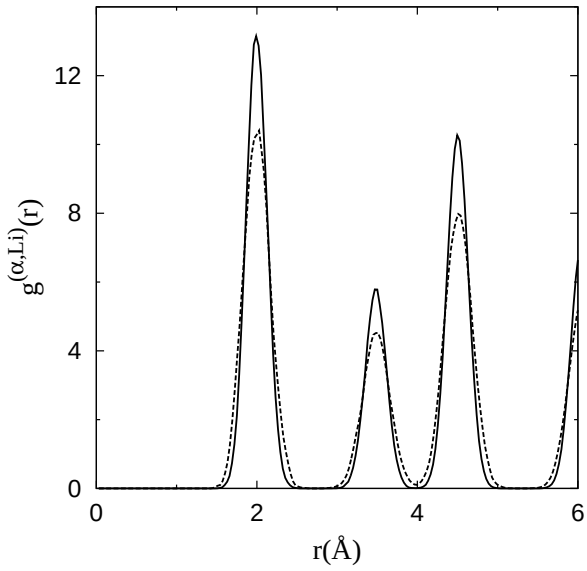

Figure 4.5: Radial distribution functions between Li and H or D; Li^+-H^- (dotted line) and Li^+-D^- (solid line) pairs.

results and the accurate ones of Table 4.3 shed light on the relevance of quantum effects in the ionic solids **LiH** and **LiD**.

Additional information on the spatial structure of the solid can be drawn from the two-body radial distribution functions $g^{(\alpha,\beta)}(r)$. In Fig.4.5, results for the radial distribution functions corresponding to the pairs of ions Li^+-H^- and Li^+-D^- are plotted. The position of the peaks coincide in **LiD** and **LiH** because the lattice structure is practically the same, but the peaks in lithium deuteride are slightly narrower because the displacements of the D^- ions around the equilibrium positions are smaller due to their larger mass.

In conclusion, the fully quantum treatment of the system has shown the existence of H-D isotopic effects, sizeable different from the corresponding ones expected from a merely harmonic estimation. New neutron scattering experiments, such as the recent ones reported in Ref. [119], would help enormously to check our theoretical predictions and to confirm once more the unavoidable quantum character of both **LiD** and **LiH**.

Chapter 5
Solid Ne at zero temperature

5.1 Introduction

Noble gases, like **He**, **Ne** and Xe, have been studied in great detail during the last decades, both experimentally and theoretically [130, 131]. Due to their simple electronic closed-shell structure, they appear to be affordable many-body systems where to carry out feasible quantum computations and test novel methods of calculation.

Although most of them are regarded as classical systems, quantum mechanical approaches are necessary to understand the nature of the lighter ones, **He** and **Ne**, in the low temperature regime. As it is well-known, **He** is the experimental and theoretical quantum many-body system for excellence. Unique features as Bose-Einstein condensation (BEC) and superfluidity (SF) are observed in liquid $^{\mathbf{4}}\mathbf{He}$, probably also SF in the solid phase but in a practically imperceptible fraction, due to the bosonic character of the atoms and small weight.

Even though this is not the case of **Ne**, the classical picture of frozen particles distributed on a crystalline lattice and attending to the equipartion principle is ruled out on it. Instead, a wider mean squared displacement, $\langle \mathbf{u^2} \rangle$, and a kinetic energy per particle, $\langle E_k \rangle$, greater than the predicted by Classical Mechanics are observed. A parameter which corroborates the quantum nature in solid **Ne** is the De Boer quantum parameter

$$\Lambda^* = \frac{h}{\sqrt{m\epsilon\sigma^2}} \quad , \tag{5.1}$$

which is proportional to the ratio between the thermal De Broglie wavelength

and the typical interatomic distance σ. This quantum indicator is equal to 0.54 for **Ne** (2.50 for ^{4}**He**), while for argon and other heavier noble gases where classical behaviour is expected it drops significantly to zero. In view of these facts, solid **Ne** must be classified into the category of quantum crystal (see Chapter 1), and consequently, fully quantum approaches are required to get comprehensive knowledge from it.

Experimental information on structural properties in condensed matter systems is obtained from the static structure factor function, S(**q**), which is directly measured from the output radiation in the elastic scattering experiments. This function can be estimated theoretically by means of QMC methods, since it is related to the Fourier transform of the radial distribution function, $g(r)$. In the case of bulk **Ne**, S(**q**) was measured long time ago in the liquid phase [133], however, only theoretical estimations of it are found for the solid. On the other hand, deep inelastic neutron scattering techniques (neutron Compton scattering -NCS-, for instance) provide reliable information about the collective motion of particles in condensed matter systems (dynamic structure factor -S(**q**,ω)- at high momentum transfer and momentum distribution -n(**p**)-). Apart from the variational approach, fully quatum–mechanics methods devised to simulate the real dynamics of physical processes are still under development [134, 135]. Despite of this, an exception is made with respect to the momentum distribution. As it has been proved [10], the QMC approach is able to provide trustworthy estimations of n(**p**) in the quantum system of interest through a Fourier transform of the one–body density matrix.

In the case of ^{4}**He** near the λ transition, it is well–known that the shape of n(**p**) is remarkably different from a Gaussian [30]. Therefore, it is of great interest to know to what extent the momentum distribution and kinetic energy of an intermediate quantum system like **Ne** is different from classical predictions. Several NCS experiments on liquid and solid **Ne** have been published to date [132, 136, 137, 141]; also systematic fully quantum calculations in the low temperature regime (4–30 K) have been carried out in both phases [138, 139, 140]. However, some discrepancies in the shape of the momentum distribution (strictly Gaussian or not) and the kinetic energy per particle, $\langle E_k \rangle$, are stated when theoretical results and experimental measurements for the solid phase are contrasted.

The first theoretical calculation of solid **Ne** was performed by Bernades in 1958; it was a variational calculation assuming uncorrelated single–particle wave functions. He obtained a kinetic energy per particle of 48.0 K [142]. However, the total ground–state energy calculated with this approach was found to be in poor agreement with experiment, and therefore, the introduction of many–particle correlations appeared to be necessary. Few years later, Nosanow and Shaw carried out a Hartree calculation (variational calculation with better uncorrelated single–particle wave functions) and estimated a kinetic energy of 42.8 K [143]: they obtained a better agreement with experiment, mainly for the ground–state energy and mean squared displacement from the equilibrium positions. Further on, Koehler also studied solid **Ne** but within the Self Consistent Phonon (SCP) formalism (pure harmonic approach) [144]; he obtained 42.6 K for $\langle E_k \rangle$ and other similar results to those of Nosanow and Shaw.

Nevertheless, most of the neutron scattering experiments in solid **Ne** have agreed in estimating a ground–state kinetic energy value around 49K [132, 140]. In principle, the discrepancy in $\langle E_k \rangle$ between the abovementioned early calculations and recent experiments could be explained in terms of anharmonic effects and/or inaccurate approximations. However, using the Path Integral Monte Carlo (PIMC) method, it has been shown that the kinetic energy per particle in solid neon at very low temperature is around 41 K [140, 141]. Moreover, two different modelizations of the interatomic interactions in **Ne** (L–J and HFD–C2 [145]) have been explored with PIMC in order to infer the dependence of the kinetic energy on them [140, 141]. However, while the initial discrepancy with experiments in the temperature range (4-20)K is maintained, the results obtained with the two different potentials turned out to be compatible.

Recently, Timms *et al.* [141] have carried out new experimental measures that seem to converge to the many–body theory predictions. The ground–state kinetic energy in Ref. [141] is determined by means of a linear extrapolation of the excess kinetic energy measured in the temperature range 4–20 K; they report $\langle E_k \rangle^{extrp}$=41(2) K as the zero temperature result.

In this chapter, we present a QMC study of the ground state of solid **Ne** with the DMC technique. The corresponding equation of state (EOS) at T=0K is assessed and several thermodynamic functions as the pressure and com-

pressibility are derived from it. The kinetic energy per particle at the equilibrium density is calculated and compared with previous PIMC and experimental predictions at zero temperature. It is shown that our estimation of $\langle E_k \rangle$ in solid **Ne** falls within the interval yielded by the zero temperature extrapolation of Ref. [141]. We have also tackled the problem of anharmonicity in solid **Ne** comparing the exact DMC results with the ones obtained through the Self Consistent Average Phonon (SCAP) and Self Consistent Phonon (SCP) theories [127, 32]. Complementarily, an structural study of the solid is presented; the pair–radial distribution function, Lindemann's ratio, kurtosis and density profile of the atoms around the sites have been calculated.

The schedule of the chapter is the following: in the first section we describe the modelization of the system and the trial wave function used for importance sampling; next, we present our ground–state results and compair them with the ones calculated with other approaches; finally, some concluding remarks are put forward.

5.2 The model

Solid bulk **Ne** is modeled assuming point-like atoms disposed in a fcc lattice and interacting via a radial pair–wise potential. The Hamiltonian of the system is

$$\mathrm{H} = -\frac{\hbar^2}{2m_{Ne}} \sum_{i}^{N} \nabla_i^2 + \sum_{i<j}^{N} V(r_{ij}) \tag{5.2}$$

where r_{ij} is the radial distance between the i and j labeled atoms, N the number of particles and m_{Ne} the atomic mass, equal to 20.173 a.m.u (this figure results from the average of the isotopic masses weighted by their corresponding abundances).

The potential chosen to model the interatomic interactions corresponds to the HFD–B form [146]. This potential reproduces within experimental error some of the macroscopic and microscopic properties of **Ne** over a wide range of temperature, and it turns out to be more realistic than the HFD–C2 [145] and L–J models at short distances. Explicitly,

$$V(r) = \epsilon \Theta(x) \tag{5.3}$$

where

$$\Theta(x) = A\exp\left(-\alpha x + \beta x^2\right) - F(x)\left(\frac{C_6}{x^6} + \frac{C_8}{x^8} + \frac{C_{10}}{x^{10}}\right)$$

with

$$F(x) = \begin{cases} \exp\left[-\left(\frac{D}{x} - 1\right)^2\right] & x < D \\ 1 & x \geq D \end{cases}$$

and

$$x = \frac{r}{r_m}\,.$$

The values of the parameters for the potential are

$A = 895717.95$	$\alpha = 13.86434671$
$D = 1.36$	$r_m = 3.091$ Å
$\beta = -0.12993822$	$\epsilon = 42.25$ K
$C_6 = 1.21317545$	$C_8 = 0.53222749$
$C_{10} = 0.24570703$	

It is known that, in the high pressure regime, the introduction of three-body terms in the effective potential of rare–gas solids is required to get an accurate description of them [140, 147, 148]. For instance, in solid Ar this limit is posed around 50 kbar. However, this fact does not affect the results presented here since our simulations have been carried out at densities corresponding to the 0–2 kbar pressure range.

Regarding the trial wave function chosen for importance sampling, Ψ_T, this corresponds to the Nosanow-Jastrow model,

$$\Psi_T\left(\mathbf{r_1}, \mathbf{r_2}, ..., \mathbf{r_N}\right) = \prod_{i\neq j}^{N} \mathrm{f}_2(r_{ij}) \prod_{i=1}^{N} \mathrm{g}_1(|\mathbf{r_i} - \mathbf{R_i}|) \tag{5.4}$$

with

$$\begin{aligned} \mathrm{f}_2(r) &= e^{-(\frac{b}{r})^c} \\ \mathrm{g}_1(r) &= e^{-\frac{1}{2}ar^2} \end{aligned} \tag{5.5}$$

and best parameter values $a = 6.5$ Å^{-2}, $b = 4.0$ Å and $c = 5$. The first factor in Ψ_T takes into account the pair correlations between particles, while the second introduces the crystalline lattice. Regarding the parameters of the simulation, the number of particles per box (where boundary conditions are applied) is N =256, the time step $\Delta\tau$= 2.7·10^{-4} K^{-1} and the critical walker population n_w= 260. These parameters have been chosen in order to ensure the correct asymptotic behaviour with respect to $\Delta\tau$ and n_w.

5.3 Results

5.3.1 DMC results

The equation of state of solid **Ne** at zero temperature is depicted in Fig.5.1. In this figure, the solid line corresponds to a polynomial fit, $e\left(\rho\right) = E\left(\rho\right)/N$,

$$e(\rho) = e_0 + a\left(\frac{\rho-\rho_0}{\rho_0}\right)^2 + b\left(\frac{\rho-\rho_0}{\rho_0}\right)^3 \tag{5.6}$$

to the DMC energies reported in Table 5.1 (solid points in the figure); energy tail corrections are included in the figures quoted in the table, in order to correct the finite–size errors introduced by the simulation box.

The parameters of the fit are a= 910(3) K, b= 826(20) K, e_0= -232.87(1)K and ρ_0= 0.04550(2)Å^{-3}, where e_0 and ρ_0 are the equilibrium energy and density, respectively.

It is worth noticing the excellent agreement between the equilibrium properties we have obtained and the experimental measurements e_0^{expt}= -232(1) K and ρ_0^{expt}= 0.044976(3) Å^{-3}, found in Refs. [149, 150].

Furthermore, once $e(\rho)$ is known it is straightforward to deduce the pressure, $P(\rho)$, and compressibility, $\kappa(\rho)$, through the set of equations

$$\begin{aligned} P(\rho) &= \rho^2 \frac{\partial e(\rho)}{\partial \rho} \\ \kappa(\rho) &= \frac{1}{\rho}\frac{\partial \rho}{\partial P} \quad . \end{aligned} \tag{5.7}$$

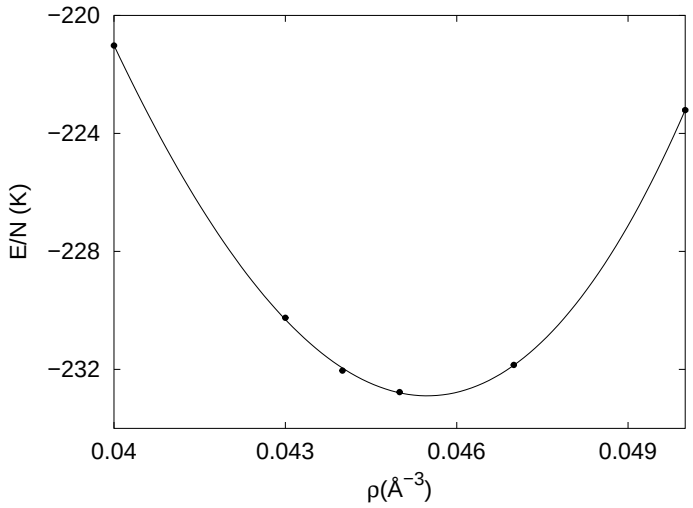

Figure 5.1: Total energy per particle in solid **Ne** as a function of density at absolute zero temperature. The solid line corresponds to a polynomial fit to the figures quoted in Table 5.1 (solid points).

The compressibility deduced at the equilibrium density is κ_0= 0.87(1)·10^{-9} Pa^{-1}, which is also in excellent agreement with the experimental value κ_0^{expt}= 0.89(2)·10^{-9} Pa^{-1} found in Ref. [150]. Complementarily, the dependence of the compressibility and pressure with the density are drawn in Figs.5.2 and 5.3, respectively.

An interesting magnitude in the study of homogeneous condensed systems is the spinodal density, ρ_S, i. e. the limit which the system is not thermodynamically allowed to cross maintaining a homogeneous phase. At this density, the system fulfills the relation $\partial P/\partial\rho$= 0, which is equivalent to an infinite compressibility and zero speed of sound; our prediction for this magnitude is ρ_S= 0.0350(2) $Å^{-3}$, which corresponds to a pressure $P(\rho_S)$= -1.10(5) kbar. In Ref. [151], Herrero presents a comprehensive study of solid **Ne** in the negative pressure regime by means of the PIMC method. The author modelizes the interatomic interactions with the L–J potential and calculates the pressure at the spinodal density and zero temperature, through a linear fit of the squared bulk modulus versus pressure; he yields $P(\rho_S)^{PIMC}$= -0.91 kbar,

ρ (Å^{-3})	E/N	V/N	T/N
0.040	$-221.03(2)$	$-251.37(6)$	$30.34(6)$
0.043	$-230.25(1)$	$-266.48(6)$	$36.23(6)$
0.044	$-232.04(1)$	$-270.61(10)$	$38.57(10)$
0.045	$-232.77(1)$	$-273.38(6)$	$40.61(6)$
0.047	$-231.85(2)$	$-277.02(10)$	$45.17(10)$
0.050	$-223.21(3)$	$-275.38(10)$	$52.17(10)$

Table 5.1: Total energy, potential energy and kinetic energy per particle of solid **Ne** at absolute zero. The potential and kinetic energies on the table are $pure$ estimations.

and ρ_S^{PIMC}= 0.0356 Å^{-3}. The discrepancy with our results in $P(\rho_S)$ may be explained in terms of the potential form: slight differences between the total energies deduced from the L–J and HFD–B potentials may be amplified carrying out successive derivatives with the density (pressure and bulk modulus) [140].

The pure estimator technique enables us to calculate exactly the expected ground–state value of any coordinate operator which does not commute with the Hamiltonian (see Chapter 3). By calculating the pure estimation of the potential energy, we can estimate in an unbiased way the kinetic energy per particle, $\langle E_k \rangle$, as the difference between the total and potential energies divided by N. The value we have obtained is $\langle E_k \rangle$= 41.68(6) K. Despite this estimation is more accurate than the zero temperature study reported by Timms *et al.* in Ref. [141], $\langle E_k \rangle^{extrp}$= 41(2) K, both results are compatible.

We have also carried out an structural exploration of the solid at the equilibrium density. In Fig.5.4, the radial pair–distribution function, $g(r)$, is depicted. This function is proportional to the probability of finding some particle at a certain distance r from another, and as it is observed, it exhibits a collection of peaks corresponding to the distances between crystalline positions in the fcc lattice.

One characteristic parameter in the study of quantum solids is the Lindemann's ratio,γ, which is defined as the ratio between the squared root of the mean squared displacement, $\langle \mathbf{u^2} \rangle$, and the smallest distance between neigh-

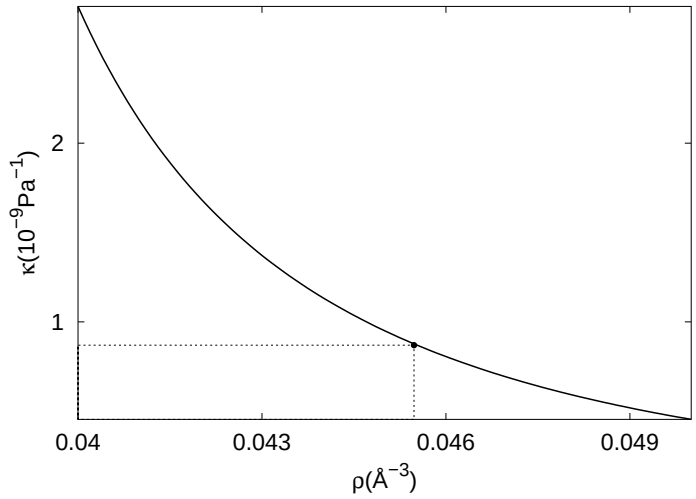

Figure 5.2: Compressibility of solid **Ne** as a function of density at T=0 K. The dot (•) indicates the equilibrium density where κ_0= 0.87·10^{-9} Pa^{-1}.

bouring positions in the perfect lattice. Our estimation of the Lindemann's ratio at the equilibrium density is γ_{Ne}= 0.088(2), which is significantly smaller than in ^{4}**He** (0.26) or $\mathbf{H_2}$ (0.18). The corresponding mean squared displacement, $\langle \mathbf{u^2_{Ne}} \rangle$, is equal to 0.077(1) Å^2. In Table 5.2 we also quote γ at some densities near the equilibrium; there, it is observed that γ reduces whenever the density is increased. This behaviour can be understood in terms of energy minimization: despite the gain in kinetic energy, derived from the increase in atomic location, the gain in cohesion when approaching to the perfect lattice turns out to be more advantageous.

In order to describe how the **Ne** atoms are distributed around the equilibrium positions, we have calculated the density profile function, $\mu(r)$, and kurtosis, ζ_Q. The density profile yields the probability of finding one particle at a distance $\in$ (r, r+dr) from any arbitrary site of the lattice. The mean squared displacement, $\langle \mathbf{u^2} \rangle$, then can be obtained as

$$\langle \mathbf{u^2} \rangle = 4\pi \int_0^\infty \mu(r) r^4 dr \quad . \tag{5.8}$$

In Figure 5.5, function $\mu(r)$ is plotted at the equilibrium density; the solid

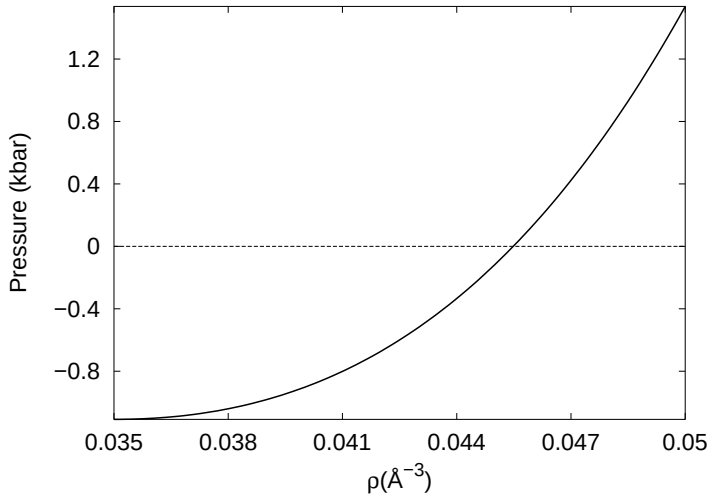

Figure 5.3: Pressure of solid **Ne** as a function of density at T=0K. The density range shown in the figure embraces from the spinodal density, $\rho_S = 0.035(2)$ Å^{-3}, to the maximum simulated one, 0.050Å^{-3}.

line in it corresponds to a Gaussian fit to our data (points). To check the reliability of this fit, we have assumed it instead of $\mu(r)$ in equation (5.8) and then recalculated $\langle \mathbf{u^2} \rangle$. The result obtained so is 0.079(1) Å^2, which perfectly agrees with the previous direct calculation 0.077(1) Å^2.

Once the shape of the atomic density profile is proved Gaussian, kurtosis may be computed whenever to decide atoms move isotropically or not. This magnitude is defined as

$$\zeta_{(ijk)} = \frac{\langle \mathbf{u^4}_{(ijk)} \rangle}{\langle \mathbf{u^2}_{(ijk)} \rangle^2} - 3 \quad , \tag{5.9}$$

where $\mathbf{u}_{(ijk)}$ are the projections of the vectors connecting each lattice site with its nearest particle along the (ijk) direction (cubic basis). It is easy to prove that when the atomic distribution around the lattice sites does not depend on the direction and is Gaussian, kurtosis equals zero. For the present system at the equilibrium density, we have obtained $\zeta_{(100)}$= 0.0078(63) and $\zeta_{(010)}$= 0.0062(59), which indeed imply isotropic motion of the **Ne** atoms around the equilibrium positions. Some other results concerning ζ_Q at densities near the equilibrium one are listed in Table 5.2.

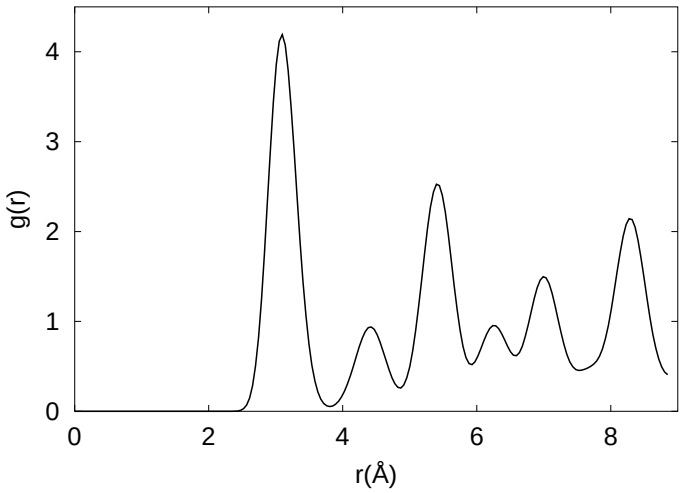

Figure 5.4: Pair–radial distribution function in solid **Ne** at the equilibrium density ρ_0. The location of the peaks corresponds to the neighbours in the fcc lattice.

5.3.2 SCAP results

It is known that the Self Consistent Phonon theory (SCP, [30]) is accurate for describing the main features of solids in the middle way between classical and quantum behaviour. This theory makes the assumption of particles being coupled harmonically with frequencies within a certain range and modes determined by the crystal symmetry and lattice parameter. A simplified version of this theory is the Self Consistent Average Phonon theory (SCAP, [127, 32]) which adopts the expressions of SCP theory but replacing the summation over the different vibrational frequencies by an averaged one (Einstein's frequency, Ω_0).

Despite this crude simplification, the agreement between experimental measurements and SCP/SCAP theories in solid **Ne** and other rare gases (Ar and Kr) is excellent when thermodynamic properties (isothermal bulk modulus, specific heat, etc.) are calculated within these approaches [32]. However, we would know to what extent harmonic assumptions in solid **Ne** are accurate enough for deriving microscopic properties of its ground state.

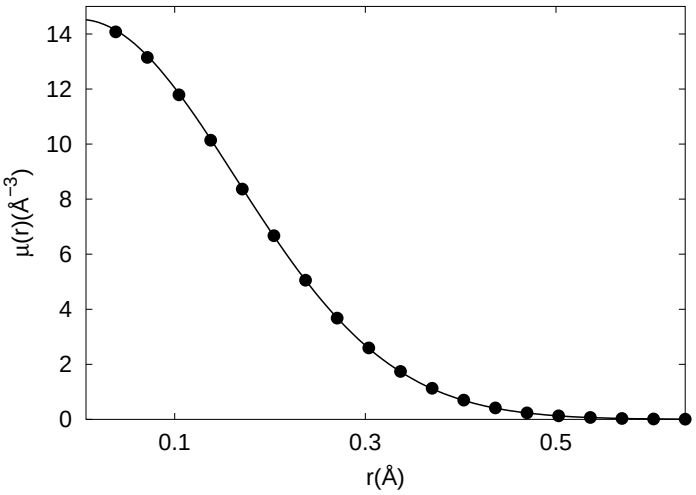

Figure 5.5: Density profile of the **Ne** atoms around the lattice positions. The solid line corresponds to a Gaussian fit to our data (points).

To partly answer this question and also get insight about possible anharmonic effects in solid **Ne**, we have calculated the corresponding kinetic energy and mean squared displacement assuming the SCAP approximation.

The formulas of interest are

$$\Omega_0^2 = \frac{1}{3mN} \left\langle \sum_{i=1}^{N} \nabla_i^2 V(\mathbf{r}_i) \right\rangle \ , \tag{5.10}$$

$$\begin{aligned} \langle \mathbf{u}^2 \rangle^{(\mathrm{SCAP})} &= \frac{3\hbar}{2m\Omega_0} \ , \\ \langle E_k \rangle^{(\mathrm{SCAP})} &= \frac{1}{2}\, m \langle \mathbf{u}^2 \rangle^{(\mathrm{SCAP})} \Omega_0^2 = \frac{3}{4}\hbar\Omega_0 \ , \end{aligned} \tag{5.11}$$

where $V(r)$ is the potential felt by a **Ne** atom and m its mass.

We first compute the exact Einstein's frequency, Ω_0, with the *pure* estimator technique within the DMC approach, and then calculate the value of expressions (5.11). The results we have obtained are, $\hbar\Omega_0$= 62.04(1) K,

ρ (Å^{-3})	γ	$\zeta_{(100)}$	$\zeta_{(010)}$
0.040	0.099(2)	0.017(12)	0.012(14)
0.043	0.092(2)	0.000(8)	−0.001(8)
0.044	0.091(2)	0.000(10)	0.000(10)
0.045	0.087(2)	−0.006(7)	−0.014(7)
0.047	0.086(2)	0.000(20)	0.000(10)
0.050	0.083(2)	0.000(10)	−0.010(10)

Table 5.2: Lindemman's ratio, γ, and kurtosis, ζ_Q of solid **Ne** at different densities close to equilibrium.

$\langle \mathbf{u}^2_{\mathrm{Ne}} \rangle^{SCAP}$= 0.058(3) Å^2, and $\langle E_k \rangle^{SCAP}$= 46.5(1) K. It is observed that the agreement between approximate SCAP and exact DMC results is not satisfactory, especially in the case of the mean squared displacement.

The existing discrepancies between these results could be explained in view of two different arguments: a) harmonic approximation in solid **Ne** is valid but the crude simplification made on the density of phonon states (delta function centered on Ω_0) is not accurate, and b) harmonic approximation is not valid in solid **Ne**.

As was mentioned in the introduction of this chapter, Koehler estimated within the Self Consistent Phonon framework the kinetic ground–state energy in solid **Ne**, obtaining $\langle E_k \rangle^{SCP}$= 42.6 K [144]. This result is reasonably compatible with our exact result and PIMC as well, however, this is not the case for the SCAP prediction. This fact, together with the Gaussian and isotropic distribution of the atoms around the lattice positions (characteristic of a particle in a harmonic field), make us incline towards option a) above.

Assuming only fully harmonic interactions among the particles in a solid, it is stated at zero temperature [121]

$$\langle \mathbf{u}^2 \rangle \langle E_k \rangle = \frac{9\hbar^2}{8m} \left(\int_0^\infty Z(\omega) \frac{1}{\omega} d\omega \right) \left(\int_0^\infty Z(\omega) \omega d\omega \right) \tag{5.12}$$

where $Z(\omega)$ is the density of phonon states of frequency ω (see equations 4.3 in Chapter 4). If $Z(\omega)$ in Eq.(5.12) is approximated by a delta function (SCAP), the product $\langle \mathbf{u}^2 \rangle \langle E_k \rangle$ equals the quantity $9\hbar^2/8m$. Then, if $\langle E_k \rangle$ is substituted by the exact value 41.68(6) K, $\langle \mathbf{u}^2 \rangle$ turns out to be ~ 0.065Å^2, which is still far

from the exact result 0.077(1)Å^2 but closer than the original SCAP estimation. One might expect to yield the exact $\langle \mathbf{u}^2 \rangle \langle E_k \rangle$ value once the integrals entering Eq.(5.12) were evaluated.

5.4 Comparison with previous results

In Fig.5.6 we have plotted some experimental and theoretical values of the excess kinetic energy in solid **Ne** in the temperature range (4–20)K. The excess kinetic energy, E_k^{exc}, corresponds to the part of the kinetic energy per particle which exceeds its classical prediction.

$$E_k^{exc} = \langle E_k \rangle - \frac{3}{2} k_B T \tag{5.13}$$

At zero temperature, the excess kinetic energy coincides with the zero point energy, so we have performed simple linear fits to the data in order to get the crossing point with the energy axis (dashed lines). The value of the extrapolated ground–state kinetic energy per particle corresponding to the experimental data found in Ref. [132] and Ref. [141], are 49.1(2.8) K and 41(2) K, respectively. As it is observed in the figure, PIMC results obtained with the HFD–C2 potential [140] (filled triangles) turn out to be compatible only with data found in Ref [141].

In view of these and the previously presented results concerning the kinetic energy per particle in solid **Ne**, it can be asserted that:
- our DMC estimation is compatible with previous PIMC results and experimental data found in Ref. [141], but not with previous experimental data found in Ref. [132]
- it is corroborated that no critical dependence of the ground–state kinetic energy per particle on the selected potential form exists, since PIMC extrapolations performed with the L–J and HFD–C2 models are compatible with our DMC value obtained with the HFD–B potential.

For the sake of clarity we have not included in Fig.5.6 the earliest calculations of Bernardes [142] and Nosanow *et al.* [143]. The first work corresponds to a variational calculation performed with an uncorrelated single–particle wave function; they obtained a kinetic energy of 48.0 K. The poor agreement between this result and ours is quite reasonable; first, because reliable estimations of the total ground–state energy at the variational level do not ensure

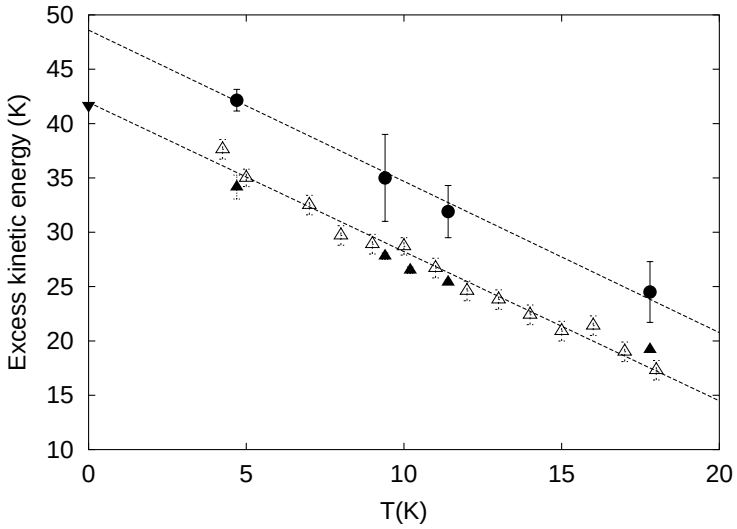

Figure 5.6: Experimental and theoretical values of the excess kinetic energy (K) in the temperature range (4–20)K. Dots (•) corresponds to experimental data of Ref. [132], empty triangles (△) to experimental data of Ref. [141], filled triangles (▲) to theoretical PIMC calculations with the HFD–C2 potential [140], and the ▼ symbol in the ordinate axis to our exact zero temperature calculation. The dashed lines (- - -) are linear fits to the experimental data in Refs. [132] and [141].

reliable estimations of any other magnitude, and second, the introduction of many–body correlations in the trial wave function model improves notably the variational description of a quantum system like this. On the other hand, the study carried out by Nosanow and Shaw [143] was performed at the Hartree level. They obtained $\langle E_k \rangle^{\mathrm{H}}$= 42.8 K, which surprisingly differs from our exact result only in a 3%.

It is also worthwhile mentioning the work carried out by Hansen [152] in which he performed a variational study of solid **Ne** with correlated wave functions. He estimated a total ground–state energy at the equilibrium density only 4 K upper than the present value, however, he did not quote the kinetic energy. In spite of this, our variational Monte Carlo (VMC) study of the system, previous to the DMC one, allows us to reproduce the total ground–

state energy deduced by Hansen ($\sim$ -228 K), and the corresponding kinetic energy of the atoms as well, $\langle E_k \rangle^{VMC}$= 37.0(5) K. In this case, it is evidenced that a fair agreement with the DMC total ground–state energy (2% error), does not imply necessarily a similar variational agreement in the kinetic energy (10% error) or any other magnitude.

5.5 Concluding remarks

We have studied the ground state of homogeneous solid **Ne** using the diffusion Monte Carlo (DMC) approach. This technique asymptotically provides the exact ground–state energy of the system as well as the expected values of other operators. Our results concerning the binding energy, equilibrium lattice parameter and equilibrium compressibility, agree notably with experimental data. Regarding the structural properties, the pair radial distribution function, g(r), density profile around the equilibrium positions, $\mu(r)$, Lindemann's ratio, γ, and kurtosis, ζ_Q, have been assessed at the equilibrium density ρ_0= 0.04550(2) Å^{-3}.

With the *pure* estimator technique we have computed the exact kinetic energy per particle at absolute zero, obtaining $\langle E_k \rangle$= 41.68(6) K. This result comes to be compatible with a very recent inelastic neutron scattering experiment [141] and previous PIMC calculations [140] in the temperature range (4–20)K. On the contrary, previous experimental data on this matter systematically underestimated the atomic zero–point energy few kelvins [132, 137].

Originally, the mentioned discrepancy between the experimental results and first theoretical calculations based on approximate methods [143, 144], was related to possible anharmonic effects. In order to detect anharmonicity in solid **Ne**, we have calculated the density profile around the crystalline positions and the kurtosis. We have found that the density profile perfectly fits to a Gaussian and that kurtosis vanishes in any of the three orthogonal directions of the cubic cell. In view of these results, we can conclude that the spatial distribution of any atom around its site is isotropic and Gaussian, exactly equal to the one which corresponds to a quantum particle moving within an external harmonic potential. This fact, added to the compatibility of our fully quantum calculation with the SCP one in Ref. [144], lead us to consider that the harmonic approach is sufficiently accurate to describe the ground–state

properties of solid **Ne**. We have also performed some calculations within the SCAP framework, which is a simplified version of the SCP theory. However, the results obtained in this case are not at all satisfactory.

All the theoretical results presented in this chapter have been obtained assuming the interparticle potential form HFD-B [146]. The excellent agreement between these and other fully quantum calculations assuming different models for the interatomic interactions (L–J and HFD–C2), corroborates the previously deduced conclusion that no critical dependence of $\langle E_k \rangle$ on the potential form exists [140, 141].

Chapter 6
Solid $^4\mathrm{He}$ at zero temperature

6.1 Introduction

Although helium is one of the simplest atoms in the Periodic Table of the Elements, its corresponding phase diagram is a rich and intriguing one which indefectibly accounts for its extraordinary quantum many-body nature. At T=0 K, and in equilibrium with its vapor pressure (P=0), helium is the only system which remains in the liquid phase, wherein it exhibits unique phenomenona like superfluidity (SF) and Bose–Einstein condensation (BEC). With a moderate pressure of P$\approx$25 bars, ^{4}**He** solidifies in the hexagonal closed–package structure (hcp) [153], and indeed, the face–centered cubic (fcc) [154] and body–centered cubic (bcc) [155, 156] crystalline forms can also be achieved at higher pressures and temperatures (Figure 6.1).

Solid helium has been from early in the beginning of the 40's up to present, the objective of continuous investigations, both experimental and theoretical. Just like it occurs in the liquid case, helium is the paradigm of quantum solids. This fact is a direct consequence of its large zero–point kinetic energy and Lindemann's ratio, both rendered by the light mass of the constituent atoms and the weak attractive interaction acting among them. It is worthwhile noticing that helium owns the largest De Boer parameter (see Eq.(1.6) and Table 1.1), Λ^* $\sim$2.5, among the whole chemical species.

Such evident quantum character of solid **He** has motivated continuous work focused on studying its main thermodynamic (heat capacity, bulk modulus, Debye temperature, etc.) [157, 158, 159] and microscopic aspects (momentum distribution, kinetic and binding energy, energy excitations, crysta-

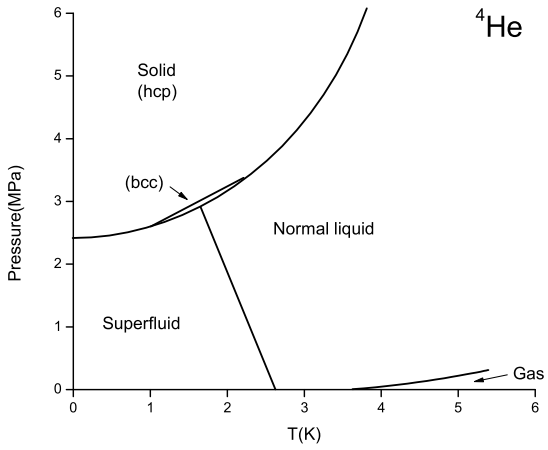

Figure 6.1: Schematic representation of the low temperature phase diagram of ^{4}**He**. Structure fcc, not included in the figure, is obtained above 120 MPa and 18 K.

lline defects -vacancies, impurities...-, etc.) [170, 171, 26, 172, 173].

But, in spite of being one of the most thoroughly investigated crystals, solid helium never stops marveling us. Recently, Kim and Chan [21, 22] have observed non-classical rotation of inertia (NCRI) in solid ^{4}**He** at temperatures below 0.2 K. In analogy to the superfluid case, where NCRI was first predicted by London 50 years ago [174] and few time later evidenced by Hess and Fairbank [175], this ascertainment would imply a supersolid phase where the crystalline order and the superfluid–like behaviour could coexist. The possibility of such state, which seemingly is counter to intuition, was first suggested by Andreev *et al.* in 1969 [33] and subsequently put under debate [176, 177, 178, 179]. However, experiments on this matter for the following 35 years were not successful. Kim and Chan's experiments have reopened a long-standing controversy which is forcing theorists to revise the generally accepted models concerning solid ^{4}**He** [180, 181, 182].

The aim of this chapter is twofold: first, a comprehensive and modern QMC study regarding the equation of state (EOS) and related properties of

solid ^{4}**He** at zero temperature, and second, an artificial model of external localization in liquid ^{4}**He** is investigated and jointly linked to a plausible mode of atomic diffusion within the crystalline structure.

In the first part of the chapter, the current level of accuracy in the description of solid ^{4}**He** is improved in two directions :
1) the semiempirical potential HFD-B(HE) [183] proposed by Aziz *et al.* in 1987, hereafter referred to Aziz II, is used to modelize the **He**–**He** atom interaction. This potential improves significantly the theoretical EOS of the liquid phase when it is compared with other potentials, as for instance the HFDHE2 [184] one, widely used over the past decade [57]
2) an accurate treatment of the finite–size effects is carried out in order to avoid the bias introduced by the simulation box. It is customarily assumed when calculating energy corrections (tails) in solids, that the radial pair–distribution function equals one beyond half the simulation box, despite it exhibits an ordered pattern therein. We show that such approximation in solid ^{4}**He** inevitably leads to an underestimation of the total energy of some tenths of K, and propose an improvement for estimating energy corrections.

Within this first part, also a new study of the energy properties of overpressurized liquid ^{4}**He**, that is, liquid helium in a metastable state, is presented and compared with the solid phase [185].

In the second part of the chapter, we intend to shed some light on the renewed controversy provoked by Kim and Chan's experiments on supersolids. As was pointed out in previous chapters, the diffusion Monte Carlo (DMC) method can provide exact estimations of the superfluid and condensate fractions in bosonic systems with affordably computational effort. Nevertheless, quantum solids within such framework are commonly described by non–symmetrized and non–translationally invariant trial wave functions. In consequence, atoms are not allowed to exchange and/or diffuse within the simulation box, and therefore, superfluid–like behaviour in crystals (if any) can not be studied. On the other hand, the extremely weak superfluid signal ($\sim$1%) and low phase–transition temperature ($\sim$0.1 mK) observed in the experiments, unfortunately overwhelm the computational efficiency of other full–quantum approaches (PIMC) which, contrarily to DMC, do not have to deal with trial wave functions.

In view of these limitations, we have investigated by means of the DMC technique an artificial model of localization in liquid **^{4}He**, where indeed, exchange symmetry and space delocalization are properly included in the trial wave function. In this model, atomic localization is imposed externally by means of a lattice of Gaussian traps. These traps are shaped in order to reproduce structural and microscopic properties of solid **^{4}He** at the same density. Under these conditions, superfluid–like behaviour is assessed in a small figure (ρ_s/ρ ∼2-4%).

6.2 EOS of solid ^{4}He at T=0

6.2.1 The model

The Hamiltonian describing the N-body system is assumed to include pair–wise interactions only, and the atoms are considered point–like. The **He**–**He** interaction is modelized with the radial Aziz II potential [183], expressed in the form

$$V(r) = \epsilon[A\exp\left(-\alpha x + \beta x^2\right) - F(x)\sum_{j=0}^{2}\left(C_{2j+6}/x^{2j+6}\right)] \tag{6.1}$$

where

$$F(x) = \begin{cases} \exp\left[-\left(\frac{D}{x}-1\right)^2\right] & x < D \\ 1 & x \geq D \end{cases}$$

with

$$x = \frac{r}{r_m}.$$

The values of the parameters for the Aziz II potential are:

$A = 1.844310 \cdot 10^5$	$\alpha = 10.43329537$
$D = 1.4826$	$r_m = 2.963$ Å
$\beta = -2.27965105$	$\epsilon = 10.948$ K
$C_6 = 1.36745214$	$C_8 = 0.42123807$
$C_{10} = 0.17473318$	

It has been proven [57] that this revised version of the HFDHE2 potential [184] produces a better description of the equation of state for liquid ^{4}He.

Regarding the form of the trial wave function, we have selected the usual Nosanow–Jastrow model (equation 6.2) owing that it conforms with a good variational description of the solid,

$$\Psi_{NJ}\left(\mathbf{r_1}, \mathbf{r_2}, ..., \mathbf{r_N}\right) = \prod_{i \neq j}^{N} \mathrm{f}_2(r_{ij}) \prod_{i=1}^{N} \mathrm{g}_1(|\mathbf{r_i} - \mathbf{R_i}|) \tag{6.2}$$

with

$$\begin{aligned} \mathrm{f}_2(r) &= e^{-(\frac{b}{r})^5} \\ \mathrm{g}_1(r) &= e^{-\frac{1}{2}ar^2}. \end{aligned} \tag{6.3}$$

The family of vectors $\{\mathbf{R_i}\}$ introduces the equilibrium positions of an hcp lattice at the desired density, which is the realistic one at T=0 [153, 159]. However, in many of the related theoretical works found in the literature the fcc lattice is adopted for the calculations [50, 187]. This fact is justified because, first, energy differences between the two structures are negligible up to the standard DMC accuracy level (the first and second shells of nearest neighbours of an atom are identical in both cases), and second, the fcc symmetry is the most convenient to treat with cartesian coordinates. In fact, we have checked the mentioned agreement between the total energy of both phases up to the present quadratic DMC accuracy level [189].

Since we have explored the system in a wide range of different densities (from 0.380 to 0.620 σ^{-3}, where σ = 2.556 Å), we have optimized the variational parameters contained in Ψ_{NJ} at some selected points, in order to provide a better description of the system. For example, the value of the parameters at the lowest simulated density are b = 1.12 σ and a = 5.7 σ^{-2}, while at the higher one are b = 1.18 σ and a = 8.0 σ^{-2}.

On the other hand, the number of particles, N, critical walker's population, n_w, and time step, τ, used in all the simulations are 180, 400 and 2.7·10^{-4} K^{-1}, respectively. They have been adjusted to eliminate any residual bias coming from them.

6.2.2 Size corrections to the energy

The description of an infinite system of interacting particles generally is deduced from the simulation of a finite number of particles enclosed within a box. The difference between the scale of the real and simulated systems can be overcome by enlarging the size of the simulated system so much as possible and applying periodic boundary conditions to it [190]. Even so, several corrections to the energies quoted directly from the simulation must be done if long–range correlations are present. Certainly, these corrections arise from the fact that the maximum distance involving correlations in the simulation coincides with the length–scale of the particle container. For instance, in the case of charged particle systems the well-known Ewald's sum formalism [190] is provided in order to extend the Coulomb interaction to infinite.

In the case of liquid ^{4}**He** the net contribution of the energy tails to the total energy per particle is quoted around some tenths of K [57]. The expressions of the potential and kinetic energy tail corrections, namely $\langle \Delta V \rangle^{tail}$ and $\langle \Delta T \rangle^{tail}$, assuming a certain cut–off correlation length, R_{max}, correspond to

$$\frac{\langle \Delta V \rangle^{tail}}{N} = 2\pi\rho \int_{R_{max}}^{\infty} g(r) V(r) r^2 dr \tag{6.4}$$

$$\frac{\langle \Delta T \rangle^{tail}}{N} = -4\pi D\rho \int_{R_{max}}^{\infty} g(r) \nabla^2 \ln \mathrm{f}_2(r) r^2 dr \tag{6.5}$$

where N, $D = \hbar^2/2m$ and ρ are the number, diffusion constant and density of particles, and $g(r)$, $V(r)$ and f_2 the radial pair–distribution function, pair potential and pair–correlation function, respectively.

In most of condensed matter simulations R_{max} is one half the length of the simulation box. In the case of liquids, the function $g(r)$ can be well–approximated to the unity in equations (6.4) and (6.5), and consequently, $\langle \Delta V \rangle^{tail}$ and $\langle \Delta T \rangle^{tail}$ turn out to be analytically accessible (standard tail correction -STC-).

Nevertheless, in the case of solids such approximation could result rather inaccurate owing that the pattern of the radial distribution function is still oscillating beyond the cut–off distance (p.e. see Figure 6.5). In view of this fact, and in order to get a description of the EOS in solid ^{4}**He** as precise as possible, we have estimated $\langle \Delta V \rangle^{tail}$ and $\langle \Delta T \rangle^{tail}$ variationally without assuming

$g(r) = 1$ beyond any limiting distance (variational tail correction -VTC-).

$$\langle \Delta E \rangle^{tail} = \langle \Delta T \rangle^{tail} + \langle \Delta V \rangle^{tail} = \langle E_T \rangle_{\infty}^{var} - \langle E_T \rangle_{N}^{var} \tag{6.6}$$

The subindexs in the above equation refer to the particle number, and the limit $N \to \infty$, indeed equivalent to the $R_{max} \to \infty$ one in equations (6.4) and (6.5), is reached through successive enlargements of the simulation box which actually results computationally affordable within the variational approach. In Figure 6.2 it is shown the asymptotic agreement between standard and variational energy tail corrections for an infinite system ($1/N \to 0$).

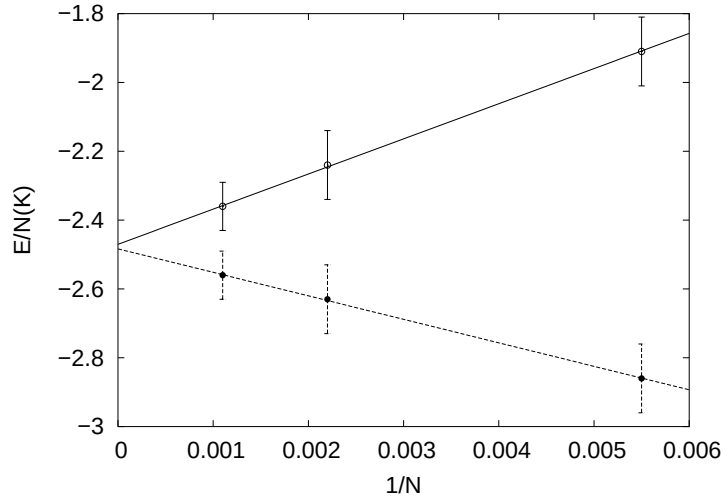

Figure 6.2: Variational total energy per particle in solid ^{4}**He** at $\rho = 0.540\ \sigma^{-3}$ as a function of $1/N$. The filled circles correspond to the total energy assuming STC energy corrections while the empty ones correspond to the total energy deduced directly from the simulation; both respective linear fits (dashed and solid lines) are coincident in the limit $N \to \infty$.

6.2.3 DMC results

In Figure 6.3 we have shown the EOS in solid ^{4}**He** at absolute zero, assuming both variational and standard energy tail corrections. As can be observed on it, theoretical estimations including VTC show a general excellent agreement with experiments and represent an appreciable improvement respect to the

STC case [158, 159] (see Table 6.1). The solid and dashed lines on the figure correspond to polynomial fits of the data in the common form (5.6); these fits are used to deduce the dependence of the pressure with the density (see Figure 6.4). Also in this case, an unusual accordance between our results and experiments is evidenced.

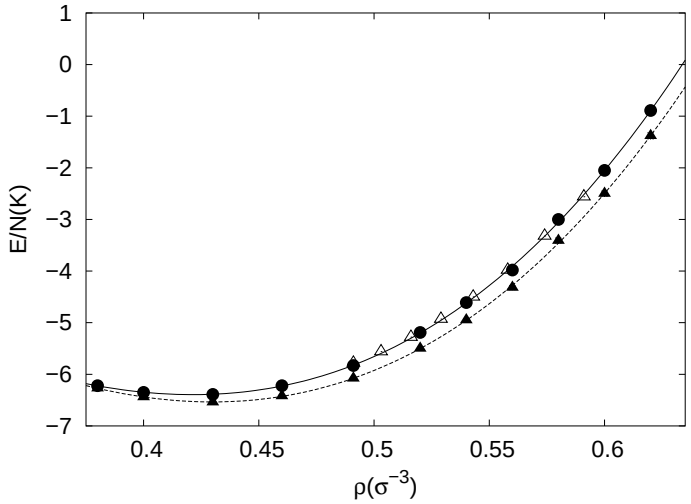

Figure 6.3: Ground–state energy per particle in solid ^{4}**He** as a function of the density. The empty triangles correspond to the experimental data from Ref. [158], while the filled circles and triangles correspond to our DMC results assuming VTC and STC corrections, respectively. The solid and dashed lines are polynomial fits in the form (5.6) to our data.

Once the EOS in solid and liquid ^{4}**He** are known, the respective freezing and melting densities can be computed easily with the double–tangent Maxwell construction; assuming for the liquid phase the equation of state from Ref. [57], which is also deduced with the radial pair–potential Aziz II, we obtain ρ_f = 0.437σ^{-3} and ρ_m = 0.481σ^{-3}. The melting pressure corresponding to such zero temperature phase transition is according to our study 27.3 atm. Our results agree notably with the experimental values measured by Grilly [191], who estimates $\rho_f^{expt} = 0.434\sigma^{-3}$ and $\rho_m^{expt} = 0.479\sigma^{-3}$ at a pressure equal to 25 atm. It is worthwhile noting the GFMC calculation carried out by Kalos *et al.* [187], which predicts the freezing and melting den-

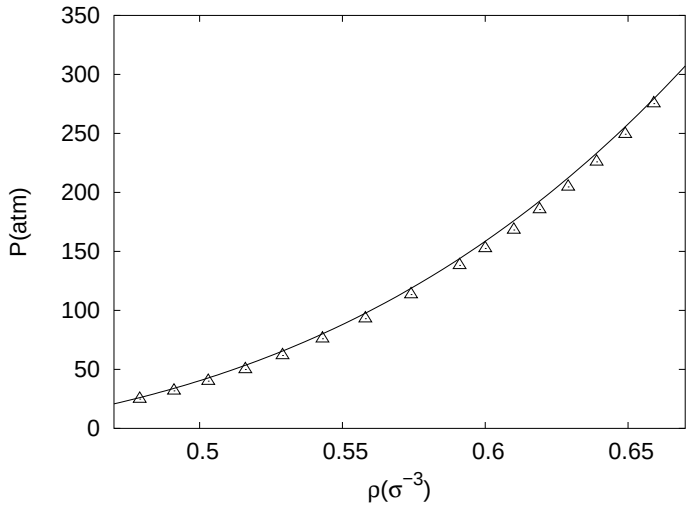

Figure 6.4: Zero temperature pressure in solid ^{4}**He** as a function of the density. The empty triangles correspond to the experimental data from Ref. [159] while the solid line is deduced from our data assuming VTC corrections.

sities of ^{4}**He** at $\rho_f = 0.438\sigma^{-3}$ and $\rho_m = 0.491\sigma^{-3}$ and pressure 26.7 atm; small discrepancies between these and our results are provided by the use of the HFDHE2 potential form instead of the Aziz II one. In a recent work, Ancilotto *et al.* [188] have studied the freezing of ^{4}**He** and its solid–liquid interface, using density functional theory and a L–J model for the atomic interactions. Concerning the liquid–solid phase transition, they have obtained $\rho_f = 0.437\sigma^{-3}$, $\rho_m = 0.490\sigma^{-3}$ and pressure 25.8 atm, which are values close to both our results and experimental measurements of Grilly [191].

With regard to the structural aspects, we have computed the Lindemann's ratio, $\gamma_{\rm He}$ (Table 6.2), and the radial distribution function, $g(r)$, and density profile around the sites, $\mu_{\rm He}$, at the given density $\rho = 0.480\sigma^{-3}$ (Figures 6.5 and 6.6, respectively). As it is observed in Table 6.2, the Lindemann's ratio of solid ^{4}**He** loosely exceeds value 0.20 within a wide density range; for instance, the equilibrium Lindemann's ratio corresponding to hydrogen, $\gamma_{\rm H}$ $\sim$0.18, and neon, $\gamma_{\rm Ne}$ $\sim$0.09, also are significantly smaller than the figures reported in this table. This uncommonly large Lindemann's ratio, and kinetic energy as well (for example, $\langle E_k \rangle^{expt} = 24.2(3)$ K at T=1.6 K [26]), converts helium in the quantum solid for excellence.

$\rho(\sigma^{-3})$	$E/N(K)$	$T/N(K)$	$V/N(K)$	$E^{expt}/N(K)$
0.445	−6.34(2)	21.23(5)	−27.57(5)	
0.460	−6.22(2)	22.48(3)	−28.70(3)	
0.470	−6.13(2)	23.24(3)	−29.37(3)	
0.480	−5.98(2)	24.08(3)	−30.06(3)	
0.491	−5.83(2)	24.98(3)	−30.81(3)	−5.78
0.500	−5.66(2)	25.71(3)	−31.37(3)	−5.62
0.520	−5.19(2)	27.50(4)	−32.69(4)	−5.18
0.540	−4.61(3)	29.22(6)	−33.83(6)	−4.60
0.560	−3.98(4)	30.98(4)	−34.96(1)	−3.90
0.580	−3.00(5)	32.98(5)	−35.89(1)	−3.07
0.600	−2.05(5)	34.60(5)	−36.65(1)	
0.610	−1.34(5)	35.83(5)	−37.17(1)	

Table 6.1: DMC total, kinetic and potential energies per particle in solid ^{4}He at T = 0. The data is calculated assuming VTC energy corrections. Experimental data from Ref.[158] are included in the last column; the figures shown therein, are obtained with a fourth order polynomial fit to the referenced experimental measurements (made the exception of the first one which is transported directly), in order to provide a direct comparison with our theoretical results (that is, equal densities in both cases).

$\rho(\sigma^{-3})$	0.480	0.491	0.500	0.520	0.540	0.560
γ_{He}	0.260(1)	0.257(1)	0.255(1)	0.249(1)	0.243	0.237(1)

Table 6.2: Lindemann's ratio in solid ^{4}**He** as a function of density at T=0 K. These values are calculated with the *pure* estimator technique.

In Figure 6.5 is clearly shown how function $g(r)$ still oscillates around the unity beyond half the length of the simulation box; in fact, this justifies our choice in calculating the energy tail corrections (VTC), which results in the addition of some tenths of K to the total energy per particle.

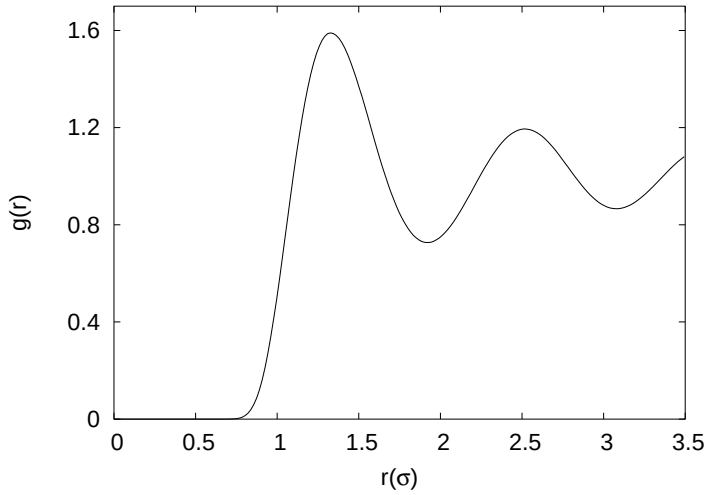

Figure 6.5: Radial pair–distribution function in solid ^{4}**He** at T = 0 and density ρ = 0.480(σ^{-3}).

Additionally, the averaged density profile of the particles around their respective lattice sites is shown in Figure 6.6, where a Gaussian fit to the data points is also plotted (solid line). As it is observed in the figure, such Gaussian fit reproduces correctly the local distribution of the particles around the equilibrium positions. In a recent PIMC work [83], Draeger *et al.* have detected a non–isotropic term in the Debye–Waller factor of solid ^{4}**He** at T$\sim$20K. The authors have assessed non–vanishing values of the kurtosis in a certain direction and at different densities; however, it is noted that these figures in

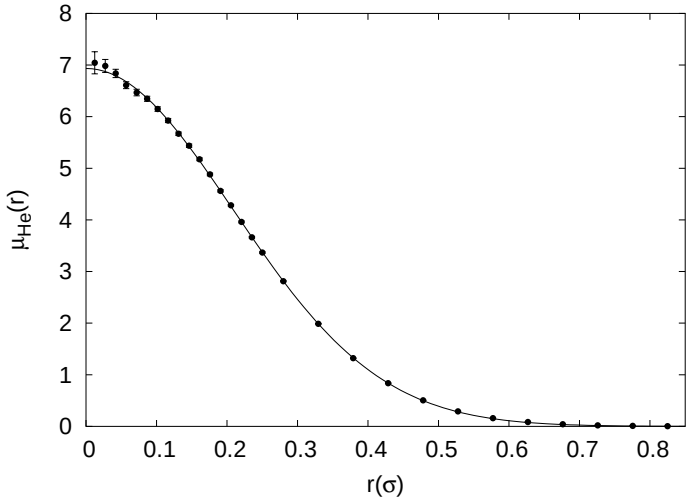

Figure 6.6: Density profile of the particles around their respective lattice sites in solid ^{4}He at T = 0 and density $\rho = 0.491(\sigma^{-3})$ (filled circles with error bars). The solid line corresponds to a Gaussian fit to the data points.

Ref. [83] are reported without including the corresponding statistical uncertainties. This PIMC result, contrarily to our DMC one, implies that the density distribution of the ^{4}He atoms around the equilibrium positions of the lattice is neither isotropic nor Gaussian. Possible causes of this disagreement could be explained in terms of the temperature, which is close to the corresponding zero Debye's temperature ($\theta_D \sim 25$ K), and/or the bias introduced by the one–body term in the Nosanow–Jastrow model, which indeed is a Gaussian.

6.2.4 Overpressurized liquid ^{4}He

Quantum fluids in metastable states are presently a research topic of fundamental interest from both the experimental and theoretical viewpoints [160]. The extremely low temperature achieved in liquid helium makes this liquid the purest in nature and therefore the optimal choice for observing homogeneous nucleation, which is an intrinsic property of the liquid. Caupin, Balibar and collaborators have studied profusely the negative pressure regime by focusing high–intensity ultrasound bursts in bulk helium [161, 162]. In liquid ^{4}He they have measured a negative pressure of -9.4 bar, only 0.2 bar above

the spinodal point predicted by microscopic theory [163, 164]. The same experimental team has used recently this acoustic technique to pressurize small quantities of liquid ^{4}**He** up to 160 bar at temperatures $0.05 < T < 1$K [165]. This pressure is the highest pressure ever realized in overpressurized liquid ^{4}**He** and is much larger than the liquid–solid equilibrium pressure, which at $T = 0$ K is 25.3 bar. Liquid ^{4}**He** in metastable states has also been obtained by immersing it in different porous media. Albergamo *et al.* [166], have carried out neutron–scattering experiments in a medium with 47 Å pore diameter filled with densities below the equilibrium density and negative pressures up to -5 bar. Using a different material, with 44 Å pore diameter, Pearce *et al.* [167] have reported neutron–scattering data in the high density regime observing a liquid phase up to ∼40 bar. Therefore, the confinement of helium in porous media makes feasible extensions of the pressure on both sides of the stable liquid phase. The nature of these two metastable regions presents a significant difference. At negative pressure, there exists an end point (spinodal point) where the speed of sound becomes zero, and it is thermodynamically forbidden to cross it maintaining a homogeneous liquid phase. On the contrary, such a point does not exist on the overpressurized side. At present, the theoretical knowledge of the metastable regime at negative pressures is rather complete with an overall agreement among quantum Monte Carlo, hypernetted chain based on Euler–Lagrange optimization, and density functional theory [160]. On the contrary, the pressurized liquid remains until now nearly unexplored.

In this subsection, we present diffusion Monte Carlo results for the overpressurized liquid phase up to 275 bar [185]. The DMC method is probably the best suited way to deal with this metastable regime since the physical phase of the system is controlled by the trial wave function used for importance sampling. It is worth noticing that overpressurized liquid ^{4}**He** in the studied density range remains superfluid, since the roton energy and fraction of condensate, both clear signatures of superfluidity, are non–vanishing in it.

The simulation of the liquid in its ground state is carried out by using a Jastrow factor, $\Psi_T(\mathbf{R}) = \prod_{i<j}^{N} \mathrm{f}_2(r_{ij})$, where f_2 is a model proposed by Reatto [45] and which incorporates nearly optimal short and medium range two–body correlations (see Eq.(1.15)).

The DMC energies corresponding to the overpressurized liquid are ac-

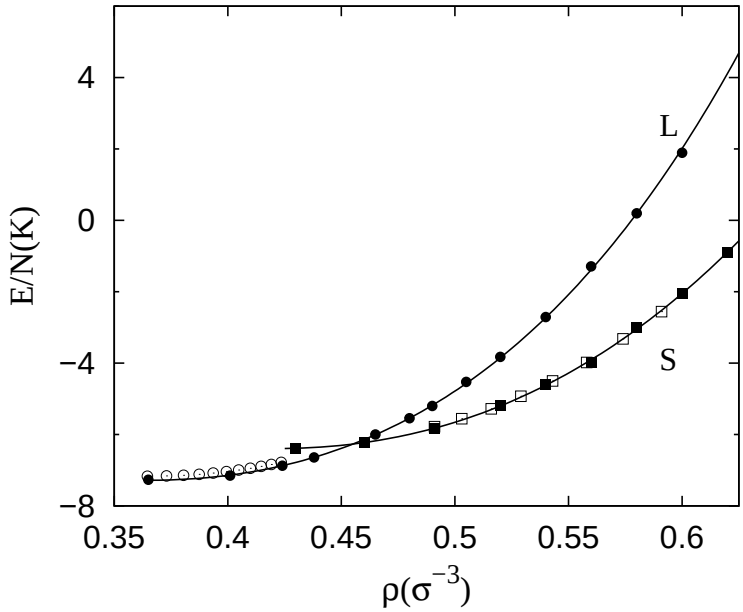

Figure 6.7: Energy per particle of liquid ^{4}**He** from the equilibrium density up to the highest density calculated $0.6\sigma^{-3}$ (solid circles). The solid line corresponds to the fit to the DMC energies using Eq.(6.7), and the open circles are experimental data in the stable regime from Ref. [168]. DMC results for the solid phase are shown as solid squares and compared with experimental data from Ref. [158] (open squares). The error bars of our data are smaller than the size of the symbols.

curately parametrized, from the spinodal point up to the highest densities calculated, by the analytical form

$$e(\rho) = e_0 + e_1\left(\frac{\rho}{\rho_c} - 1\right)\left[1 - \left(\frac{\rho}{\rho_c} - 1\right)\right] + b_3\left(\frac{\rho}{\rho_c} - 1\right)^3 + b_4\left(\frac{\rho}{\rho_c} - 1\right)^4, \qquad (6.7)$$

with $e = E/N$, and $\rho_c = 0.264\sigma^3$ the spinodal density. The rest of the parameters in Eq.(6.7) are $e_0 = -6.3884(40)$ K, $e_1 = -4.274(31)$ K, $b_3 = 1.532(12)$ K, and $b_4 = 1.433(24)$ K, the figures in parentheses being the statistical er-

rors. DMC results of the energies of the solid phase, presented in the previous subsection, are also included in Fig.6.7. Using the equation of state of both phases, their respective pressures are obtained from the thermodynamic definition $P(\rho) = \rho^2 \, (\partial e/\partial \rho)$. The results obtained, which are shown in Fig.6.8, reproduce accurately the experimental data [168] in the stable regime and predict a pressure $P \approx 275$ bar at the highest density evaluated, $\rho = 0.6\sigma^{-3}$. Our results are compared in the same figure with the analytic form suggested in Ref. [165], adjusted to Abraham's experimental data [169] (dashed line). Below the freezing point, both curves agree but they give significantly different values at higher densities; the difference amounts to $\sim$100 bar at $\rho = 0.6\sigma^{-3}$. As a matter of comparison, the figure also shows the pressure of the solid phase (deduced in the previous subsection, Fig.6.4).

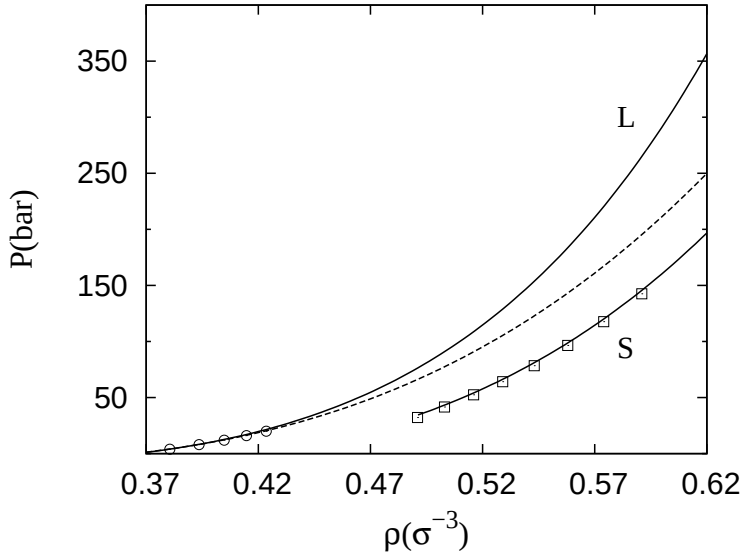

Figure 6.8: Pressure as a function of the density. The solid lines stand for the DMC results obtained from the equations of state of the liquid and solid phases shown in Fig.6.7. The dashed line is the extrapolation from experimental data [165, 169]; the symbols correspond to experimental data for the liquid [168] and solid [158] phases.

The present DMC calculation of the equation of state of overpressurized

liquid ^{4}He, is a new and accurate calculation posed in the interesting topic of quantum fluids in metastable regimes, and which turns out to be a motivating challenge for experimentalists.

6.3 Supersolid ^{4}He

As was pointed out in the introduction of this chapter, a renewed controversy on the possibility of superfluid–like behaviour in solid ^{4}He have been provoked by the recent experiments of Kim and Chan [21, 22]. This issue has been of great theoretical interest for many years [33, 176, 177]. However, on the one hand, any experimental evidence of such supersolid phase was inexistent until present, and on the other, a theoretical prediction of an upper bound to this superfluid fraction of about 10^{-4} had been generally accepted. The main result of Kim and Chan's experiments is that a non–classical rotation of inertia (NCRI) in bulk solid ^{4}He has been measured at temperatures below 0.2 K and in pressure range 25–65 bars. The observed superfluid fraction lies between 0.8 and 1.7%. The discussion is open on whether such experimental observation forcedly implies superfluid–like behaviour in solid helium or, contrarily to this, it just responds to the existence of some other effects present in the quantum crystal (point and line defects, incommensurability, slippage within the container, etc) [192, 193, 194].

The diffusion Monte Carlo method is able to calculate with affordable computational effort the zero temperature superfluid and condensate fractions in quantum liquids. In the case of the superfluid fraction, ρ_s/ρ, this is accomplished by computing the diffusion constant of the center of mass for an infinite imaginary time [91],

$$\frac{\rho_s}{\rho} = \lim_{\tau\to\infty} \frac{1}{6N\tau D_0} \langle (\mathbf{R}_{CM}(\tau) - \mathbf{R}_{CM}(0))^2 \rangle \tag{6.8}$$

where $\mathbf{R}_{CM}$ is the position of the center of mass of particles in the simulation box and D_0 the free diffusion constant of the particles $\hbar^2/2m_{He}$.

Attending to Eq.(6.8), it is evident that a certain diffusion of particles within the entire simulation volume is needed to register any superfluid signal. Nevertheless, the estimation of superfluidity in quantum solids (if any)

is systematically reduced to zero owing that commonly used trial wave functions describing the crystalline phase do not hold exchange–particle symmetry. However, the correct inclusion of symmetry is not expected to modify the energy results obtained within the Nosanow–Jastrow model since the exchange frequency has been estimated to be very small [52, 10].

In order to shed light on the possibility of a supersolid phase in ^{4}He, we have studied the ground–state properties of an ensemble of ^{4}He atoms moving on an external potential field, which is designed to localize particles around the positions of a certain crystalline lattice. In this way, instead of introducing the solid structure via the customary Nosanow–Jastrow trial wave function, Ψ_{NJ} (6.2), the same ordering conditions are achieved by imposing an external potential field (see Figure 6.9) and describing the system through a correctly symmetrized Jastrow factor, Ψ_J. Certainly, this model is not pretended to be a formal description of solids within the QMC formalism owing that the corresponding localization of the particles is obtained somehow artificially. However, scattering measures of the local order of the system would show signals nearly indistinguishable to the ones of a real solid.

6.3.1 The structured liquid model (SLM)

The Hamiltonian corresponding to the structured liquid model (SLM) is,

$$\mathrm{H} = -\frac{\hbar^2}{2m_{He}} \sum_{i=1}^{N} \nabla_i^2 + \sum_{i<j}^{N} V(r_{ij}) + \sum_{i=1}^{N} V_{ext}(\mathbf{r}_i) \tag{6.9}$$

where $V(r)$ is adopted in the Aziz II potential form and $V_{ext}(\mathbf{r})$ corresponds to the external confining potential. The explicit form of such potential reads,

$$V_{ext}(\mathbf{r}) = a \sum_{j=1}^{N} \exp\left[-b\left(\mathbf{R}_j - \mathbf{r}\right)^2\right] \tag{6.10}$$

where a and b are free parameters whose values are assigned to reproduce the main structural aspects of solid ^{4}He in the crystalline structure defined by the vectors $\{\mathbf{R}_i\}$. With some more detail, the selected lattice corresponds to the fcc symmetry at a density near the melting point, $\rho = 0.491\sigma^{-3}$; this option is justified since this is the most convenient symmetry to treat with cartesian

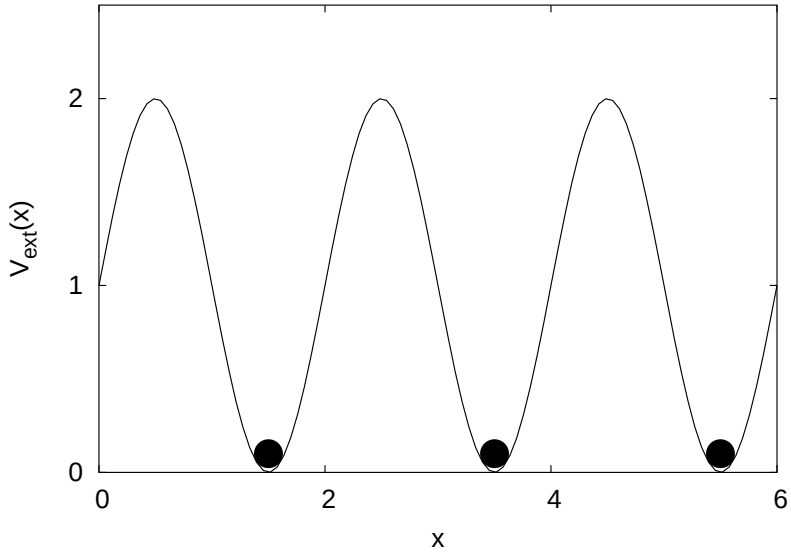

Figure 6.9: Schematic representation of a 1D ordered system imposed by a periodic external potential field (solid line). The filled circles represent the particles.

coordinates and which does not introduce any appreciable change respect to the proper one (hcp). On the other hand, the trial wave function, Ψ_J, corresponds to a Jastrow factor where the two–body correlation factors are adopted in the common McMillan form $\exp\left[-0.5\,(b/r)^5\right]$, being $b = 1.30\sigma$. Regarding the parameters of the simulation, the number of particles is $N = 108$, the critical population of walkers n_w = 420, and the time step $\Delta\tau$ = 2.5·10^{-4} K^{-1}, in order to reduce any possible bias coming from them to the level of statistical uncertainties.

Two important technical aspects concerning the simulation of the SLM must be noted: first, the equilibrium regime is costly reached due to the instabilities introduced by the deep constraining traps and the small time step adopted for an effective sampling (especially for the branching stage where the effect of the confining potential is fully taken into account -for reminding see section 2.3-), and second, the estimation of the superfluid fraction results in a very time consuming process due to the slow convergence towards the

V/N (K)	γ^{SLM}	ρ_s/ρ
$-31.81(10)$	$0.378(1)$	$0.27(5)$
$-32.37(12)$	$0.329(5)$	$0.13(3)$
$-32.78(10)$	$0.320(3)$	$0.08(2)$
$-33.47(10)$	$0.294(2)$	$0.05(2)$
$-33.77(10)$	$0.247(2)$	$0.02(1)$
$-35.54(10)$	$0.192(2)$	$0.0035(10)$

Table 6.3: Potential energy, Lindemann's ratio and superfluid fraction in the SLM at the given density $\rho = 0.491\sigma^{-3}$. The different points are obtained through varying the confining potential $V_{ext}(\mathbf{r})$.

asymptote in equation (6.8) (see Figure 6.10). These facts, together with the seek of a convenient pair of parameters a and b, make these simulations very demanding in computer time.

6.3.2 DMC results

In Table 6.3 we present the results concerning the interparticle potential energy, Lindemann's ratio and superfluid fraction in the proposed SLM in the conditions previously mentioned. The interparticle potential energy is computed by subtracting the entire effect of the external confining potential, $V_{ext}(\mathbf{r})$, to the total potential energy. This estimation results analogous to the one of the potential energy in the solid, which is found to be around -31.0 K per particle.

The Lindemann's ratio column in the same table, γ^{SLM}, is calculated in the following manner: from any position defined by the fcc lattice the nearest particle is found and the squared distance to it is computed to enter the common definition of γ (see equation 3.15); however, if once we have passed among all the crystalline sites any particle has not been included on γ, the corresponding summatory is readjusted by assigning the missgiven particle to the nearest site which owns a repeated nearest particle index and is not placed at a distance greater than one lattice parameter from it.

Certainly, these conditions on the evaluation of γ^{SLM} are imposed to avoid unwilling bias (double counting or missing of particles). In fact, we

have also considered the condition nearest site–to–particle and we have found that in the range 0.20–0.30 γ^{SLM} just varies to decrease on the hundredths; however, in this regime multiple occupation of a same site is observed with frequency ∼1-3%.

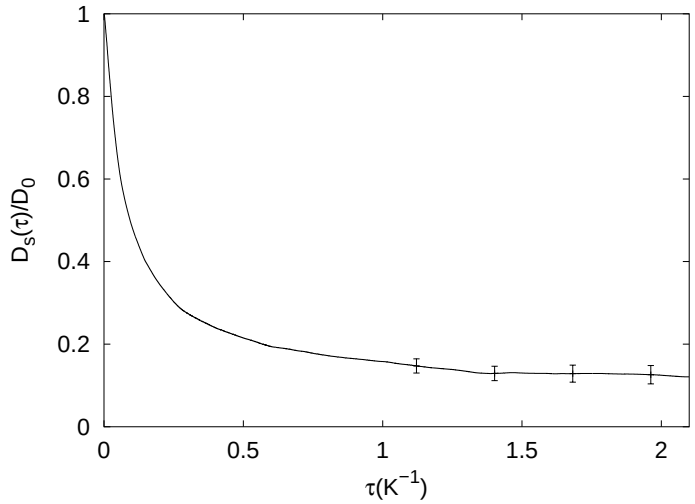

Figure 6.10: Diffusion of the center of mass in the SLM for an *infinite* imaginary time. In this case the evaluated superfluid fraction is ∼0.13 and the corresponding Lindemann's ratio γ^{SLM} = 0.329.

In the Nosanow–Jastrow model for solids (equation 6.2), previous considerations made on γ have non–sense since the atomic motion is bounded and the identification particle–to–site (or equivalently, site–to–particle) is always univoque; in spite of this, it is worthwhile noticing that in this model when the nearest site–to–particle is considered the ∼0.5% of the atoms are coincident with some another. Indeed, this occurs because the mean squared displacement in solid ^{4}**He** at the given density is unusually large (γ_{He} = 0.257).

The dependence of the superfluid fraction, ρ_s/ρ, with γ^{SLM} is also contained in Table 6.3 (see Figure 6.11), and can be fitted to a polynomial function of fourth order (dashed line). With this model, the prediction of the superfluid fraction in SLM when $\gamma^{SLM} = 0.257$ is found to be ∼2%. This particular point is selected because in the case of solid ^{4}**He** at zero temperature $\gamma_{\mathrm{He}} = 0.257$ at a density $0.491\sigma^{-3}$ (see Table 6.2) and it corresponds to a pressure of $\sim$ 34 atm, according to the EOS derived in a previous section. It must be noted that

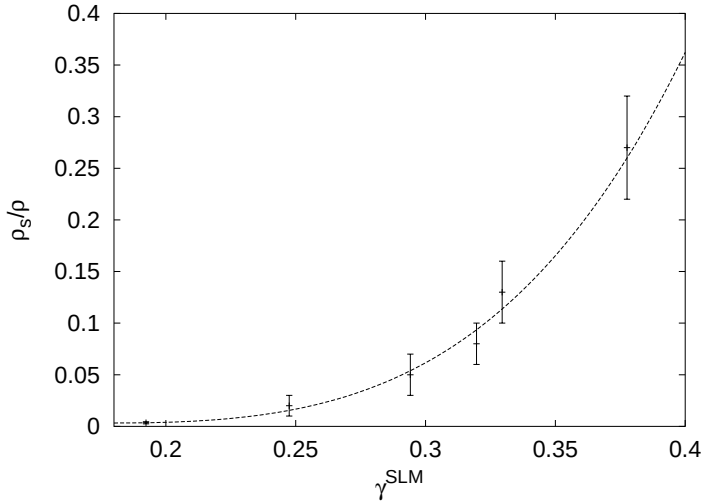

Figure 6.11: Dependence of the superfluid fraction, ρ_s/ρ, with the Lindemann's ratio in the SLM. The dashed line corresponds to a polynomial fit.

such pressure is on the range of Kim and Chan's experiment on solid bulk helium [22]. It is also worthwhile noticing that if the same dependence than in Figure 6.11 is drawn, but calculating γ^{SLM} just considering nearest site–to–particle (without redistributing particles to avoid double counting of a same site), the superfluid fraction deduced at 0.257 is $\sim$4%. Therefore, in order to overcome any reasonable criticism regarding the evaluation of γ^{SLM} and to be cautious, it can be asserted that the superfluid fraction in the SLM when the structural properties therein are very similar to those in ^{4}**He** at the same density, is some number between 2–4%.

In Figure 6.12 the radial distribution function, $g(r)$, corresponding to solid ^{4}**He** (solid line) and the SLM (dashed and dotted lines) at the studied density are compared. In the case of SLM, the lines correspond to two different choices of the confining potential, which yields respectively γ^{SLM} = 0.294 and 0.247; as it can be observed in the figure, an atomic ordering similar to that in the solid is achieved in the SLM case (periodic pattern).

Results for the static structure factor $S(k)$ (averaged in all directions) for both the Nosanow–Jastrow model and SLM, are shown in Fig.6.13. The two sharp peaks in the SLM case, centered in wave vectors corresponding to the fcc reciprocal lattice, are also clear signals of the attained crystalline order.

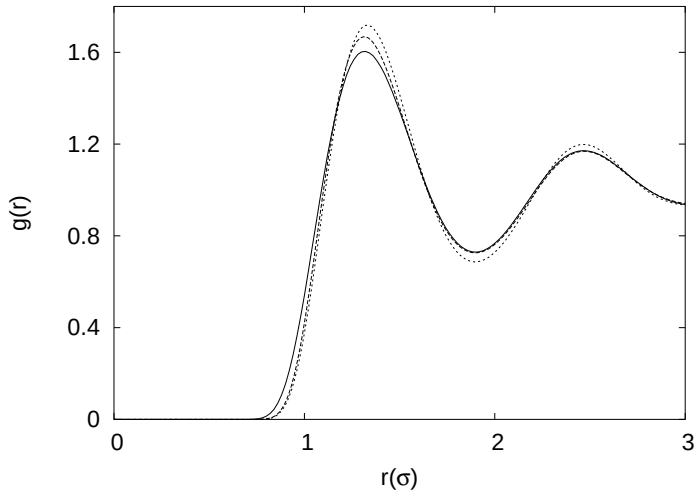

Figure 6.12: Radial pair–distribution function, $g(r)$, in solid ^{4}**He** at zero temperature and density $0.491\sigma^{-3}$ (solid line). The dashed and dotted lines correspond to the SLM at the same density and with γ^{SLM} = 0.294 and 0.247, respectively.

Once the main results concerning the proposed SLM are presented, a brief summary is required to fix the basic ideas to its respect :
a) while adopting a common Jastrow factor Ψ_J for describing an N–ensemble of ^{4}**He** atoms, an spatial order very similar to this in bulk solid (see Figures 6.12 and 6.13) is imposed by means of an adequate external potential (6.10).
b) the estimator γ^{SLM} is defined in analogy with the Lindemann's ratio for solids but with additional assumptions due to the capacity of the atoms to diffuse; its relation with the external confinement as well as the superfluid fraction, ρ_s/ρ, have been quoted (see Table 6.3). It is worthwhile noticing that if the external potential in the SLM is removed while considering the positions of the lattice, that is liquid ^{4}**He** with $\rho_s/\rho = 1.0$, $\gamma^{SLM} = 0.410$.
c) the superfluid fraction in the SLM corresponding to γ^{SLM} = 0.257 is some value between 2–4%; this estimation results quite compatible with Kim and Chan's measurements on bulk solid ^{4}**He** at pressures and temperature where $\gamma_{\rm He}$ is between 0.24 and 0.26.

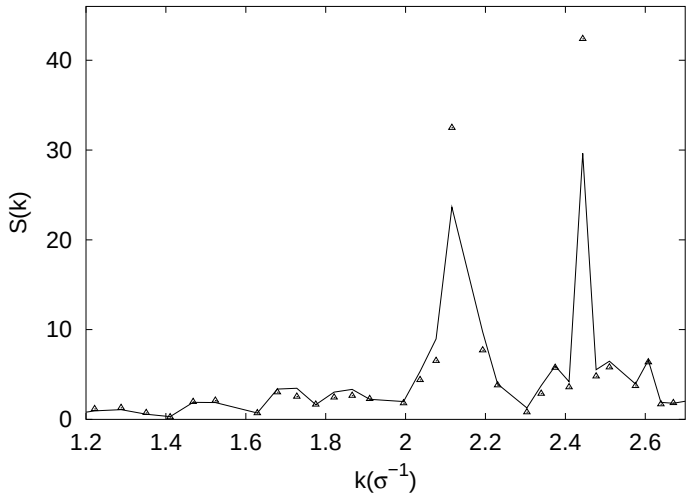

Figure 6.13: Static–structure factor corresponding to the SLM (solid line) with γ^{SLM} = 0.294, and to the Nosanow–Jastrow model (empty triangles), both at density $\rho = 0.491\sigma^{-3}$.

6.3.3 Discussion and speculations

In 1970 an argument provided by Chester [177], and based on a previous work of Reatto [195], proposed that a certain many–body state of interacting bosons could indeed show crystalline ordering and Bose–Einstein condensation simultaneously, though this did not insure superfluidity. In the same year [176], Leggett estimated in 10^{-4} the upper bound for the superfluid fraction in solid ^{4}**He** attending to some arguments of rotational symmetry and tunneling theory. One year later [178], Guyer estimated the superfluid transition temperature in bulk solid helium as T_s $\sim$0.1 mK, and also ρ_s/ρ $\sim 10^{-6}$. In the same decade, and based on Leggett's investigation, Saslow also estimated the superfluid fraction of interest, but assuming it as a function of some atomic localization parameter. He found that at zero temperature ρ_s/ρ in bulk ^{4}**He** should be between 0.05 and 0.2 [179].

The main point of agreement between all these ground–state investigations carried out along the 70's, is that atomic–exchange processes must be on the engine of any potential BEC or superfluid phenomenon occurring in bulk solid ^{4}**He** at temperatures below, at least, few tenths of mK. Indeed, once

this hypothesis is seriously assumed, the Path Integral Monte Carlo (PIMC) formalism appears to be a very suitable approach to study ^{4}**He** in such conditions, owing to its great capability in dealing with multiple–particle exchanges at finite temperature [10]. Nevertheless, it is an unfortunate fact that due to the extremely low temperature conditions and weak superfluid signal, the computational effort required for a rigorous sampling of the permutational space in the common PIMC strategy increases unfeasibly. In spite of providing good estimations of the total energy, the PIMC method results inefficient for estimating accurately the superfluid fraction in the cited conditions [196].

The main objective of the SLM study presented in the previous subsection, is to expose some plausible arguments in favour of superfluidity in bulk solid ^{4}**He** at zero temperature. As it has been mentioned, the DMC method enables us to evaluate accurately through equation (6.8) the superfluid fraction in an interacting system of bosons at zero temperature. In spite of this, and according to the present interests, one frustrating fact within this approach is that customary trial wave functions describing the solid phase are not correctly symmetrized, though the energetic predictions provided by them are excellent. With the SLM model we do not pretend to have a rigorous description of solid ^{4}**He**. However, it has been demonstrated that if a spatial ordering, very similar to this in the solid, is imposed externally on an ensemble of N ^{4}**He** atoms, properly described by a symmetrized trial wave function Ψ_J, the zero temperature estimation of the superfluid fraction on it is compatible with the recent experimental measurements of Kim and Chan.

Certainly, a more conclusive solution to the present problem concerning solid ^{4}**He** would involve the use of correctly symmetrized trial wave functions in the DMC evaluation of ρ_s/ρ. It is important to note the increasing complexity arising on this issue, since symmetrization must be fulfilled without loosing the accuracy of the spatial ordering and energetic description successfully achieved in the Nosanow–Jastrow model. An illustrative example of this is provided by the wave function,

$$\Psi_{\mathrm{S}}\left(\mathbf{r_1}, \mathbf{r_2}, ..., \mathbf{r_N}\right) = \Psi_J \prod_{i=1}^{N} \left(\sum_{j=1}^{N} \exp\left(-\frac{a}{2}|\mathbf{r_i} - \mathbf{R_j}|^2\right) \right) \tag{6.11}$$

which is correctly symmetrized. However, it yields an unrealistic diffusion

of the ^{4}He atoms and a poor variational estimation of the total energy [197]. In view of this, and some other failed attempts, we conjecture two different models of properly symmetrized trial wavefunction to check and implement within the DMC ansatz. The first model reads,

$$\Psi_{\mathrm{S1}}\left(\mathbf{r_1}, \mathbf{r_2}, ..., \mathbf{r_N}\right) = \Psi_J \exp\left(-\sum_i^N \xi\left(\mathbf{r_i}\right)\right) \tag{6.12}$$

where the function $\xi\left(\mathbf{r}\right)$ must be expanded in the set of plane–wave vectors corresponding to the appropriate reciprocal lattice,

$$\xi\left(\mathbf{r}\right) = \sum_{\{G\}} \xi_G \exp\left(-i\mathbf{G}\cdot\mathbf{r}\right). \tag{6.13}$$

In such a way, the explicit introduction of the lattice positions in the trial wave function is suppressed, while the periodicity of the one–body correlation factor is guaranteed (similar to Bloch formalism for electrons). This proposal is not new [54], but to our present state of knowledge it has never been applied to the case of solid ^{4}He within the DMC formalism.

A second model of symmetrized trial wave function for solids is

$$\Psi_{\mathrm{S2}}\left(\mathbf{r_1}, \mathbf{r_2}, ..., \mathbf{r_N}\right) = \Psi_J \exp\left(-\sum_{i,j}^N \Xi\left(\mathbf{r_i} - \mathbf{R_j}\right)\right), \tag{6.14}$$

where several considerations must be done on function $\Xi(\mathbf{r})$. If a Gaussian for the potential $\Xi(\mathbf{r})$ is proposed, one would realize that the corresponding numerical calculation would turn out to be dramatically instable and unreasonable. In fact, this is due to the linear increase of the Gaussian drift (first derivatives) with the distance. Intuitively, this is predicted by thinking on the trivial case of a particle held by a spring: the more stretched the spring is the greater the attractive force acting on the particle.

In principle, in any improved description of the solid phase it should happen that as far as a particle gets away from a certain lattice site the effective *attraction* to it should decrease in order to allow its diffusion. This is accomplished by imposing that the drift function associated to the proposed one–body correlation factor, $\nabla\Xi(\mathbf{r})$, tends to zero for increasing distances. Moreover, $\Xi(\mathbf{r})$ must also be maximum at the origin, decrease (or maintain constant, A) when r increases, and obviously have continuous and well behaved

first and second derivatives.

$$\begin{aligned} \lim_{r\to\infty} \Xi\left(r\right) &\to A \\ \lim_{r\to\infty} \nabla\Xi\left(r\right) &\to 0 \end{aligned} \tag{6.15}$$

The quality of $\Xi(\mathbf{r})$ would depend on its behaviour near the origin, which presumably may be $\lim_{r\to 0}\Xi\left(r\right) \to ar^2$ in analogy with Gaussians in the Nosanow–Jastrow model.

Future work devoted to the seek of new wave function models for quantum solids, holding both exchange–particle symmetry and spatial atomic location, appears to be challenging, since it would be required for a comprehensive and more accurate description of bosonic solids such as ^{4}He.

Chapter 7
General Conclusions

Many–body studies of bosonic quantum solids at zero temperature have been carried out with the variational Monte Carlo (VMC) and diffusion Monte Carlo (DMC) techniques. These fully quantum–mechanics approaches, provide upper bounds to the energy (VMC) and accurate estimations of the energy and structural properties (DMC) of quantum systems. The relevance of quantum effects and dimensionality of the investigated systems (**Ne**, **LiH**, **LiD**, $\mathbf{H_2}$, $\mathbf{D_2}$ and $^4\mathbf{He}$) are assorted. Next on, we present the main conclusions reported in this thesis.

1) Two–dimensional p–$\mathbf{H_2}$ at zero temperature (Chapter 3)

Exhaustive VMC and DMC studies have been carried out in 2D p–$\mathbf{H_2}$ at zero temperature. A detailed physical description of the system on the cited conditions and based on microscopic theory is quoted; our calculations agree satisfactorily with extrapolated PIMC results recently reported [81]. On the other hand, any possible conjecture about superfluid–like behaviour on such system is rigorously rejected. In fact, the EOS corresponding to the solid and liquid phases have been calculated using DMC and it has been concluded that the solid phase is the stable one for any possible density. The reduction of dimensionality in molecular hydrogen is not enough to induce its melting because, in spite of the light weight of a single molecule, the collective interactions provided by the inter–molecular potential is still dominant.

Moreover, the rate of particle–exchange processes in the ground state of solid 2D p–$\mathbf{H_2}$ is quantified at the variational level ($\sim$0.7% in the most

favourable case). The conclusion is that exchanges between molecules on such system are very unlikely to occur, so then, they can be neglected on practice.

2) p–$\mathbf{H_2}$ with alkali impurities (Chapter 3)

Based on the idea suggested by Gordillo and Ceperley [78], the zero temperature behaviour of a N–ensemble of p–$\mathbf{H_2}$ molecules with alkali impurities (Rb and Na) has been investigated. Due to the weak interaction between the p–$\mathbf{H_2}$ molecules and the alkali atoms, and also because the substrate induces an important effect of excluded surface, it has been assessed that in this strictly two–dimensional model the stable phase of the hydrogen molecules is the liquid one. Some improvements respect to previous works have been included in the calculations; these consist in using somehow more rigorous potentials to modelize the interactions of interest as well as in adopting other suitable and more realistic substrates (alkali lattices).

The main results quoted in the Rb–$\mathbf{H_2}$ case are a superfluid fraction, ρ_s/ρ, around the 8% and a fraction of condensate near the 3%. However, in the Na–$\mathbf{H_2}$ case a higher superfluid density is obtained, $\sim$30%, while the condensate fraction is very similar ($\sim$2%). The difference between the superfluid fraction calculated in the two cases is explained in terms of the crossed alkali–$\mathbf{H_2}$ interaction: since the core of the interaction, σ, is less repulsive in the Na case, a higher concentration of the hydrogen molecules and also a greater diffusion of them on the surface are allowed. Both facts result favourable to superfluidity. On the other hand, the condensate fractions are very similar and almost vanishing because the translational invariance in any of the two systems is practically suppressed by the presence of the substrate. The study concerning the p–$\mathbf{H_2}$ molecules with Na impurities, results specially motivating for the relatively high value of the superfluid fraction. However, the critical dependence of the results on the adopted alkali–hydrogen potential form, puts in evidence the need of more involved and accurate models to describe them.

3) Two–dimensional o–$\mathrm{D_2}$ at zero temperature (Chapter 3)

Analogously to the previous study in the p–$\mathbf{H_2}$ system, a ground–state investigation of 2D o–$\mathbf{D_2}$ has been carried out. The main objective of this study is

to provide a detailed description of the two–dimensional system while emphasizing the isotopic effects appearing on p–$\mathbf{H_2}$. Some of these isotopic effects are, an increase of the equilibrium density ($\sim 16\%$), decrease of the total energy ($\sim 80\%$), and decrease of the Lindemann's ratio ($\sim 20\%$), respect to the p–$\mathbf{H_2}$ case.

4) Ground–state properties of LiH (Chapter 4)

A variational Monte Carlo study of the ground–state properties of **LiH** is presented together with some recent neutron scattering experiments carried out by D. Colognesi and M. Zoppi on TOSCA–II (IINS) [119]. These new and highly accurate measurements on the dynamics of the H^- ion in **LiH**, are in a semi–quantitative fair agreement with the previous measurements of Dyck and Jex [109], though the main discrepancies are localized on the regimes 65 meV $< \hbar\omega <$ 90 meV (translational optical regime) and 112 meV $< \hbar\omega <$ 145 meV (longitudinal optical regime). Such differences are suggested to be founded in anharmonicity. The main objectives of this jointly experimental and theoretical study is to provide a detailed description of the quantum nature of the H^- ion, and also, to shed some more light on the possible issue of anharmonicity in solid **LiH**.

Basically, three quantum magnitudes concerning the dynamical aspects of the H^- ion have been measured experimentally and calculated within the VMC approach, namely the kinetic energy, $\langle T_H \rangle$, mean squared displacement,$\langle \mathbf{u}_H^2 \rangle$, and Einstein frequency, $\hbar\Omega_{0,H}$. The agreement between theory and experiment in the kinetic energy and Einstein frequency is excellent ($\langle T_H \rangle^{VMC} = 84(1)$meV, $\langle T_H \rangle^{IINS} = 80(1)$meV, $\hbar\Omega_{0,H}^{VMC} = 110.3(5)$meV and $\hbar\Omega_{0,H}^{IINS} = 109.2(9)$meV), while in the mean squared displacement this is rather modest ($\langle \mathbf{u}_H^2 \rangle^{VMC} = 0.074(2)$Å^2 and $\langle \mathbf{u}_H^2 \rangle^{IINS} = 0.062(1)$Å^2). The overall agreement, however, must be considered notable though the VMC approach is not an exact but approximate one.

Moreover, the same quantities have been quoted also attending to the SCAP theory [127, 32], which is a simplified version of the SCP theory and therefore relies on basic harmonic assumptions. The kinetic energy obtained so turns out to be compatible with the ones above mentioned, however $\langle \mathbf{u}_H^2 \rangle^{SCAP}$ is estimated below its experimental and variational counterparts

($\langle \mathbf{u}_{\mathrm{H}}^2 \rangle^{\mathrm{SCAP-VMC}} = 0.0564(3)\text{Å}^2$ and $\langle \mathbf{u}_{\mathrm{H}}^2 \rangle^{\mathrm{SCAP-IINS}} = 0.0570(5)\text{Å}^2$). This last discrepancy is straightforwardly understood because the evaluation of the mean squared displacement demands special accuracy on the shape of the density of phonon states (DoPS -see Eq. 4.3-), which is crudely approximated within the SCAP approach.

Regarding the possible anharmonic effects in **LiH**, a VMC study has been carried out on the solid phase but using harmonic expansions of the potential functions instead of the proper ones. In such a case, just the distances from each particle to its corresponding equilibrium position must be taken into account to compute the total energy (equivalent to a N–ensemble of decoupled oscillators). The numbers obtained so are identical to the ones yielded previously in the customary manner. This fact together with the acceptable description got in the SCAP scenario drive us to affirm that anharmonic effects in solid **LiH** result negligible, in spite of the large Lindemann's ratio ($\sim$0.13) and kinetic energy of the H^- ions therein.

5) Ground–state properties of LiD (Chapter 4)

An equivalent VMC study to that on **LiH** has been carried out on **LiD**, though without contrasting with any experimental measurement. The same dynamical quantum aspects, namely $\langle \mathbf{u}_{\mathrm{D}}^2 \rangle$, $\langle T_{\mathrm{D}} \rangle$ and $\hbar\Omega_{0,\mathrm{D}}$, have been assessed in the case of the D^- ion. The proposed targets of this study are to provide a thorough description of lithium deuteride as well as of the isotopic effects arising in **LiH**. Apart from the large Lindemann's ratios and kinetic energies of the ions, the great relevance of the quantum effects in solid **LiD** and **LiH** is manifestly put in evidence by the discrepancies coming up between our variational full-quantum results and the predictions from other semiclassical approaches (p.e. SCAP and the Debye model for solids).

6) Solid Ne at zero temperature (Chapter 5)

A DMC study of the ground state of solid **Ne** has been carried out. The corresponding energy properties (EOS, pressure and compressibility, etc.) have been deduced using the HFD–B [146] potential form, and subsequently compared with previous experimental data; the agreement between our theoreti-

cal results and experimental measurements of the thermodynamical properties is excellent. Furthermore, a detailed microscopic description of the internal structure (pair–radial distribution function, Lindemann's ratio, kurtosis and site density profile) is provided in order to complete this thorough description. Special emphasis is put on the estimation of the kinetic energy per particle which has been calculated exactly using the pure estimator technique for the potential energy.

One of the main objectives of this study apart from the pure intrinsic one, which is to yield a highly accurate characterization of such solid in the middle–way between the quantum and classical behaviour, is to shed some more light on the poor agreement among the experimental scattering data available to date [132, 137, 141], as well as in the discrepancies between most experimental results and full–quantum calculations [140].

The recently devised neutron Compton scattering (NCS) technique provides a direct access to the atomic momentum distribution in the quantum systems of interest; in turn, this can be used to deduce the excess kinetic energy at finite temperature, which actually is the magnitude to compare with simulations. Our exact estimation of the kinetic energy in solid **Ne** at zero temperature, $\langle E_k \rangle = 41.68(6)$K, is compatible with previous PIMC results [140] and the zero temperature extrapolation obtained from very recent scattering measurements carried out by Timms *et al.* [141], $\langle E_k \rangle^{extrp} = 41(2)$ K; however, this is not the case if the former experimental works are considered ($\langle E_k \rangle \sim 46$ K). Originally, this disagreement between full–quantum calculations and experiments on the kinetic energy was attributed to possible anharmonic effects in solid **Ne**, or critical dependence on the modelization of the potential.

According to our quoted results concerning the above mentioned issues, it can be concluded: a) in view of the fairly good agreement between our results obtained with the HFD–B potential, and other full–quantum calculations performed with the L–J and HFD–C2 forms [140, 137], it is corroborated that no critical dependence of the kinetic energy of solid **Ne** on the modelization of the interatomic interactions exists; b) full–harmonic approaches may describe accurately the unavoidable quantum nature of solid **Ne**, which at zero temperature does not exhibit anharmonic features in the atomic distribution around lattice sites.

7) Solid ^{4}He at zero temperature (Chapter 6)

A two–fold exhaustive study of the ground–state properties in ^{4}**He** has been carried out. The first part is purely descriptive and deals with the solid phase in the bulk configuration; through the DMC approach, the EOS and related energy properties are deduced with extreme accuracy due to a rigorous treatment of the potential energy tail contributions (quoted around 1K). The atomic interactions are modelized with the Aziz II potential form [183], which in the case of the liquid yields a notable improvement in the theoretical prediction of the EOS. In this way, an excellent agreement with experimental data is achieved [158, 159]. Also in this part, a microscopic analysis of the atomic structure is included for completeness (pair–radial distribution, Lindemann's ratio and density profile around the sites). Complementarily, a DMC calculation of the equation of state of liquid ^{4}**He** in the overpressurized regime is presented and compared with bulk solid. This new and accurate result appears to be challenging for experimental research.

The second part deals with an infinite system of ^{4}**He** atoms under the effect of an external confining field. Such external potential field is modelized in order to reproduce the crystalline structure of its solid counterpart (structured liquid model -SLM-). The main conclusions concerning the SLM are: a) a general solid–like ordering is obtained while the diffusion of the particles is not frustrated, b) superfluid–like behaviour is assessed and its relation with the strength of the external potential is explored, and c) in the specific case where the internal structure in the SLM is similar to that in solid ^{4}**He** under the conditions of Kim and Chan's experiments [22], the corresponding superfluid density is $\sim$2–4%; this value results reasonably compatible with the measurements reported by these authors in the already mentioned work.

Although the structured liquid model is not devised to be a reliable representation of solid ^{4}**He** because the crystalline order is imposed artificially via an external potential, our aim has been to provide some plausible arguments in favour of superfluidity in solid helium. As it has been pointed out, the DMC method is the most suitable one to estimate the superfluid fraction in the ground state of a N–body system, however the difficult problem of proper symmetrization in the common trial wave functions describing solids still remains. A more conclusive answer to such intriguing phenomenon in solid

helium would be yielded within the DMC formalism by some type of correctly symmetrized trial wave function, which as a requisite might provide the proper atomic ordering and energy properties.

Bibliography

[1] N.Metropolis, A.W.Rosenbluth, M.N.Rosenbluth, A.H.Teller, and E.Teller, *J.Chem.Phys.*, **21**, 1087 (1953)

[2] B. L. Hammond, W. A. Lester Jr. and P. J. Reynolds in *Monte Carlo Methods in Ab Initio Quantum Chemistry* (World Scientific, 1994).

[3] J. B. Anderson, *Rev. Comput. Chem.* **13**, 133 (1999).

[4] W. A. Lester in *Recent Advances in Quantum Monte Carlo Methods*, Recent Adv. in Comput. Chemistry, **2** (World Scientific, Singapore, 1997).

[5] *Microscopic Quantum Many–Body Theories and Their Applications*, ed. by J. Navarro and A. Polls (Springer, Berlin, 1998).

[6] L. de Broglie in *Recherches sur la theorie des quanta* (doctoral thesis, 1924).

[7] D. M. Ceperley and M. H. Kalos in *Monte Carlo Methods in Statistical Physics* (Springer, Berlin, 1979).

[8] M. H. Kalos, D. Levesque and L. Verlet, *Phys. Rev. A*, **9**, 2178 (1974).

[9] P. J. Reynolds, D. M. Ceperley, B. J. Alder, and W. A. Lester, *J.Chem.Phys.*, **77**, 5593 (1982).

[10] D. M. Ceperley, *Rev. Mod. Phys.*, **67**, 279 (1995).

[11] E. Sola, J. Casulleras and J. Boronat, *Journal of Low Temperature Physics* **138**, 1/2, 247 (2005).

[12] Y. Kwon and K. B. Whaley, *Journal of Low Temperature Physics* **138**, 1/2, 253 (2005).

[13] C. Kittel in *Introduction to Solid State Physics* (7th edition, Wiley 1996).

[14] N. W. Ashcroft and N. D. Mermin in *Solid State Physics* (Holt-Saunders 1976).

[15] R. K. Pathria in *Statistical Mechanics* (2nd Edition Butterworth-Heinemann 1996).

[16] J. J. Sakurai in *Modern Quantum Mechanics* (Addison-Wesley, 1985).

[17] J. de Boer, *Rep. Prog. Phys.*, **12**, 305 (1949).

[18] Alastair I. M. Rae in *Quantum Mechanics* (Institute of Physics Publishing Bristol and Philadelphia, 4th Ed. 2002).

[19] D. M. Ceperley and G. Jacucci, *Phys. Rev. Letts.* **58**, 1648 (1987).

[20] B. Bernu and D. Ceperley, in *Quantum Monte Carlo Methods in Physics and Chemistry*, eds, M. P. Nightingale and C. J. Umrigar, Kluwer (1999).

[21] E. Kim and M. H. W. Chan, *Nature (London)* **427**, 225 (2004).

[22] E. Kim and M. H. W. Chan, *Science* **305**, 1941 (2004).

[23] L. Boltzmann, *Wien. Ber.* **53**, (1866).

[24] J. C. Maxwell, *Philos. Trans. R. Soc. London* **157**, 49 (1867).

[25] H. R. Glyde, R. T. Azuah and W. G. Stirling, *Phys. Rev. B* **62**, 14337 (2000).

[26] S. O. Diallo, J. V. Pearce, R. T. Azuah and H. R. Glyde, *Phys. Rev. Lett.* **93**, 75301 (2004).

[27] R. T. Azuah, W. G. Stirling, H. R. Glyde and M. Boninsegni, *J. Low Temp. Phys.* **109**, 287 (1997).

[28] G. F. Reiter, J. Mayers and P. Platzman, *Phys. Rev. Lett.* **89**, 135505 (2002).

[29] P. Withlock and R. M. Panoff, *Can. J. Phys.* **65**, 1409 (1987).

[30] H. R. Glyde in *Excitations in Liquid and Solid Helium* (Clarendon Press, Oxford, 1994).

[31] *CRC Handbook of Chemistry and Physics*, 56th. edition (1976).

[32] A. Paskin, A. M. Llois de Kreiner, K. Shukla, D. O Welch and G. J. Dienes, *Phys. Rev. B*, **25, 2** (1982).

[33] A. F. Andreev and I. M. Lifshitz, *Sov. Phys. JETP* **29**, 1107 (1969).

[34] D. M. Ceperley and B. Bernu, *Phys. Rev. Letts.* **93**, 155303 (2004).

[35] P. Remeijer, S. C. Steel, R. Jochemsen, G. Frossati and J. M. Goodkind, *Low. Temp. Phys.* **23**, 447 (1997).

[36] D. I. Pusharov, *J. Phys. C: Solid State Phys.* **19**, 6873 (1986).

[37] T. A. G. Eberlein, R. Jones and P. R. Briddon, *Phys. Rev. Lett.* **90**, 225502 (2003).

[38] W. L. McMillan, *Phys. Rev.*, **138, 2A**, A442 (1965).

[39] W. M. C. Foulkes, L. Mitas, R. J. Needs and G. Rajagopal, *Rev. Mod. Phys.* **73**, 1 (2001).

[40] *Series on Advances in Quantum Many–Body Theory* **4**, ed. by E. Krotscheck and J. Navarro (World Cientific Publishing, 2002).

[41] Y. Alhassid, G. F. Bertsch, D. J. Dean and S. E. Koonin, *Phys. Rev. Lett.* **77**, 1444 (1996).

[42] R. B. Dingle, *Phil. Mag.*, **40**, 573 (1949).

[43] R. Jastrow, *Phys. Rev.*, **98**, 1479 (1955).

[44] E. Krotscheck, in *Microscopic Quantum Many-Body Theories and Their Applications*, ed. by J. Navarro and A. Polls (Springer, Berlin, 1998).

[45] L. Reatto, *Nucl. Phys.* **A 328**, 253 (1979).

[46] C. C. Chang and C. E. Campbell, *Phys. Rev. B* **15**, 4238 (1977).

[47] K. Schmidt, M. H. Kalos, M. A. Lee, and G. V. Chester, *Phys. Rev. Lett.*, **45**, 573 (1980).

[48] P. A. Whitlock, G. V. Chester, *Phys. Rev. B*, **35** vol. **10** (1987).

[49] L. H. Nosanow, *Phys. Rev. Lett.* **13**, 270 (1964).

[50] J. P. Hansen and D. Levesque, *Phys. Rev.*, **165**, 293 (1968)

[51] J. P. Hansen, *Phys. Letters*, **30A**, 214 (1969)

[52] D. Ceperley and G. V. Chester, *Phys. Rev. B*, **17, 3** 1070 (1978).

[53] S. Vitiello, K. Runge and M. H. Kalos, *Phys.Rev.Lett.* **60**, 1970 (1988).

[54] D. N. Lowy and C. Woo, *Phys. Rev. B* **13**, 3790 (1976).

[55] A. Nijenhuis and H. S. Wilf, in *Combinatorial Algorithms for Computers and Calculators*, 2nd ed. (Academic Press, 1978).

[56] S. A. Chin, *Phys. Rev. A* **42**, 6991 (1990).

[57] J. Boronat and J. Casulleras, *Phys. Rev. B* **49**, 8920 (1994).

[58] J. Casulleras and J. Boronat, *Phys. Rev. Lett.* **84**, 3121 (2000).

[59] R. Guardiola in *Microscopic Quantum Many-Body Theories and Their Applications*, ed. by J. Navarro and A. Polls (Springer, Berlin, 1998).

[60] W. Feller in *An Introduction to Probability Theory and its Applications*, **1** 3rd ed. (Willey, New York, 1968).

[61] W. H. Press, S. A. Teukolsky, W. T. Vetterling and B. P. Flannery, in *Numerical Recipes in Fortran 77, 2nd Ed.* (Cambridge University Press, 1992).

[62] G. S. Fishman in *Monte Carlo: Concepts, Algorithms and Applications* (Springer-Verlag New York 1996).

[63] K. S. Liu, M. H. Kalos and G. V. Chester, *Phys. Rev. A*, **10**, 303 (1974).

[64] P. J. Reynolds, R. N. Barnett, B. L. Hammond and W. A. Lester, Jr., *J. Stat. Phys.* **43**, 1017 (1986).

[65] K. J. Runge, *Phys. Rev. B* **45**, 7229 (1992).

[66] J. Casulleras and J. Boronat, *Phys. Rev. B* **52**, 3654 (1995).

[67] J. van Straaten, R. J. Wijngaarden and I. F. Silvera, *Phys. Rev. Lett.* **48**, 97 (1982).

[68] G. M. Seidel, H. J. Maris, F. I. B. Williams and J. G. Cardon, *Phys. Rev. Lett.* **56**, 2380 (1986).

[69] H. J. Maris, G. M. Seidel and F. I. B. Williams, *Phys. Rev. B* **36**, 6799 (1987).

[70] J. De Kinder, A. Bouwen and D. Schoemaker, *Phys. Rev. B* **52**, 15782 (1995).

[71] D. F. Brewer, J. C. N. Rajendra and A. L. Thomson, *J. Low Temp. Phys.* **101**, 317 (1995).

[72] M. Schindler, A. Dertinger, Y. Kondo and F. Pobell, *Phys. Rev. B* **53**, 11451 (1996).

[73] P. E. Sokol, R. T. Azuah, M. R. Gibbs and S. M. Bennington, *J. Low Temp. Phys.* **103**, 23 (1996).

[74] F. C. Liu, Y. M. Liu, and O. E. Vilches,*Phys. Rev. B*, **51**, 2848 (1995).

[75] M. C. Gordillo, J. Boronat, and J. Casulleras,*Phys. Rev. Lett.* **85**, 2348 (2000).

[76] S. Grevenev, B. Sartakov, J. P. Toennius and A. F. Vilesov, *Science* **289**, 1532 (2000).

[77] P. Sindzingre, D. M. Ceperley, and M. L. Klein,*Phys. Rev. Lett.* **67**, 1871 (1991).

[78] M. C. Gordillo and D. M. Ceperley,*Phys. Rev. Lett.* **79**, 3010 (1997).

[79] I. F. Silvera and V. V. Goldman,*J. Chem. Phys.* **69**, 4209 (1978).

[80] P. A. Whitlock, M. H. Kalos, G. V. Chester, and D. M. Ceperley, *Phys. Rev. B* **21**, 999 (1979).

[81] M. Boninsegni, *Phys. Rev. B* **70**, 193411 (2004).

[82] N. G. Kampen in *Stochastic Processes in Physics and Chemistry* (North–Holland, Amsterdam 1992).

[83] E. W. Draeger and D. M. Ceperley, *Phys. Rev. B* **61**, 12094 (2000).

[84] P. A. Whitlock, G. V. Chester, M. H. Kalos, *Phys. Rev. B* **38**, 2418 (1988).

[85] C. Cazorla and J. Boronat, *Journal of Low Temperature Physics* **134**, 1/2, 43 (2004).

[86] Gerald S. Leatherman and Renee D. Diehl,*Phys. Rev. B*, **53**, 4939 (1996).

[87] Gerald S. Leatherman, *Ph.D thesis* (Penn State University, 1996).

[88] Renee D. Diehl *(private communication).*

[89] L. W. Bruch, M. W. Cole and E. Zaremba in *Physical Adsorption:Forces and Phenomena* (Oxford Science Publications, 1997).

[90] F. Ancilotto, E. Cheng, M. W. Cole, and F. Toigo,*Z. Phys. B* **98**, 323 (1995).

[91] S. Zhang, N. Kawashima, J. Carlson, and J. E. Gubernatis, *Phys. Rev. Lett.* **74**, 1500 (1995).

[92] E. Cheng, G. Mistura, M. H. W. Chan, M. W. Cole, C. Carraro, W. F. Saam and F. Toigo, *Phys. Rev. Lett.* **70**, 1854 (1993).

[93] D. Ross, P. Taborek and J. E. Rutledge, *Phys. Rev. B* **58**, 4274 (1998).

[94] W. Shi, J. K. Johnson and M. W. Cole, *Phys. Rev. B* **68**, 125401 (2003).

[95] M. Boninsegni, *Phys. Rev. B* **70**, 125405 (2004).

[96] Ph. Avouris, D. Schmeisser and J. E. Demuth, *Phys. Rev. Lett.* **48**, 199 (1982).

[97] H. Wiechert, K. D. Kortmann and N. Stüsser, *Phys. Rev. B* **70**, 125410 (2004).

[98] W. M. Mueller, J. P. Blackledge, and G. G. Libowitz, *Metal Hydrides* (Academic Press, New York, 1968).

[99] E. Zintl and A. Harder, *Z. Phys. Chem. B* **14**, 265 (1931).

[100] R. S. Calder, W. Cochran, D. Griffiths, and R. D. Lowde, *J. Phys. Chem. Solids* **23**, 621 (1962).

[101] C. O. Rodriguez and K. Kunc, *J. Phys.; Condensed Matter* **1**, 1601 (1989).

[102] A. K. M. A. Islam, *Phys. Stat. Sol. B* **180**, 9 (1993).

[103] J. Van Kranendonk, *Solid Hydrogen* (Plenum Press, New York, 1983).

[104] F. A. Lindemann,*Phys. Z.* **11**, 609 (1911).

[105] J. M. Besson, G. Weill, G. Hamel, R. J. Nelmes, J. S. Loveday, and S. Hull, *Phys. Rev. B* **45**, 2613 (1992).

[106] A. C. Ho, R. C. Hanson, and A. Chizmeshya,*Phys. Rev. B* **55**, 14818 (1997).

[107] S. Lebèsgue, M. Alouani, B. Arnaud, and W. E. Pickett, *Europhys. Lett.* **63**, 562 (2003).

[108] J. L. Verble, J. L. Warren, and J. L. Yarnell, *Phys. Rev.* **168**, 980 (1968).

[109] W. Dyck and H. Jex, *J. Phys. C.: Solid State Phys.* **14**, 4193 (1981).

[110] Yu. A. Izyumov and N. A. Chernoplekov, *Neutron Spectroscopy* (Consultants Bureau, New York, 1994).

[111] M. G. Zemlianov, E. G. Brovman, N. A. Chernoplekov, and Yu. L. Shitikov, in *Inelastic Scattering of Neutrons*, vol. II, pg. 431 (IAEA, Vienna, 1965).

[112] A. R. Q. Hussain and M. J. Sangster *J. Phys. C.: Solid State Phys.* **19**, 3535 (1986).

[113] E. Haque and A. K. M. A. Islam, *Phys. Stat. Sol. B* **158**, 457 (1990).

[114] G. Roma, C. M. Bertoni, and S. Baroni, *Solid State Communications* **98** 203 (1996).

[115] B. Yates, G. H. Wostenholm, and J. L. Bingham, *J. Phys. C: Solid State Phys.* **7**, 1769 (1974).

[116] J. L. Anderson J. Nasise, K. Philipson, and F. E. Pretzel, *J. Phys. Chem. Solids* **31**, 613 (1970).

[117] D. C. Wallace, *Thermodynamics of Crystals* (J. Wiley, New York, 1972).

[118] D. Colognesi, M. Celli, F. Cilloco, R. J. Newport, S. F. Parker, V. Rossi-Albertini, F. Sacchetti, J. Tomkinson, and M. Zoppi, *Appl. Phys. A* **74** [Suppl. 1], 64 (2002).

[119] J. Boronat, C. Cazorla, D. Colognesi, and M. Zoppi *Phys. Rev. B* **69** , 174302 (2004).

[120] D. Colognesi, C. Andreani, and E. Degiorgi, *Phonon Density of States from a Crystal-analyzer Inverse-geometry Spectrometer: A study on Ordered Solid Hydrogen Sulfide and Hydrogen Chloride* (Journal of Neutron Research, 2003).

[121] V. F. Turchin, *Slow Neutrons* (Israel Program for Scientific Translations, Jerusalem, 1965).

[122] J. Hama and N. Kawakami, *Phys. Lett. A* **126**, 348 (1988).

[123] M. Born and K. Huang, *Dynamical Theory of Crystal Lattices* (Oxford Press, Oxford, 1954).

[124] S. Rosati and M. Viviani, in *First International Course on Condensed Matter*, edited by D. Prosperi *et al.* (World Scientific, Singapore, 1988)

[125] M. J. L. Sangster and R. M. Atwood, *J. Phys. C: Solid State Phys.* **11**, 1541 (1978).

[126] J. P. Vidal and G. Vidal-Valat, *Acta Cryst. B* **42**, 131 (1986).

[127] K. Shukla, A. Paskin, D. O. Welch, and G. J. Dienes, *Phys. Rev. B* **24**, 724 (1981).

[128] M. T. Dove *Introduction to Lattice Dynamics* (Cambridge University Press, Cambridge, 1993).

[129] C. Cazorla and J. Boronat, *Journal of Low Temperature Physics* **139**, 5/6, 645 (2005).

[130] J. P. Hansen and I. R. McDonald, *Theory of Simple Liquids* (Academic Press, New York, 1976).

[131] M. L. Klein and J. A. Venables, *Rare Gas Solids* (Academic Press, London, 1976).

[132] D. A. Peek, I. Fujita, M. C. Schmidt and R. O. Simmons, *Phys. Rev. B* **45**, 9680 (1992).

[133] L. A. de Graaf and B. Mozer, *J. Chem. Phys.* **55**, 4967 (1971).

[134] G. Voth, D. Chandler and V. H. Miller, *J. Chem. Phys.* **91**, 7749 (1989).

[135] J. Cao and G. Voth, *J. Chem. Phys.* **99**, 10070 (1993).

[136] D. A. Peek, M. C. Schmidt, I. Fujita and R. O. Simmons, *Phys. Rev. B* **45**, 9671 (1992).

[137] D. N. Timms, A. C. Evans, M. Boninsegni, D. M. Ceperley, J. Mayers and R. O. Simmons, *J. Phys: Condens. Matter* **8**, 6665 (1996).

[138] A. Cuccoli, A. Macchi, V. Tognetti and R. Vaia, *Phys. Rev. B* **47**, 14923 (1993).

[139] A. Cuccoli, A. Macchi, G. Pedrolli, V. Tognetti and R. Vaia, *Phys. Rev. B* **56**, 51 (1997).

[140] M. Neumann and M. Zoppi, *Phys. Rev. E* **65**, 031203 (2002).

[141] D. N. Timms, R. O. Simmons and J. Mayers, *Phys. Rev. B* **67**, 172301 (2003).

[142] N. Bernardes, *Phys. Rev.* **112**, 1534 (1958).

[143] L. H. Nosanow and G. L. Shaw, *Phys. Rev.* **128**, 546 (1962).

[144] T. R. Koehler, *Phys. Rev. Lett.* **17**, 89 (1966).

[145] R. A. Aziz, W. J. Meath and A. R. Allnatt, *Chem. Phys.* **79**, 295 (1983).

[146] R. A. Aziz and M. J. Slaman, *Chem. Phys.* **130**, 187 (1989).

[147] M. Grimsditch, P. Loubeyre and A. Polian, *Phys. Rev. B* **33**, 7192 (1986).

[148] V. F. Lotrich and K. Szalewicz, *Phys. Rev. Lett.* **79**, 1301 (1997).

[149] G. T. McConville, *J. Chem. Phys.* **60**, 4093 (1974).

[150] D. N. Batchelder, D. L. Losee and R. O. Simons, *Phys. Rev.* **162**, 767 (1967).

[151] C. P. Herrero, *Phys. Rev. B* **68**, 172104 (2003).

[152] J. P. Hansen, *Phys. Rev.* **172**, 919 (1968).

[153] W. H. Keesom and K. W. Taconis, *Physica* **5**, 161 (1938).

[154] J. S. Dugdale and F. E. Simon, *Proc. Roy. Soc. (London)* **A128**, 291 (1953).

[155] J. H. Vignos and H. A. Fairbank, *Phys. Rev. Letters* **6**, 265 (1961).

[156] A. F. Schuch and R. L. Mills, *Phys. Rev. Letters* **8**, 469 (1962).

[157] J. S. Dugdale and J. P. Franck, *Phil. Trans. Roy. Soc. London* **A257**, 1 (1964).

[158] D. O. Edwards and R. C. Pandorf, *Phys. Rev.* **140**, A816 (1965).

[159] A. Driessen, E. vand der Poll and I. F. Silvera, *Phys. Rev. B* **33**, 3269 (1986).

[160] *Liquids Under Negative Pressures* ed. by A. R. Imre *et al.* (Kluwer Academic Publishers, Dordrecht, 2002).

[161] F. Caupin and S. Balibar, *Phys. Rev. B* **64**, 064507 (2001).

[162] S. Balibar, *J. Low Temp. Phys.* **129**, 363 (2002).

[163] J. Boronat and J. Casulleras, *Phys. Rev. B* **50**, 3427 (1994).

[164] G. H. Bauer *et al.*, *Phys. Rev. B* **61**, 9055 (2000).

[165] F. Werner *et al.*, *J. Low Temp. Phys.* **136**, 93 (2004).

[166] F. Albergamo it et al., *Phys. Rev. Lett.* **92**, 235301 (2004).

[167] J. V. Pearce *et al.*, *Phys. Rev. Lett.* **93**, 145303 (2004).

[168] R. De Bruyn Ouboter and C. N. Yang, *Physica* (Amsterdam) **44B**, 127 (1987).

[169] B. Abraham *et al.*, *Phys. Rev. A* **1**, 250 (1970).

[170] D. A. Arms, R. S. Shah and R. O. Simmons, *Phys. Rev. B* **67**, 94303 (2003).

[171] C. T. Venkataraman and R. O. Simmons, *Phys. Rev. B* **68**, 224303 (2003).

[172] D. E. Galli and L. Reatto, *Phys. Rev. Lett.* **90**, 175301 (2003).

[173] B. Chaudhuri, F. Pederiva and G. V. Chester, *Phys. Rev. B* **60**, 3271 (1997).

[174] F. London in *Superfluids* (Wiley, New York, 1954).

[175] G. B. Hess and W. M. Fairbank, *Phys. Rev. Lett.* **19**, 216 (1967).

[176] A. J. Leggett, *Phys. Rev. Lett.* **25**, 1543 (1970).

[177] G. V. Chester, *Phys. Rev. A* **2**, 256 (1970).

[178] R. A. Guyer, *Phys. Rev. Lett.* **26**, 174 (1971).

[179] W. M. Saslow, *Phys. Rev. Lett.* **36**, 1151 (1976).

[180] D. M. Ceperley and B. Bernu, *Phys. Rev. Letts.* **93**, 155303 (2004).

[181] B. Bernu and D. M. Ceperley, cond-mat/0502486.

[182] D. Galli, M. Rossi and L. Reatto, *Phys. Rev. B* **71**, 140506 (2005).

[183] R. A. Aziz, F. R. W. McCourt, and C. C. K. Wong, *Mol. Phys.* **61**, 1487 (1987).

[184] R. A. Aziz, V. P. S. Nain, J. S. Carley, W. L. Taylor and G. T. McConville, *J. Chem. Phys.* **70**, 4330 (1979).

[185] L. Vranjes, J. Boronat, J. Casulleras and C. Cazorla, *Phys. Rev. Lett.* **95**, 145302 (2005).

[186] F. Dalfovo, S. Giorgini and L. P. Pitaevskii, *Rev. Mod. Phys.* **71**, 463 (1999).

[187] M. H. Kalos, M. A. Lee, P. A. Whitlock and G. V. Chester, *Phys. Rev. B* **24**, 115 (1981).

[188] F. Ancilotto, M. Barranco, F. Caupin, R. Mayol and M. Pi, cond-mat/0509200.

[189] S. A. Vitiello, *Phys. Rev. B* **65**, 214516 (2002).

[190] M. P. Allen and D. J. Tildesley in *Computer Simulation of Liquids* (Clarendon Press, Oxford 1987).

[191] E. R. Grilly, *J. Low Temp. Phys.* **11**, 33 (1973).

[192] P. W. Anderson, cond-mat/0504731.

[193] P. W. Anderson, cond-mat/0507654.

[194] J. G. Dash and J. S. Wettlaufer, *Phys. Rev. Lett.* **94**, 235301 (2005).

[195] L. Reatto, *Phys. Rev.* **183**, 334 (1969).

[196] K. Kostas, J. Boronat and J. Casulleras, private communication (2005).

[197] We have checked this result, however it has been proof that such type of trial wave function can describe correctly the ground state of a 1D system of interacting dipoles, cond–mat/050700.